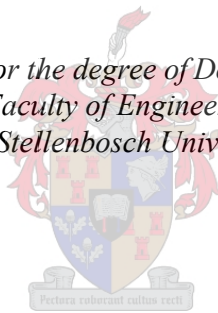


Modelling and Mitigation of Specular Multipath Interference in a Dual-Frequency Phase-Comparison FMCW Radar System

by
Willem Petrus Francois Schonken

*Dissertation presented for the degree of Doctorate in Engineering at the
Faculty of Engineering at
Stellenbosch University*



Supervisor: Prof JB de Swardt
Co-supervisor: Dr P van der Merwe

March 2017

Declaration

By submitting this thesis/dissertation electronically, I declare that the entirety of the work contained therein is my own, original work, that I am the sole author thereof (save to the extent explicitly otherwise stated), that reproduction and publication thereof by Stellenbosch University will not infringe any third party rights and that I have not previously in its entirety or in part submitted it for obtaining any qualification.

March 2017

Copyright © 2017 Stellenbosch University

All rights reserved

Abstract

Digital signal processing technology has improved greatly over the last two decades. Increased processing power, cheaper memory and higher sampling rates have enabled the application of Frequency-Modulated Continuous Wave (FMCW) radar to a myriad of new areas. FMCW offers a number of advantages, such as continuous coverage and low peak output power, making it an attractive technology for industrial and automotive applications.

Expansion into new application environments and the use of new signal processing algorithms have created a need for new multipath interference models. This study aims to fulfil that need through rigorous mathematical modelling of both the physical multipath environment and the two-dimensional Fast Fourier Transform (FFT) signal processing method, in the context of a Dual-Frequency Phase-Comparison FMCW radar sensor. It will be shown that specular reflections can have a profound effect on the amplitude and the phase of an FMCW radar's base-band received signals. The multipath phase error interacts with the signal processing method, resulting in new and interesting effects. Furthermore, new mitigation methods will be proposed and critically evaluated by means of simulated and real-world measurements.

Opsomming

Digitale seinverwerkingstegnologie het baie verbeter oor die laaste twee dekades. Toenames in verwerkerkapasiteit, goedkoper geheue en hoër monstertempo's maak dit moontlik om Frekwensie-Gemoduleerde Kontinuegolf (FGKG) radar in verskeie nuwe toepassings te gebruik. FGKG bied 'n aantal voordele, soos ononderbroke dekking en lae piek-uittreedrywing, wat dit 'n aanloklike tegnologie maak vir industriële en motorvoertuig-toepassings.

Die uitbreiding van FGKG na nuwe toepassingsareas, asook die gebruik van nuwe seinverwerkingsalgoritmes, skep 'n behoefte aan nuwe multipad-steuringsmodelle. Die doel van hierdie studie is om aan daardie behoefte te voldoen deur middel van deeglike wiskundige modellering van beide die fisiese omgewing, asook die twee-dimensionele Vinnige Fourier Transform (VFT) seinverwerkingsmetode, binne die konteks van 'n Dubbelfrekwensie-Fasevergelykende FGKG-radarsensor. Daar sal gewys word dat spekulêre weerkaatsings 'n diepgaande uitwerking kan hê op die amplitude en fase van 'n FGKG-radar se basisband-ontvangde seine. Daar is 'n wisselwerking tussen die multipad-fasefout en die seinverwerkingsmetode, wat nuwe en interessante nagevolge het. Verder sal daar ook nuwe foutverminderingsmaatreëls voorgestel word, wat krities geëvalueer sal word aan die hand van simulasiedata en regtewêreld-meetings.

Publications

Sections of the work presented in this dissertation will be published in the following article:

W.P.F. Schonken, J.B. de Swardt and P. van der Merwe, “Multipath Modelling in a Dual-Frequency Phase-Comparison FMCW Radar”, in *Proceedings of the 16th Mediterranean Microwave Symposium (MMS2016)*, Abu Dhabi, United Arab Emirates, November 2016.

Acknowledgements

A project of this magnitude would not have been possible without the help and support of several people. I would like to thank the following people in particular:

- My study leaders, Prof JB de Swardt and Dr P van der Merwe, for their advice, encouragement, and seemingly endless patience.
- Reutech Radar Systems, for their generous funding, and for allowing me the opportunity to work on such an interesting problem.
- My parents and family, for their guidance, love, and support throughout my life.

I must not fear.

Fear is the mind-killer.

Fear is the little-death that brings total obliteration.

I will face my fear.

I will permit it to pass over me and through me.

And when it has gone past I will turn the inner eye to see its path.

Where the fear has gone there will be nothing.

Only I will remain.

The Litany Against Fear.

From the novel *Dune*,

by Frank Herbert.

Contents

List of Tables.....	ix
List of Figures	x
List of Abbreviations.....	xiv
Chapter 1: Introduction	1
1.1 Problem Statement	1
1.2 Contributions.....	2
1.3 Layout of this Dissertation	2
Chapter 2: Literature Review	4
2.1 Dual-Frequency Phase-Comparison FMCW Radar	4
2.1.1 Overview of FMCW Radar.....	4
2.1.2 Angle Extraction	5
2.1.3 Dual-Frequency Operation.....	6
2.2 Terrain Modelling	7
2.2.1 Smooth Flat Surface.....	7
2.2.2 Rough Flat Surface.....	8
2.2.3 Vegetation	8
2.2.4 Other Terrain Effects	9
2.3 Mitigation Techniques.....	9
2.3.1 Increased Bandwidth.....	9
2.3.2 Ultra-Wideband.....	10
2.3.3 Integration of Additional Measurement Information	10
2.3.4 Synthetic Aperture Approach.....	11
2.3.5 Beam-Forming	12
2.3.6 Neural Network Approach	13
2.3.7 Additional Inertial Sensors.....	14
2.3.8 System Optimisation for a Specific Environment.....	15
2.4 Conclusion.....	16
Chapter 3: FMCW Signal Processing	17

3.1	Stationary Target.....	18
3.2	Moving Target.....	20
3.3	Range-Doppler Processing.....	22
3.3.1	Range FFT.....	24
3.3.2	Doppler FFT.....	26
3.4	Confirmation of Theoretical Approximation	28
3.4.1	Amplitude.....	29
3.4.2	Quadratic Frequency	31
3.4.3	Other Negligible Terms	32
3.5	Conclusion.....	36
Chapter 4: Multipath Model		37
4.1	Terrain Model Selection.....	37
4.2	Specular Multipath Model.....	40
4.3	Integration of Multipath Model.....	45
4.4	Confirmation of Integrated Model	48
4.5	Conclusion.....	49
Chapter 5: Phase Interferometry.....		50
5.1	Basic Angle-of-Arrival Extraction.....	50
5.2	Translating AoA into Elevation and Azimuth Angles	51
5.2.1	Equilateral Triangle Antenna Constellation.....	52
5.2.2	Right-Angled Triangle Antenna Constellation	55
5.2.3	Two-by-Three Matrix Antenna Constellation.....	57
5.3	Receiver Spacing and AoA Ambiguities.....	58
5.4	Dual-frequency Angle Extraction	58
5.5	Multipath Effect	59
5.6	Conclusion.....	62
Chapter 6: Mitigation Methods		63
6.1	Method 1: Single Channel Phase Unwrapping.....	63
6.1.1	Algorithm Description	63
6.1.2	Simulation Example.....	65

6.1.3	Measured Data Example	72
6.2	Method 2: Sum-Difference Processing	79
6.2.1	Algorithm Description	80
6.2.2	Simulation Example	81
6.2.3	Measured Data Example	83
6.3	Method 3: Filtering	85
6.3.1	Filter Description	85
6.3.2	Simulation Example	86
6.3.3	Measured Data Example	90
6.4	Comparison	94
Chapter 7: Conclusions		95

List of Tables

3.1	Burst phase components.....	28
6.1	Simulation parameters.....	65
6.2	Simulation parameters.....	81
6.3	Simulation parameters.....	86
6.4	Comparison of mitigation methods.....	94

List of Figures

2.1	Illustration of typical FMCW signals. The instantaneous transmitter frequency increases linearly over the duration of a sweep. Echoes are delayed by a period of time (Δt), resulting in a frequency difference (Δf).	5
2.2	The Angle-of-Arrival (θ) of a signal can be determined by comparing the phases of Rx1 and Rx2.	6
2.3	Antenna configuration example.	6
2.4	Direct and reflected signal paths for a smooth flat surface.	7
2.5	Measurement results of the inverse synthetic aperture approach for position location implemented in [35].	11
2.6	Calculated received power with multipath interference for various values of receiver height (h_R), taken from [42].	12
2.7	Calculated received power when two appropriately spaced antennas are used, taken from [42].	13
2.8	Example of frequency shift due to a closely spaced multipath tone, taken from [43]. In this example $\Delta f = 2.2$ kHz and $\Delta \phi = 0$	14
2.9	Diagram of IMU-assisted FMCW system, taken from [45].	15
3.1	Examples of modulation schemes employed in FMCW systems.	17
3.2	General FMCW radar system diagram.	18
3.3	Linear Frequency-Modulated Continuous Wave modulation scheme.	18
3.4	Illustration of the two-dimensional FFT (range-Doppler) processing method.	23
3.5	Progression of phasors after range-FFT for consecutive sweeps. A range-bin's amplitude will remain (almost) constant for consecutive sweeps, but if the target is moving the phase will change.	23
3.6	Example of a range-Doppler map. The image on the left shows the entire map, while the image on the right has been magnified to show a detection.	24
3.7	Difference between theoretically calculated and simulated burst phase.	29

3.8	Burst phase error for various radial velocities, rectangular windowing function.	30
3.9	Burst phase error for various radial velocities, Blackman windowing function.	30
3.10	Ratio between πp and Doppler-bin width as a function of radial velocity.....	33
3.11	Ratio between f_{error} and range-bin frequency as a function of radial velocity.....	34
3.12	Non-linear phase terms Φ_{err1} (a) and Φ_{err2} (b) as functions of radial velocity.	35
4.1	Simulated phase error due to diffuse multipath interference.	37
4.2	Simulated change in amplitude due to diffuse multipath interference.....	38
4.3	Simulated phase error due to specular multipath.	39
4.4	Simulated change in amplitude due to specular multipath.....	39
4.5	Illustration of possible signal paths.....	40
4.6	Change in base-band signal amplitude as a function of Y for various reflection coefficients (blue denotes a smaller coefficient and red a larger coefficient).....	44
4.7	Change in base-band signal phase as a function of Y for various reflection coefficients (blue denotes a smaller coefficient and red a larger coefficient).	44
4.8	Ratio between $\Phi_{\Delta mp}$ and Doppler-bin width as a function of range and for various radial velocities.	47
4.9	Burst phase error due to specular multipath for various radial velocities.....	47
4.10	Comparison of theoretical and simulated burst phase errors due to specular multipath interference.....	48
4.11	Comparison of theoretical and simulated burst phase errors due to specular multipath interference.....	49
5.1	The Angle-of-Arrival (γ) determines the difference in path length ($d\sin\gamma$) that a signal travels to two receivers separated by a distance of d	50
5.2	Elevation and azimuth angles relative to a global coordinate system.....	52
5.3	Equilateral triangle antenna configuration (as seen from the back).....	53

5.4	Two-dimensional approximation to determine elevation and azimuth angles (equilateral triangle).....	53
5.5	Right-angle antenna configuration (as seen from the back).....	55
5.6	Elevation and azimuth angle geometry for the right-angled configuration.....	56
5.7	Two-by-three matrix antenna constellation (as seen from the back).	57
5.8	Ambiguous angles for a phase difference measurement of 0.....	60
5.9	Coarse angle error and the resulting ambiguity angle error for (a) $ I = 0.1$, (b) $ I = 0.3$ and (c) $ I = 0.5$	62
6.1	Single-channel phase unwrapping algorithm.	64
6.2	Range-bin number as a function of range.	66
6.3	Estimated range as a function of range.	67
6.4	Comparison of burst phase (a) before and (b) after compensation.	68
6.5	Estimated q as a function of range.	69
6.6	Compensated burst phase after subtracting πq	70
6.7	Unwrapped, compensated burst phase as a function of range.....	71
6.8	Final estimation of multipath phase error.	72
6.9	Detected range-bins for all channels.	73
6.10	Detected Doppler-bins for all channels.	73
6.11	Estimated radial velocity.....	74
6.12	Comparison of estimated range and corresponding bin range.	74
6.13	Estimates for q and a (offset from each other for clarity).....	75
6.14	Compensated burst phase for all channels.	76
6.15	Unwrapped, compensated burst phase for all channels.....	76
6.16	Unwrapped, compensated burst phase for all channels after additional correction.	77

6.17	Single-channel multipath phase error estimates.....	77
6.18	Comparison between coarse angle phases and their estimated multipath components. Expected coarse angle phases (calculated from the physical geometry of the measurement setup) are displayed as dashed lines.....	78
6.19	Sum-difference processing algorithm.	81
6.20	Comparison between estimated and actual multipath phase difference.....	82
6.21	Comparison between estimated and actual multipath phase error.	82
6.22	Estimated Y for all channels.	83
6.23	Estimated multipath phase difference for Rx1f1 channel, shown in blue. A magnified version of the offset correction is shown in red.	83
6.24	Comparison between corrected and non-corrected coarse angle phase for (a) Φ_{ca1} , (b) Φ_{ca2} and (c) Φ_{ca3}	85
6.25	Angle-of-arrival phases ($\angle\Phi$) for (a) f1 = 10.1 GHz, (b) f2 = 9.1 GHz and (c) f3 = f1 – f2 = 1 GHz.....	88
6.26	Comparison of filtered and unfiltered coarse angle phase ($\angle\Phi$ at f3) for (a) $\alpha = 1/300$, (b) $\alpha = 1/4000$ and (c) $\alpha = 1/10000$	90
6.27	Comparison of filtered and unfiltered coarse angle phases for (a) Φ_{ca1} , (b) Φ_{ca2} and (c) Φ_{ca3} . In this example the filter was initialised with favourable values.	92
6.28	Comparison of filtered and unfiltered coarse angle phases for (a) Φ_{ca1} , (b) Φ_{ca2} and (c) Φ_{ca3} . In this example the filter was initialised with extreme values.....	93

List of Abbreviations

ADC	- Analogue-to-Digital Converter
APS	- Active Protection System
AoA	- Angle-of-Arrival
DFT	- Digital Fourier Transform
ESD	- Energy-Spectral-Density
FFT	- Fast Fourier Transform
FMCW	- Frequency-Modulated Continuous Wave
IF	- Intermediate Frequency
IMU	- Inertial Measurement Unit
LFMCW	- Linear FMCW
LOS	- Line-of-Sight
MTI	- Moving Target Indicator
NLOS	- Non-Line-of-Sight
RPG	- Rocket-Propelled Grenade
Rx	- Receiver
SNR	- Signal-to-Noise Ratio
TDOA	- Time-Difference-of-Arrival
Tx	- Transmitter
UWB	- Ultra Wideband
VCO	- Voltage Controlled Oscillator

Chapter 1: Introduction

Before the advent of high-speed analogue-to-digital converters (ADC), it was impractical to measure phase directly in monopulse architectures. Phase-comparison monopulse systems had to rely on analogue techniques to convert phase information into amplitude information [1]. Amplitude-comparison monopulse systems were generally more accurate and therefore more popular. Modern ADC circuitry, combined with high-performance digital processors, make it possible to sample radar signals and calculate phase information quickly and accurately. This has led to renewed interest in phase-comparison solutions, an example of which is the Active Protection System (APS) radar sensor developed by Reutech Radar Systems. This radar system is used to detect and track high-velocity targets with small radar cross-sections (rocket-propelled grenades or RPGs) in real time.

Frequency-Modulated Continuous Wave (FMCW) radar has also seen an increase in popularity over the previous decade. Modern digital signal processing hardware, along with high-power solid-state amplifiers, has enabled the utilisation of FMCW techniques in a myriad of new applications, such as:

- Local Positioning Systems
- Tachymeters
- Imaging Radars
- Automotive Radars
- Electronic Warfare Systems

New applications and signal processing methods necessitate the development of novel mathematical models to describe the interactions between radar signals, radar circuitry and the physical environment.

1.1 Problem Statement

There are many environmental effects that can lead to degradation of signal quality in radar systems. One of the more difficult phenomena to predict and mitigate is multipath [1]. The reason for this difficulty is the inherent unpredictability of the terrain in which most radar applications have to operate [2] [3]. Several models have been proposed in an attempt to model specific terrain aspects [4]. These environmental aspects interact with radio signals in subtly different ways, creating a variety of multipath signals. Statistical models are commonly used to account for multipath in unpredictable scenarios. This is especially evident in FMCW applications for industrial purposes (e.g. asset location), where indoor environments are very common.

The APS radar sensor presents a fairly unique situation, as it will be deployed in an outdoor scenario. This requires the development of a new, more deterministic multipath model to describe the interaction between the environment and the radar. Furthermore, an effective multipath mitigation method is also needed to cope with interfering reflections. The objectives for this study can therefore be stated as follows:

- Develop a novel multipath interference model that accounts for both the physical environment and the signal processing techniques employed by Dual-Frequency Phase-Comparison FMCW radar systems.
- Propose and evaluate mitigation methods to cope with multipath interference.

1.2 Contributions

This study required the development of new models, as well as the expansion of previous work, leading to several contributions:

- The expansion of the two-dimensional FFT (range-Doppler) processing method formula to include phase terms that were previously ignored.
- An evaluation of all burst phase terms to determine their influence on measured phase.
- The development of a new specular multipath model for FMCW receivers.
- The integration and evaluation of a new multipath model with the expanded range-Doppler processing method formula to determine the influence of specular multipath on measured burst phase.
- The development and evaluation of new multipath mitigation techniques.

1.3 Layout of this Dissertation

This study aims to develop a new multipath model for FMCW radars operating in an outdoor environment where both the radar and the target are fairly close (in the order of one to two metres) to a reflective ground plane. A suitable mitigation method will also be proposed. The work is divided into the following parts:

- A literature review is presented in the second chapter. This part of the dissertation will investigate terrain models and mitigation techniques for multipath interference. It will also provide a brief description of Dual-Frequency Phase-Comparison FMCW radars.
- Chapters 3 and 4 will present rigorous mathematical models for range-Doppler processing and multipath interference in FMCW systems. This will provide insight into the effects that multipath has on phase and amplitude measurements.

- The next section, contained in Chapter 5, will look at phase interferometry. A concise explanation of angle extraction will be given in order to understand how erroneous phase measurements affect elevation and azimuth parameters.
- Chapter 6 will propose three mitigation methods. All three methods will be critically evaluated through simulated and measured data.
- The last chapter will present final conclusions.

Chapter 2: Literature Review

This chapter consists of three parts:

- The first section will give a brief explanation of Dual-Frequency Phase-Comparison FMCW radar, using the Active Protection System (APS) sensor as an example.
- The next section will investigate various physical terrain models.
- The last section will investigate a number of multipath mitigation techniques for typical FMCW applications.

2.1 Dual-Frequency Phase-Comparison FMCW Radar

The Active Protection System (APS) radar sensor is a staring radar system designed and constructed by Reutech Radar Systems to find and track high-velocity targets with small radar cross-sections (RCSs) using phase interferometry [5]. A Frequency-Modulated Continuous Wave (FMCW) radar approach was utilised, which has several advantages:

- Continuous coverage of the target area.
- Sufficient output power can be achieved with solid-state components.
- Multiple targets can be tracked simultaneously, as long as they are separated in range or Doppler.
- FMCW systems are intrinsically coherent, making them a sensible choice for phase interferometry.

2.1.1 Overview of FMCW Radar

Frequency-Modulated Continuous Wave (FMCW) radar systems work by generating a signal, of which the frequency changes over time, transmitting it and comparing any received signals with the locally generated signal. Due to the physical distance that the transmitted signal must travel before reaching a target and being reflected back to the radar, there is a time delay between the locally generated signal and received echo signals. This leads to a difference in instantaneous frequency between transmitted and received signals, as shown in Figure 2.1. There is a direct relationship between the frequency difference and the round-trip time-of-flight, which is exploited to calculate the distance between the radar and the target.

FMCW systems typically mix the incoming receiver signal with a copy of the outgoing transmitter signal to produce a base-band or beat signal. Spectral analysis of the beat signal is performed to extract range and Doppler information, from which the radial velocity and distance to each target can be

computed. More detailed information on FMCW radar signal processing will be presented in Chapter 3.

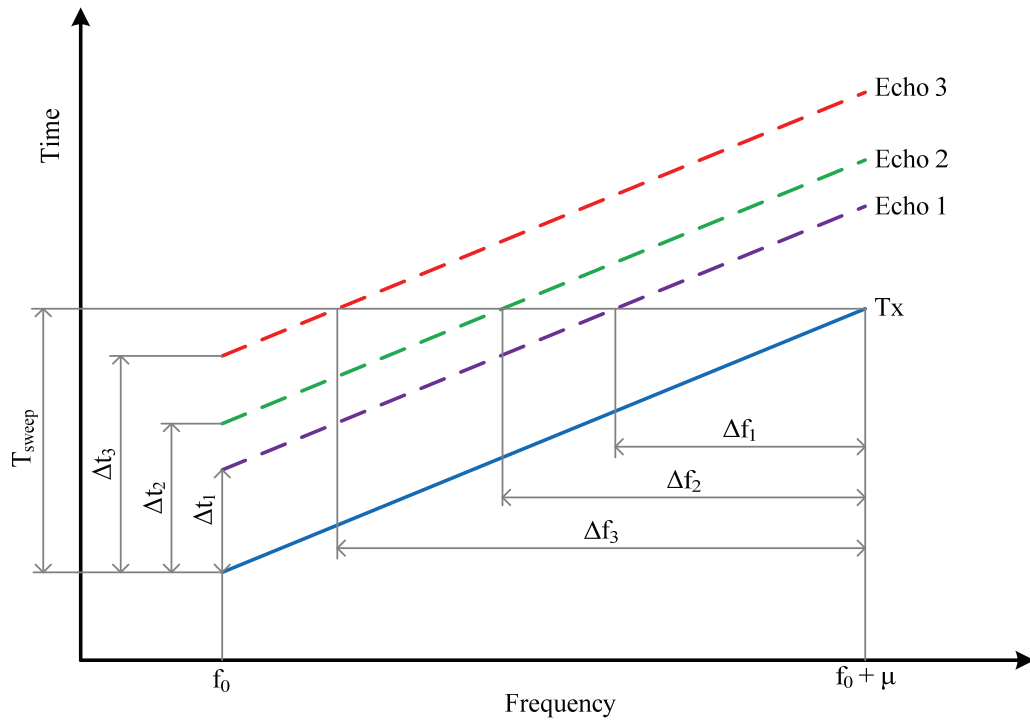


Figure 2.1 Illustration of typical FMCW signals. The instantaneous transmitter frequency increases linearly over the duration of a sweep. Echoes are delayed by a period of time (Δt), resulting in a frequency difference (Δf).

2.1.2 Angle Extraction

After finding the range and velocity, it is also necessary to determine the direction of the target relative to the radar. This is accomplished by comparing the measured phase (at the target's corresponding beat frequency) of two or more closely spaced receivers. A difference in phase implies that the echo signal arrives slightly earlier at one receiver than it does at the other, which can be used to calculate the Angle-of-Arrival (AoA) of that echo signal. This is illustrated in Figure 2.2.

In the case of the APS system, three receive antennas are spaced approximately 5λ (five wavelengths) apart, in the shape of an equilateral triangle. A fourth antenna, used for signal transmission, is placed in the centre of the receive antenna array, shown in Figure 2.3. Three receive antennas allow for the extraction of both azimuth and elevation angles.

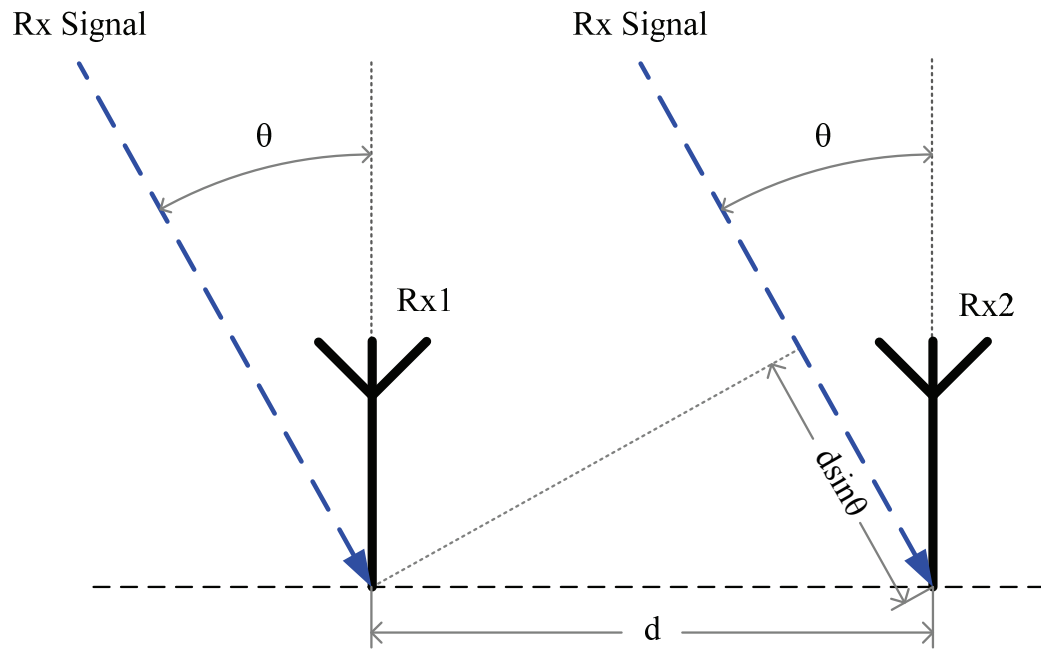


Figure 2.2 The Angle-of-Arrival (θ) of a signal can be determined by comparing the phases of Rx1 and Rx2.

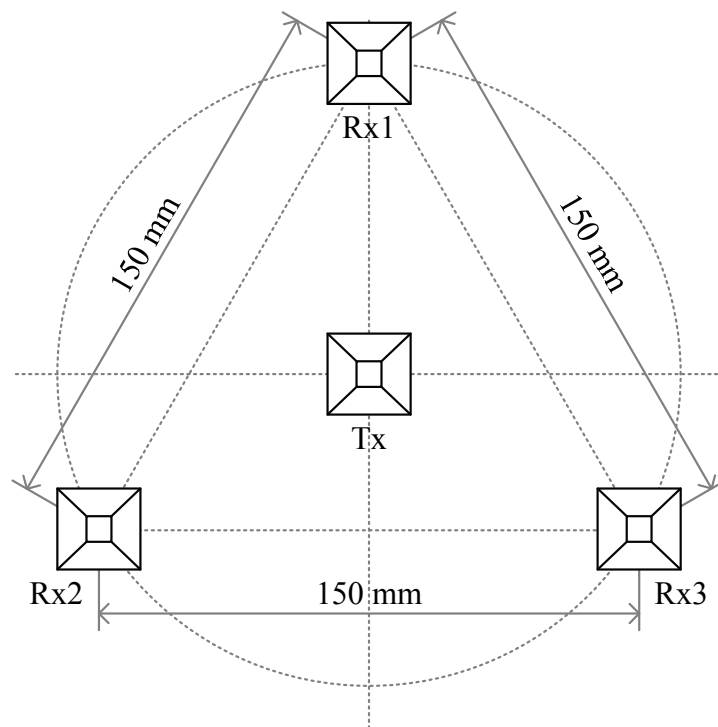


Figure 2.3 Antenna configuration example.

2.1.3 Dual-Frequency Operation

The physical size of the receive antennas and the required isolation between the transmitter and the receivers determine the relatively large 5λ antenna spacing. This results in ambiguities when calculating elevation and azimuth angles, which is resolved by transmitting at two carrier frequencies

instead of one. APS generates a chirp signal that starts at 9.1 GHz and another chirp that starts at 10.1 GHz. Echoes from both chirps can be used to create a third artificial phase measurement at 1 GHz, where the antenna spacing is approximately half a wavelength and unambiguous angles can be extracted. A detailed analysis of this will be presented in Chapter 5.

2.2 Terrain Modelling

Much research has been done to model, predict and interpret the effects of radar reflectivity for various terrains. Knowledge of how and why microwave signals interact with the physical environment allows us to improve the performance of radar systems in terms of resolution and accuracy [1]. It also allows us to expand the potential application areas for radar technology. This has been driven by, amongst other fields, the geosciences [7] [8]. The need for mapping of terrain in remote or inaccessible locations, finding and mapping of resources, mapping of agricultural land usage and many other applications have led to a number of specific terrain models. The following subsections will explore the main aspects regarding the modelling of physical terrain.

2.2.1 Smooth Flat Surface

This is the simplest model for multipath interference and forms the basis for the other multipath models in the following subsections. Reflection due to a smooth, flat surface is shown in Figure 2.4:

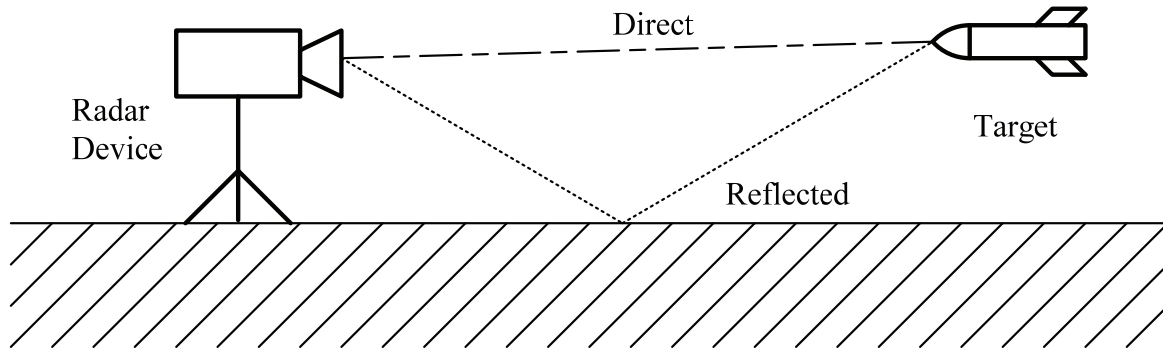


Figure 2.4 Direct and reflected signal paths for a smooth flat surface.

There are four main signal paths; three are the result of reflections and one is the direct line-of-sight path. For each reflection, the signal undergoes attenuation and a phase-shift [9]. Attenuation and phase-shift are determined by the reflection coefficients for horizontal and vertical polarization, as given by Fresnel's equations ((2.1) and (2.2), taken from [4]):

$$\Gamma_H = \frac{\sin\alpha - (\epsilon - \cos^2\alpha)^{\frac{1}{2}}}{\sin\alpha + (\epsilon - \cos^2\alpha)^{\frac{1}{2}}} \quad (2.1)$$

$$\Gamma_V = \frac{\varepsilon \sin \alpha - (\varepsilon - \cos^2 \alpha)^{\frac{1}{2}}}{\varepsilon \sin \alpha + (\varepsilon - \cos^2 \alpha)^{\frac{1}{2}}} \quad (2.2)$$

where α is the incidence angle, ε is the complex dielectric constant of the surface and Γ_H and Γ_V are the reflection coefficients for horizontal and vertical polarization respectively. The complex dielectric constant ε is dependent on the properties of the surface material and will typically vary with frequency [6].

2.2.2 Rough Flat Surface

Subsection 2.2.1 illustrated the reflections that can be expected from a smooth, flat surface. This is referred to as the specular component of the reflected power, but there is also a diffuse component. Consider equation (2.3) (taken from [4]):

$$\Delta\Phi = \frac{4\pi\Delta h \sin\theta}{\lambda} \quad (2.3)$$

where λ is wavelength, θ is the grazing angle and Δh is the difference in height of two points on the reflecting surface. $\Delta\Phi$ is the phase-shift that is introduced between two waves reflecting off these two points. Lord Rayleigh considered a surface electromagnetically smooth if:

$$\Delta h \sin\theta < \frac{\lambda}{8} \quad (2.4)$$

The Rayleigh Roughness Criterion (2.4) is used to determine whether a surface is electromagnetically smooth or rough. A rough surface will produce a diffusely reflected signal, which has a uniformly distributed phase. It can essentially be thought of as a large number of small, independent scatterers, each contributing to the total field [4]. Reflected signals typically have both a specular and a diffuse component.

2.2.3 Vegetation

Vegetation can be modelled in several different ways, depending on leaf structure, leaf size, vegetation height, moisture content and operating frequency. One model, suggested by [7], assumed that each individual blade or stem scatters like a long, thin, lossy cylinder. The model also assumes that very little of the incident energy reaches the underlying surface. This implies that absorption depends on the complex dielectric constant of the vegetation. A field with an adequate covering of grass would be a good physical example for this model.

Similarly, leaves could be modelled as planar sheets, since the actual size of the leaves is greater than the operating wavelength at higher microwave frequencies. This was used by [8] to account for various polarizations of scattered fields, the scattering geometry and other parameters.

2.2.4 Other Terrain Effects

The terrain effects that have been considered up to this point were restricted to land-based models. The Smooth Flat Surface model can be used to describe sea reflection for small areas of ocean under very tranquil conditions [4], but this is a rare situation. More comprehensive models have been developed to include the effects of oceanic wave motion [9] [10]. Sea waves can be divided into larger waves, which can be several metres high, and capillaries, which are superimposed onto the larger wave structure.

Another terrain model is that of Composite Surfaces [11] [12]. Natural surfaces that are very rough (with average height differences greater than a wavelength) normally possess a smaller scale of roughness as well, for instance the oceanic wave model mentioned in the previous paragraph [4]. The reflecting surface can be thought of as a number of smaller, slightly rough scattering surfaces that are tilted at various angles.

There are a number of propagation effects that have not been mentioned yet, such as depolarization, divergence caused by the curvature of the earth's surface, atmospheric scattering, atmospheric absorption and reflectivity models of larger vegetation structures (such as trees).

2.3 Mitigation Techniques

Multipath interference is a common source of errors in a number of electronic systems, e.g. channel fading in wireless communication systems [13], loss of accuracy in position location systems [14] [15] or incorrect angle resolution in tracking radars [1]. Much research has been done to compensate for this source of interference or in some cases even exploit the additional information provided by multiple signal paths. The following subsections will briefly discuss a few mitigation techniques that are commonly used in FMCW systems.

2.3.1 Increased Bandwidth

Some mitigation techniques attempt to distinguish direct line-of-sight signals from reflected or multipath signals in time and/or frequency [16] [17] [18] [19]. Increasing system bandwidth typically allows for improved range-resolution [20] [21]. Consider the following equation, taken from [20]:

$$\Delta R_{rect} \approx 2 \frac{c}{3B_{fm}} \quad (2.5)$$

where B_{fm} is the effective signal bandwidth,

c is the propagation velocity and

ΔR_{rect} is the range-resolution (minimum distance required to separate two targets).

With sufficient range-resolution it is possible to distinguish direct line-of-sight (LOS) echoes from non-direct line-of-sight (NLOS) echoes in radar systems, as a LOS return corresponds to the shortest signal path for a particular target.

An example where sufficient bandwidth is employed to mitigate the effects of severe multipath is the active transponder system (with high-precision clock synchronisation) presented in [22] and [23]. This work is further extended in the design of a 24 GHz radar tachymeter, presented in [24], where distance and angle were measured with root-mean-square errors of 2.2 cm and 0.16°, respectively.

2.3.2 Ultra-Wideband

Ultra-Wideband (UWB) techniques can be used where increasing the bandwidth for other topologies becomes unpractical. UWB techniques go hand-in-hand with very high range-resolution [25] [26], which often makes it possible to separate LOS and NLOS return signals [27], [28]. A drawback of UWB systems is the relatively low coverage due to restrictions on transmitted energy [29]. The pulsed frequency modulation techniques presented in [30], [31] and [32] attempt to overcome this limitation by combining the strengths of UWB and FMCW.

2.3.3 Integration of Additional Measurement Information

A standard FMCW system will analyse the beat frequency to determine range and velocity [1]. The systems proposed in [33] and [34] utilise the phase information, which was previously discarded, to improve overall accuracy. If three consecutive measurements to the same target are taken with instantaneous phases φ_1 , φ_2 and φ_3 , the angular rates (ω) and acceleration (α) can be calculated as follows:

$$\begin{aligned}\omega_1 &= \frac{\varphi_2 - \varphi_1}{\Delta T} \\ \omega_2 &= \frac{\varphi_3 - \varphi_2}{\Delta T} \\ \alpha_\varphi &= \frac{\omega_2 - \omega_1}{\Delta T}\end{aligned}\tag{2.6}$$

where ΔT is the elapsed time between consecutive measurements. Calculating angular rate and angular acceleration from phase measurements provides additional information, which can be used to improve range and velocity accuracy or to detect non-line-of-sight (NLOS) signals.

2.3.4 Synthetic Aperture Approach

Vossiek, Urban, Max and Gulden propose an interesting inverse synthetic aperture approach in [35], which is further extended in [36] and [37]. The relative movements of a target are measured by assisting sensors (dead reckoning or inertia sensors) and used to create a short synthetic aperture. One (or more) radar units are mounted at fixed, known locations around the coverage area and measure the distance (using standard FMCW techniques) to a transponder that is attached to a mobile unit (target). A number of echo profiles are measured at arbitrary points along the relative trajectory and combined in a reconstruction algorithm to produce an image. The image maximum represents the most likely spatial location of the radar unit (or units), relative to the mobile transponder. Figure 2.5, taken from [35], shows an example of the reconstructed image from an experimental measurement. The radar unit was mounted at $x = 2.05$ m and $y = 3.75$ m. The white cross marks the image maximum, which translates to a 2-D localisation accuracy of 10 cm.

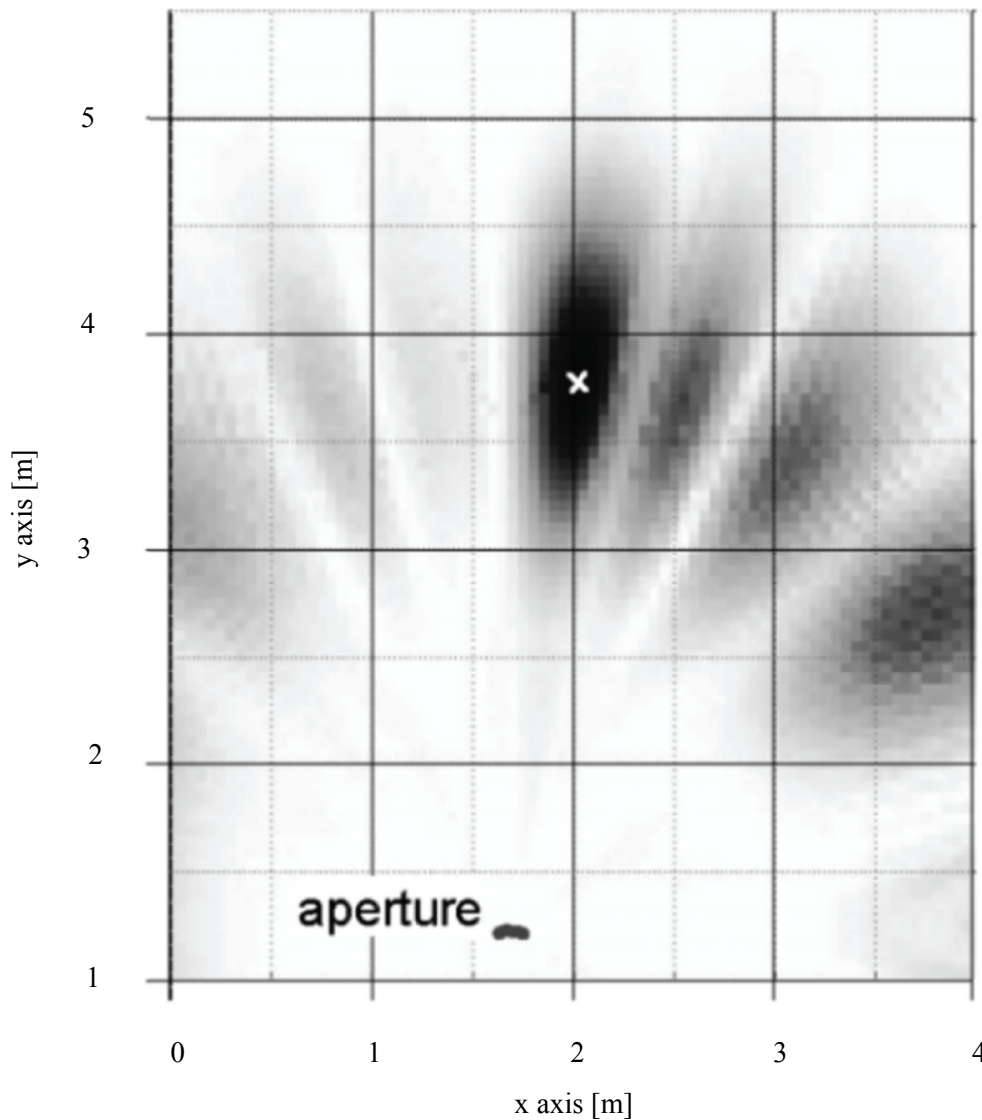


Figure 2.5 Measurement results of the inverse synthetic aperture approach for position location implemented in [35].

The synthetic aperture approach shows remarkable precision, even in tough multipath environments. It does, however, carry an increased computational overhead and requires additional relative sensors.

2.3.5 Beam-Forming

Beam-forming potentially offers a simple and inexpensive solution to reduce the effects of multipath. This is accomplished by using directional antennas that focus their beam on the direct line-of-sight (LOS) signal path, thereby eliminating or reducing possible non-line-of-sight (NLOS) signal paths [38]. The use of directional antennas reduces the coverage area and is more suitable for applications where a limited area needs to be illuminated at any given time.

More versatile solutions are available in the form of switched-beam topologies, as presented in [39] and [40], or multiple-input multiple-output systems like the one described in [41]. Digital beam-forming is used to focus energy on a smaller area, which suppresses interfering multipath signals, while still allowing for wide coverage. The coherent combination of several receive signals also increases effective antenna gain – a useful property for any radar system.

A third option is the use of spatial diversity, as presented in [42], where multipath interference is caused by a reflecting ground surface (asphalt road). Under severe multipath conditions, received signal strength can be greatly reduced. The reduction in signal strength is a function of range and receiver height (amongst other factors), illustrated in Figure 2.6.

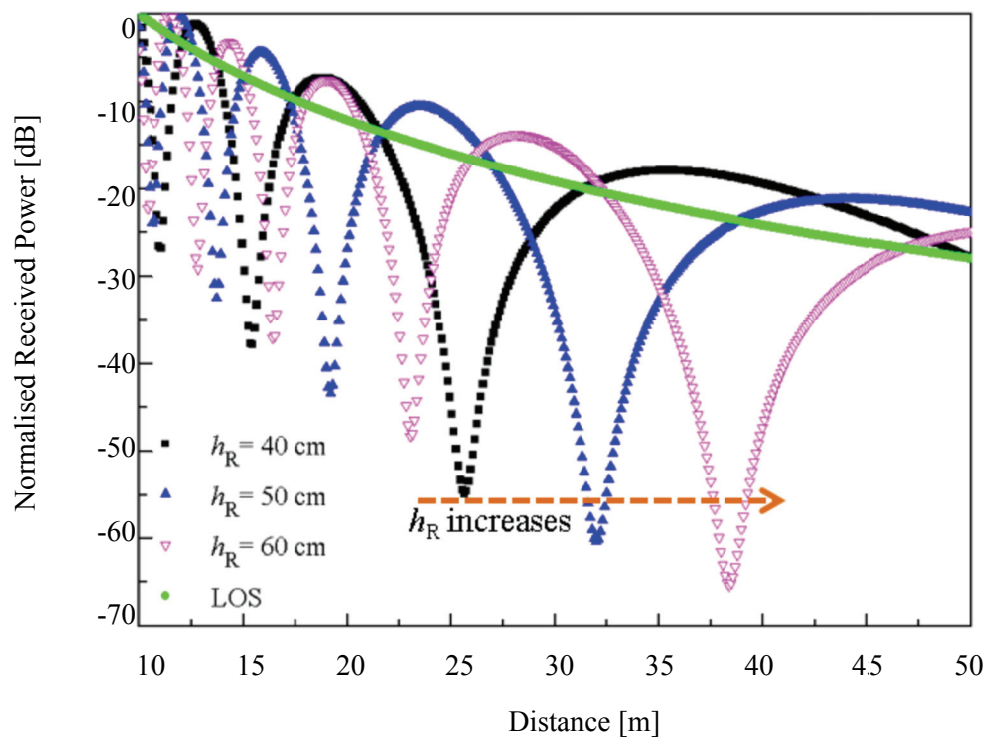


Figure 2.6 Calculated received power with multipath interference for various values of receiver height (h_R), taken from [42].

Combining two receive antennas with an appropriate difference in height reduces the maximum loss in signal strength, as shown in Figure 2.7:

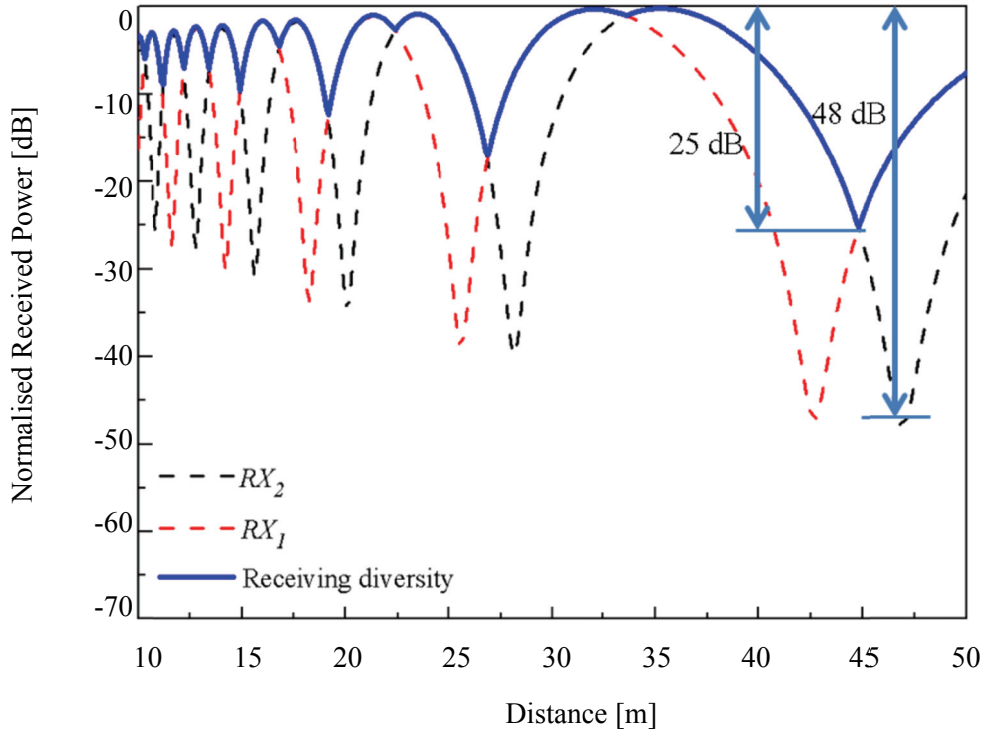


Figure 2.7 Calculated received power when two appropriately spaced antennas are used, taken from [42].

2.3.6 Neural Network Approach

Goetz, Waldmann and Weigel present an interesting mitigation technique in [43], which is then used to improve the accuracy of the system designed in [44]. It is based on Fourier spectral analysis for FMCW radar systems. The assumption is that spectral distortion is caused by multipath interference, which implies that a distorted peak corresponds to one target. A single target should produce a single peak (or tone) in the measured spectrum, if there are no interfering signals or distortions. Multipath signals produce additional tones, and may shift the frequency of the first peak.

A two-tone example is presented in Figure 2.8, comprised of a direct line-of-sight (LOS) signal and a non-line-of-sight (NLOS) multipath signal. For this example the following parameters were chosen:

$$\text{Signal duration} = 1 \text{ ms}$$

$$f_{LOS} = 100 \text{ kHz}$$

$$\phi_{LOS} = 0$$

Both signals are of equal amplitude and a Blackman window function was used. The shape of the energy-spectral-density (ESD) is now a function of:

$$\Delta f = f_{NLOS} - f_{LOS}$$

and

$$\Delta\phi = \phi_{NLOS} - \phi_{LOS}$$

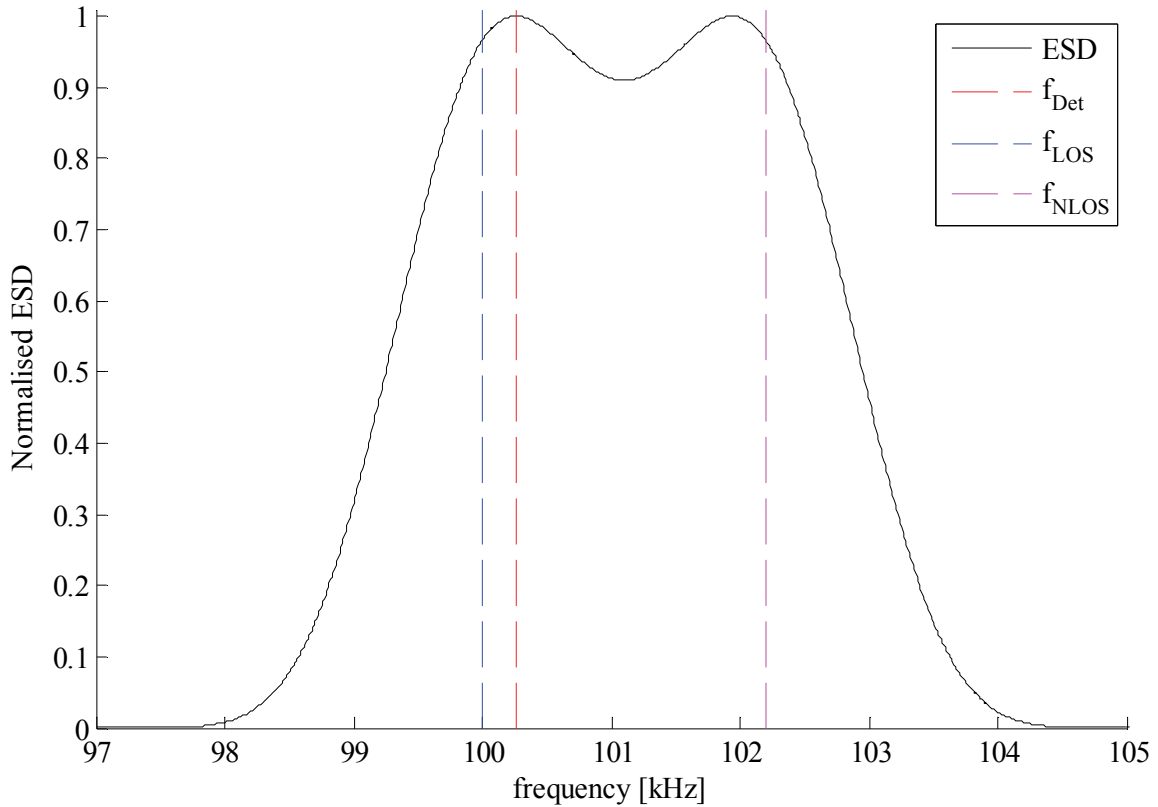


Figure 2.8 Example of frequency shift due to a closely spaced multipath tone, taken from [43]. In this example $\Delta f = 2.2$ kHz and $\Delta\phi = 0$.

The frequency of the first peak detected, f_{Det} , should be equal to the LOS frequency, f_{LOS} . Multipath interference can shift f_{Det} , as shown in Figure 2.8, causing an error ($f_{err} = f_{LOS} - f_{Det}$) in the measured frequency. The mitigation method presented in [43] measures a set of characteristics of the ESD and inputs them into an appropriately trained feedforward neural network, which outputs an estimate of f_{err} .

2.3.7 Additional Inertial Sensors

Al-Qudsi, Edwan, Joram and Ellinger investigated the feasibility of integrating an inertial measurement unit (IMU) with an FMCW system to improve performance in highly reflective

environments in [45]. Accelerometer and gyroscope triads are used in conjunction with an integration algorithm and a zero-velocity update technique (ZUPT) to produce IMU-based positioning data. This is combined with data from an FMCW time-difference-of-arrival (TDOA) module to create the final position estimate, as shown in Figure 2.9:

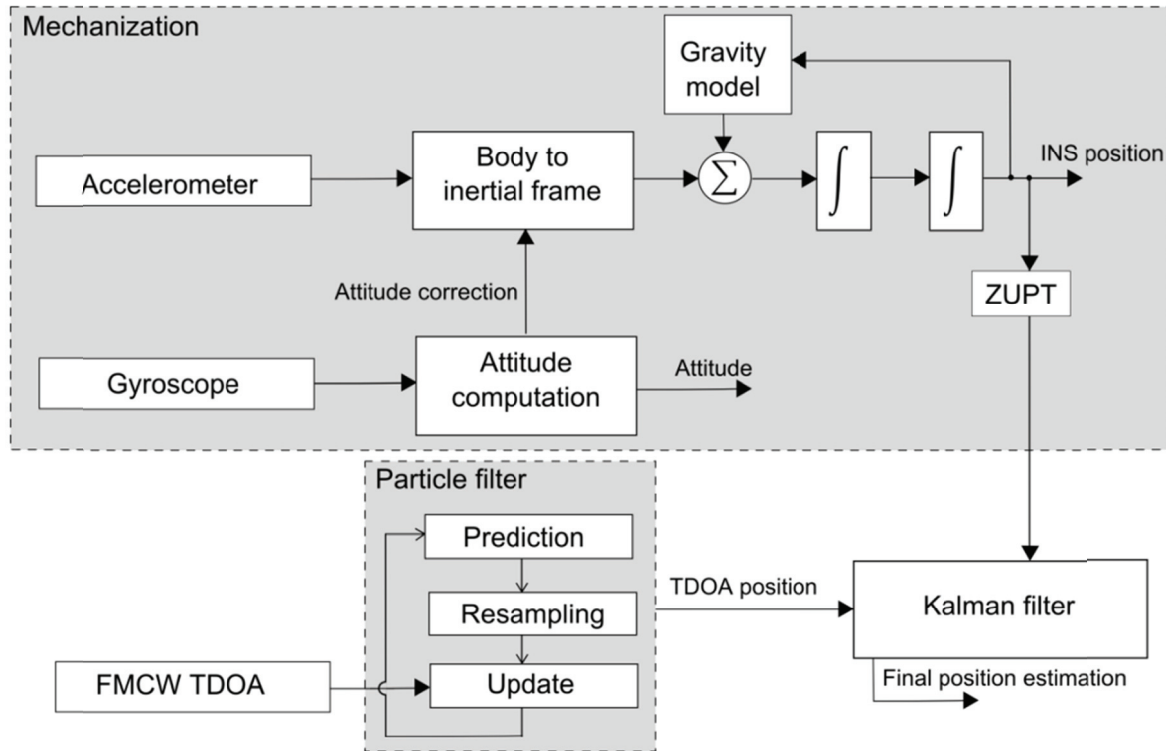


Figure 2.9 Diagram of IMU-assisted FMCW system, taken from [45].

IMU-based systems suffer from unbounded error growth, which necessitates periodic location updates. FMCW-based systems can provide location information within a fixed error margin, but suffer from loss of accuracy in challenging multipath scenarios. The scheme proposed in [45] combines the strengths of inertial and FMCW-based systems, resulting in a reduction of approximately 40% in mean positioning error.

2.3.8 System Optimisation for a Specific Environment

A well-characterised deployment environment, such as an industrial warehouse, could allow for substantial system optimisation in terms of multipath and clutter suppression. An example of this is the indoor localisation system described in [46], where several factors are used to improve system performance:

- Active tags modulate the incoming chirp signal.
- Tags are retrodirective.
- Tags reflect the incoming signal in the cross-polarisation.
- Antennas have a selective radiation pattern.

The use of active tags that modulate the incoming signal serves two purposes – multiple tags can be deployed simultaneously, since each tag is identifiable by its unique modulation frequency, and target returns are separated from clutter signals after demodulation [47]. Reflecting in the cross-polarisation further suppresses echoes from walls and other objects [48].

Retrodirectivity reduces multipath interference via two mechanisms. It ensures that potential reflective surfaces or objects (other than the interrogating radar system) are not illuminated with the LOS signal, thereby reducing the strength of multipath signals. NLOS signals are also reflected in the direction from which they came, which results in longer signal flight times and therefore greater separation in frequency (after demodulation) of LOS and multipath returns.

The system described in [46] was designed for deployment in a warehouse environment. Tags are to be placed on mobile units (forklifts) that operate at ground level, with radar units placed near the ceiling around the perimeter. Radar and tag antenna radiation patterns can therefore be more directive. Radar antenna patterns were designed to look downwards and away from the perimeter, which reduces unwanted reflections from the ceiling and walls, while the tags were designed to look upwards.

2.4 Conclusion

This chapter investigated a number of physical terrain models, ranging from simple flat ground plane models to more complex oceanic surface and vegetation models. Chapter 4 will consider this information again when deriving the effects of the environment on FMCW signals. Several multipath mitigation techniques were also described, with a number of interesting approaches being used. These will be considered in Chapter 6 when suitable mitigation methods are proposed. Now it is necessary to consider signal processing and its effects, which will be discussed in the next chapter.

Chapter 3: FMCW Signal Processing

This chapter will take a closer look at the mechanics of FMCW signal processing, starting from the basic expression for instantaneous transmitter signal (3.1) and working up to an expanded formula for the measured burst phase (3.23). Frequency-Modulated Continuous Wave (FMCW) radars transmit a continuous sinusoid signal, of which the frequency is modulated. A number of modulation schemes can be used, such as triangular, sinusoidal, saw-tooth or stepped-frequency. These modulation schemes are illustrated in Figure 3.1:

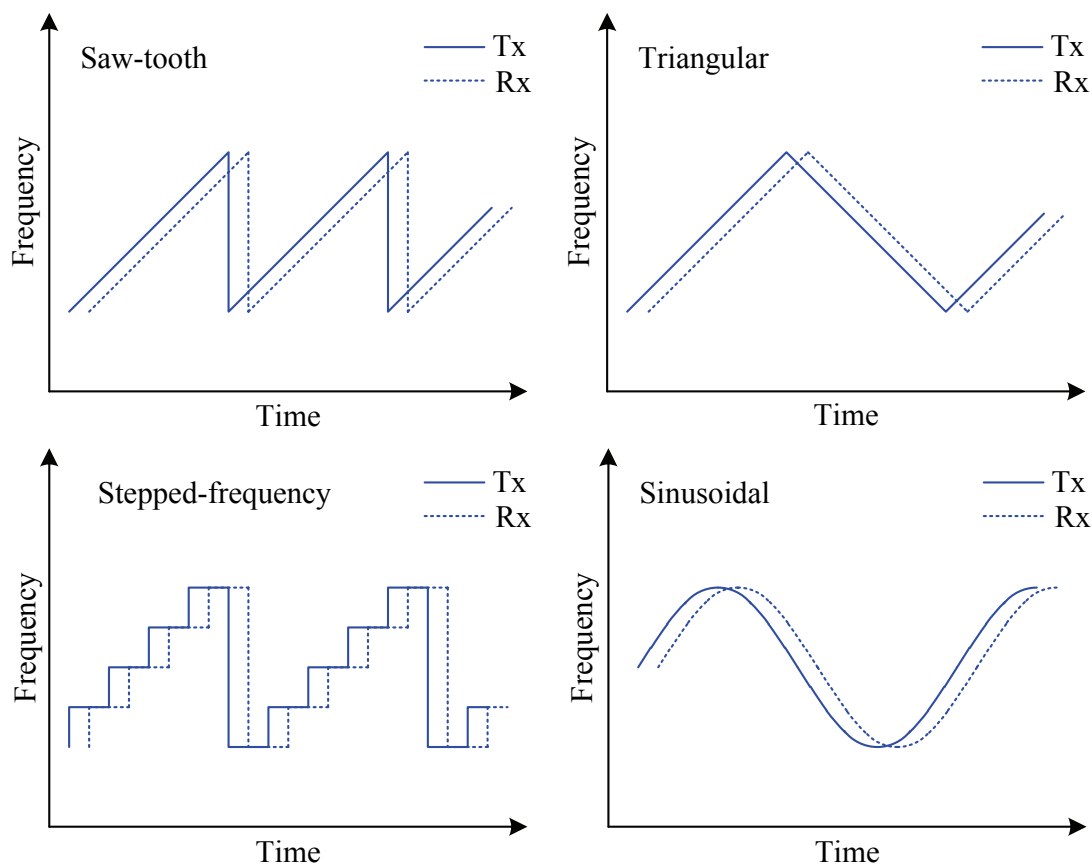


Figure 3.1 Examples of modulation schemes employed in FMCW systems.

Typical FMCW systems, such as the one depicted in Figure 3.2, compare echo signals with a copy of the transmit signal, usually by mixing the two signals and filtering out the lower side-band. This forms the base-band signal, also called the beat frequency, zero-IF signal or video signal, which contains the

range and Doppler information. Each modulation scheme will have its own signal processing methods; this chapter will focus on saw-tooth modulation (which is a popular modulation scheme and was also employed in the design of the APS radar sensor).

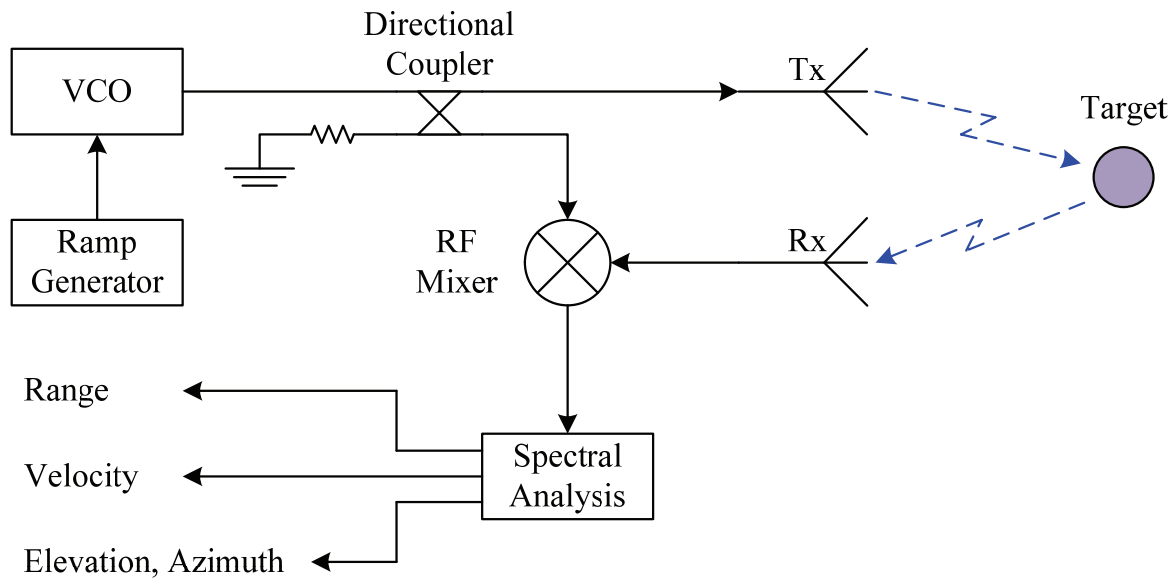


Figure 3.2 General FMCW radar system diagram.

3.1 Stationary Target

Figure 3.3 shows the saw-tooth modulation scheme, also known as Linear Frequency-Modulated Continuous Wave (LFMCW), in more detail:

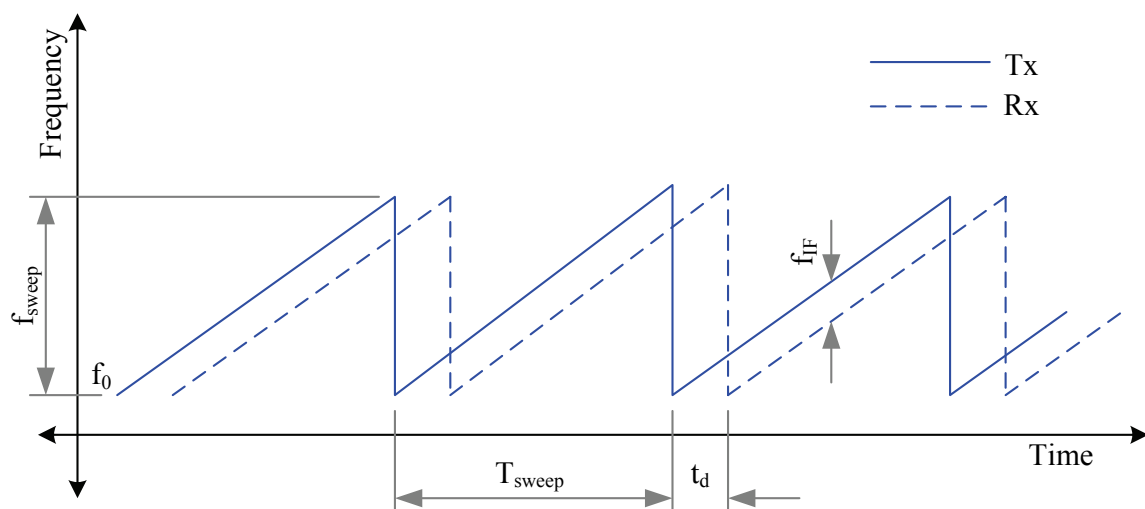


Figure 3.3 Linear Frequency-Modulated Continuous Wave modulation scheme.

Starting at f_0 , the instantaneous frequency is swept linearly up to $f_0 + f_{sweep}$ over a time period of T_{sweep} . After a time T_{rec} (during which the signal generation circuitry is reset), the next frequency sweep is generated. Instantaneous phase is obtained by integrating the instantaneous frequency; this is needed for the mathematical expression of the transmit signal given by (3.1):

$$\begin{aligned}
 s_{Tx}(t) &= A_{Tx} \sin\left(\int 2\pi f(t) dt\right) \\
 &= A_{Tx} \sin\left(2\pi \int \left(f_0 + \frac{f_{sweep}}{T_{sweep}} t\right) dt\right) \\
 &= A_{Tx} \sin(2\pi f_0 t + \pi \mu t^2 + \theta_0)
 \end{aligned} \tag{3.1}$$

where f_0 is the start frequency,

f_{sweep} is the frequency sweep range,

T_{sweep} is the duration of the sweep,

θ_0 is the initial phase and

$\mu (=f_{sweep}/T_{sweep})$ is the frequency sweep rate.

Echoes from a stationary target will be received after a delay of t_d seconds:

$$s_{Rx}(t) = A_{Rx} \sin(2\pi f_0(t - t_d) + \pi \mu(t - t_d)^2 + \theta_0) \tag{3.2}$$

$$t_d = \frac{2R}{c} \tag{3.3}$$

where R is the range (or distance) between the transceiver and the target and

c is the speed of wave propagation.

Mixing $S_{Rx}(t)$ and $S_{Tx}(t)$ and taking the lower side-band produces the zero-IF signal:

$$\begin{aligned}
 s_{IF}(t) &= A_{IF} \cos(2\pi f_0 t_d + 2\pi \mu t_d t - \pi \mu t_d^2) \\
 &= A_{IF} \cos\left(2\pi f_{IF} t + \Phi_d - 2\pi \frac{1}{2} f_{IF} t_d\right)
 \end{aligned} \tag{3.4}$$

$$f_{IF} = \mu t_d \quad (3.5)$$

$$\Phi_d = 2\pi f_0 t_d \quad (3.6)$$

where f_{IF} is the beat frequency (which is used to determine range) and

Φ_d is the phase, which will be compared to the phase of another channel to determine Angle-of-Arrival (AoA).

3.2 Moving Target

Section 3.1 derived a mathematical expression for the zero-IF signal when a stationary target is present. If the object of interest is moving, there will be a number of parameters that may also change, such as t_d , f_{IF} , Φ_d , etc. This section will investigate the effect of target movement on the base-band signal.

Assuming that the target is moving away from the transceiver at a radial velocity v , the range between the target and the transceiver will become a function of velocity, time and sweep number:

$$R(t, n) = R_0 + vnT_{rep} + vt \quad (3.7)$$

The return time-of-flight will also change:

$$\begin{aligned} t_d(t, n) &= \frac{2R(t, n)}{c} \\ &= t_{d0} + \frac{2vn}{c}T_{rep} + \frac{2v}{c}t \\ t_{d0} &= \frac{2R_0}{c} \end{aligned} \quad (3.8)$$

R_0 is the range at $t = 0$ and $n = 0$,

n is the sweep number (starting from sweep 0),

$0 \leq t \leq T_{sweep}$,

T_{rep} is the time interval between the start of consecutive sweeps ($= T_{sweep} + T_{rec}$) and

c is the speed of wave propagation.

The base-band signal, $s_{IF}(t)$, will become a function of velocity and sweep number. Substituting (3.8) into (3.4) yields the following:

$$\begin{aligned}
 s_{IF}(t, n) &= A \cos(2\pi\mu t_d t + 2\pi f_0 t_d - 2\pi \frac{1}{2} \mu t_d^2) \\
 &= A \cos \left[2\pi\mu \left(\frac{2v}{c} - \frac{2v^2}{c^2} \right) t^2 \right. \\
 &\quad \left. + 2\pi\mu \left(t_{d0} + \frac{2v}{c} n T_{rep} + \frac{f_0}{\mu} \frac{2v}{c} - \frac{2v}{c} t_{d0} - \frac{4v^2}{c^2} n T_{rep} \right) t \right. \\
 &\quad \left. + 2\pi f_0 t_{d0} + 2\pi f_0 \frac{2v}{c} n T_{rep} \right. \\
 &\quad \left. - 2\pi\mu \left(\frac{1}{2} t_{d0}^2 + \frac{2v}{c} n T_{rep} t_{d0} + \frac{2v^2}{c^2} n^2 T_{rep}^2 \right) \right] \quad (3.9)
 \end{aligned}$$

Equation (3.9) can be reorganised into a more sensible form:

$$\begin{aligned}
 s_{IF}(t, n) &= A \cos(2\pi f_{IF} t + 2\pi f_{\Delta} n t + \Phi_0 + \theta_{\Delta} n + 2\pi f_{sq} t^2 \\
 &\quad + 2\pi f_{error} t - \Phi_{error}) \quad (3.10)
 \end{aligned}$$

with:

$$f_{IF} = \mu t_{d0} \quad (3.11a)$$

$$\begin{aligned}
 f_{\Delta} &= \mu \frac{2v}{c} T_{rep} - \mu \frac{4v^2}{c^2} T_{rep} \\
 &= \mu \frac{2v}{c} T_{rep} \left(1 - \frac{2v}{c} \right) \quad (3.11b)
 \end{aligned}$$

$$\Phi_0 = 2\pi f_0 t_{d0} \quad (3.11c)$$

$$\theta_{\Delta} = 2\pi f_0 \frac{2v}{c} T_{rep} - 2\pi\mu \frac{2v}{c} T_{rep} t_{d0} \quad (3.11d)$$

$$f_{sq} = \mu \frac{2v}{c} \left(1 - \frac{v}{c} \right) \quad (3.11e)$$

$$f_{error} = \mu \left(\frac{f_0}{\mu} \frac{2v}{c} - \frac{2v}{c} t_{d0} \right) \quad (3.11f)$$

$$\begin{aligned} \Phi_{error} &= 2\pi\mu \left(\frac{1}{2} t_{d0}^2 + \frac{2v^2}{c^2} n^2 T_{rep}^2 \right) \\ &\approx \pi\mu t_{d0}^2 \end{aligned} \quad (3.11g)$$

Equation (3.10) contains a number of terms, some of which are useful for extracting telemetry information, while other terms are negligible or potential sources of errors. The beat frequency, f_{IF} , is directly related to the distance (R_θ) between radar and target. Radial velocity is obtained from θ_Δ , the change in phase between consecutive sweeps due to the change in distance. Elevation and azimuth angles can be calculated by comparing the phase (Φ_θ) of adjacent receivers. Other terms (f_Δ , f_{sq} , f_{error} and Φ_{error}) are usually considered small enough to be negligible; this will be confirmed in section 3.4

3.3 Range-Doppler Processing

FMCW radar systems typically make use of some form of spectral analysis. This can be in the form of a single Fast Fourier Transform (FFT) operation, as employed by [46]; two FFT operations (one FFT for the up-chirp and another for the down-chirp in triangular FMCW systems), as implemented in [17] and [19]; or a two-dimensional FFT operation, as presented in [49], [50] and [51]. The APS radar sensor uses a two-dimensional FFT technique, also known as range-Doppler processing, to extract range, velocity and phase information.

Consider the following simplified expression for the zero-IF signal:

$$s_{IF}(t, n) = A \cos(2\pi f_{IF} t + \Phi_0 + \theta_\Delta n) \quad (3.12)$$

A target is detected at frequency f_{IF} , with an initial phase of Φ_0 , by analysing the spectrum after the first sweep ($n = 0$). After the second sweep the measured phase increases by θ_Δ . This change in phase (due to radial movement of the target) is used by A.G. Stove in [52] to propose a moving target indicator (MTI) for FMCW radar. It is this same change in phase between consecutive sweeps that permits the two-dimensional FFT technique proposed in [53].

The base-band signal is sampled at a rate of f_s . Each sweep produces N_R samples, with a total of N_D sweeps being combined to form a block of $N_R \times N_D$ samples. This block of data, referred to as a burst, will be subjected to range-Doppler processing.

The first step is illustrated in Figure 3.4. Every row of samples (with each row containing all the samples from a single sweep) is subjected to an FFT operation, often called the range FFT. The result is an $N_R \times N_D$ block of complex values, with each row containing the spectral data of the corresponding sweep's base-band signal.

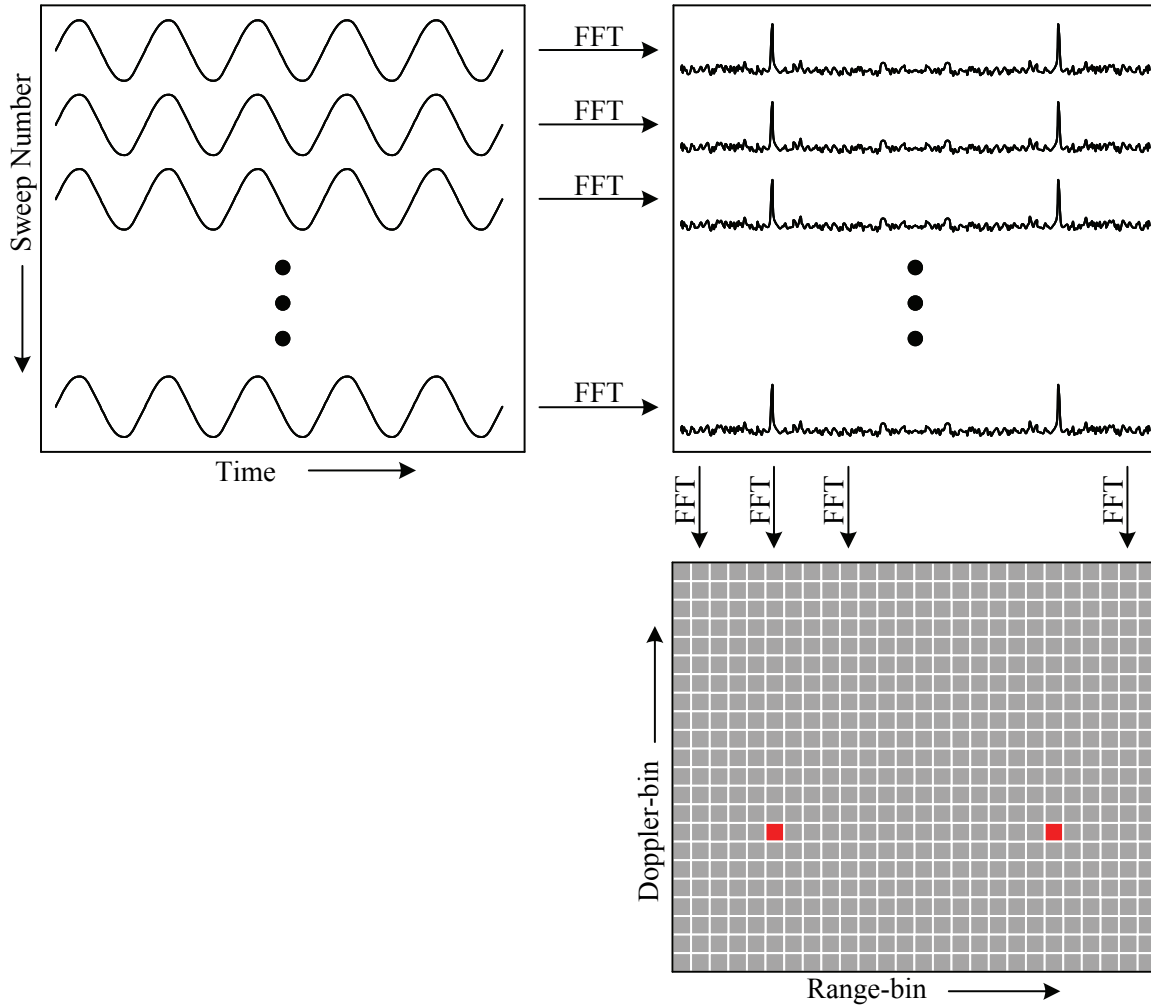


Figure 3.4 Illustration of the two-dimensional FFT (range-Doppler) processing method.

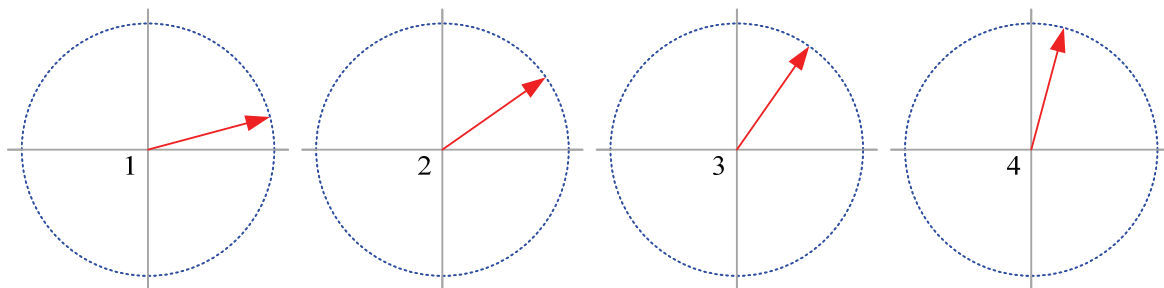


Figure 3.5 Progression of phasors after range-FFT for consecutive sweeps. A range-bin's amplitude will remain (almost) constant for consecutive sweeps, but if the target is moving the phase will change.

The second step is a Doppler FFT, also shown in Figure 3.4. Each column can be thought of as a progressive series of phasors (illustrated in Figure 3.5), with the magnitude representing the echo signal strength for the corresponding range and the phase representing the relative number of wavelengths travelled. A change in phase between consecutive sweeps is therefore equivalent to a change in distance travelled by the transmit and echo signals; this is why the Doppler FFT can be used to determine velocity.

Range-Doppler processing produces an $N_R \times N_D$ array of complex values, often referred to as a range-Doppler map. Target detections correspond to local maxima, with range and velocity determined by the target's position relative to the range and Doppler axes, illustrated in Figure 3.6.

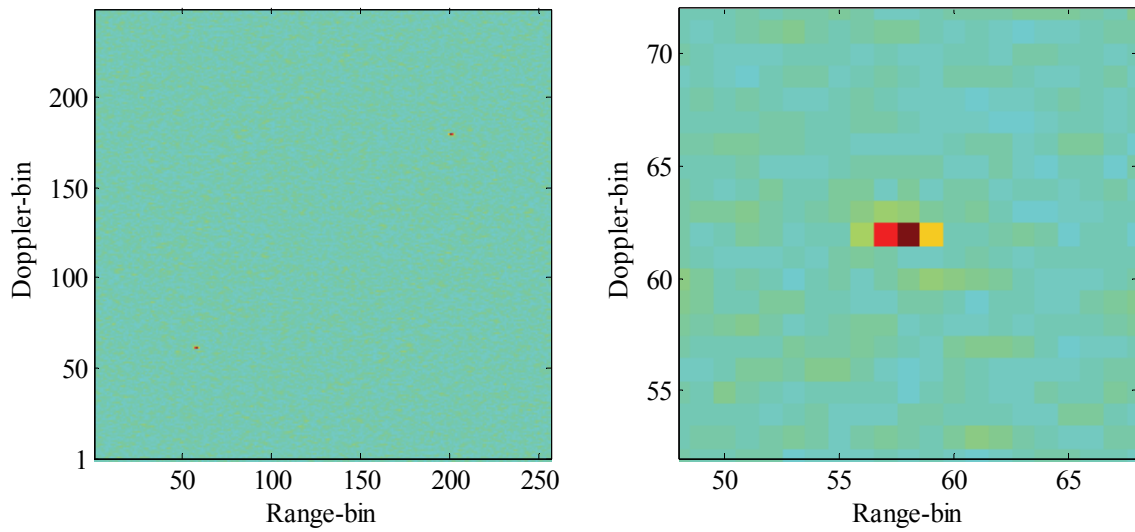


Figure 3.6 Example of a range-Doppler map. The image on the left shows the entire map, while the image on the right has been magnified to show a detection.

3.3.1 Range FFT

The zero-IF signal from each sweep is sampled at a rate of f_s to produce N_R samples. Assuming that f_{sq} is small enough to be omitted:

$$\begin{aligned}
 s_{IF}(t, n) &\approx A \cos(2\pi f_{IF}t + 2\pi f_{\Delta}nt + 2\pi f_{error}t + \Phi_0 \\
 &\quad + \theta_{\Delta}n - \Phi_{error}) \\
 &= A \cos(2\pi f_k t + 2\pi f_q t + 2\pi f_{\Delta}nt + \theta_{\Delta}n + \Phi_1)
 \end{aligned} \tag{3.13}$$

with

$$f_k = \frac{f_s}{N_R} k \quad \left[k = 0, 1, 2 \dots \frac{N_R}{2} \right] \quad (3.14a)$$

$$f_q = f_{IF} + f_{error} - f_k = \frac{f_s}{N_R} q \quad \left[-\frac{1}{2} \leq q \leq \frac{1}{2} \right] \quad (3.14b)$$

$$f_\Delta = \frac{f_s}{N_R} p \quad (3.14c)$$

$$\Phi_1 = \Phi_0 - \Phi_{error} \quad (3.14d)$$

where f_k is the range-bin frequency and is a multiple of the fundamental frequency, f_s/N_R , f_q is the remaining fraction of the fundamental frequency, and p encapsulates f_Δ .

Converting from continuous time to discrete time:

$$t = \frac{r}{f_s} \quad [r = 0, 1, 2 \dots N_R - 1] \quad (3.15)$$

$$s_{IF}(r, n) = A \cos \left(2\pi \frac{rk}{N_R} + 2\pi \frac{rq}{N_R} + 2\pi \frac{rpn}{N_R} + \theta_\Delta n + \Phi_1 \right) \quad (3.16)$$

An FFT operation¹ is performed on each sweep's sampled base-band signal, the output of which is a series of complex values known as range-bins (with k denoting the number of the bin):

$$\begin{aligned} y(k, n) &= DFT\{s_{IF}(r, n)\} \\ &\triangleq \sum_{r=0}^{N_R-1} s_{IF}(r, n) e^{-\frac{i2\pi kr}{N_R}} \\ &= A_r e^{i[\theta_1 n + \theta_2]} \end{aligned} \quad (3.17)$$

The values q and k form the beat frequency and are determined by range. The change in phase between consecutive sweeps, θ_Δ , is determined by radial velocity, while the cross-term p shows the coupling between range and velocity. This coupling, also called range-Doppler coupling, can be interpreted as chirp on the range beat frequency (due to the change in range) or as chirp on the Doppler frequency (due to the changing transmitter frequency) [52]. In this study it will be lumped with θ_Δ , thereby

¹ Mathematically defined here as a Discrete Fourier Transform, DFT, which is what the FFT approximates [61].

interpreting the small change in frequency between consecutive sweeps as a change in phase after applying the FFT operation.

The two phase terms from (3.17) can now be written as:

$$\theta_1 = \theta_\Delta + \pi p \quad (3.18a)$$

$$\theta_2 = \Phi_0 - \Phi_{error} + \pi q \quad (3.18b)$$

3.3.2 Doppler FFT

After the range FFTs have been computed, a second set of Doppler FFTs is performed. For each range-bin k , all range FFT values from sweep 0 to sweep $N_D - 1$ ($n = 0, 1, 2 \dots N_D - 1$) are taken as input for the next FFT operation:

$$\begin{aligned} Y(k, b) &= DFT\{y(k, n)\} \\ &\triangleq \sum_{n=0}^{N_D-1} y(k, n) e^{-\frac{i2\pi bn}{N_D}} \\ &= \sum_{n=0}^{N_D-1} A_r e^{i[\theta_1 n + \theta_2]} e^{-\frac{i2\pi bn}{N_D}} \end{aligned} \quad (3.19)$$

Similar to the range-bin frequency f_k , the Doppler-bin frequency can be defined as:

$$\theta_b \triangleq 2\pi \frac{b}{N_D} \quad [b = 0, 1, 2 \dots N_D - 1] \quad (3.20)$$

with the remainder frequency:

$$\begin{aligned} \theta_a &\triangleq \theta_1 - \theta_b \\ &= 2\pi \frac{a}{N_D} \quad [-0.5 \leq a \leq 0.5] \end{aligned} \quad (3.21)$$

Substituting (3.20) and (3.21) into (3.19) yields:

$$\begin{aligned}
Y(k, b) &= \sum_{n=0}^{N_D-1} A_r e^{i[\theta_1 n + \theta_2]} e^{-\frac{i2\pi b n}{N_D}} \\
&= \sum_{n=0}^{N_D-1} A_r e^{i\left[2\pi \frac{b}{N_D} n + 2\pi \frac{a}{N_D} n + \theta_2 - \frac{2\pi b n}{N_D}\right]} \\
&= \sum_{n=0}^{N_D-1} A_r e^{i\left[2\pi \frac{a}{N_D} n + \theta_2\right]} \\
&= A_{rd} e^{i\Phi_{burst}}
\end{aligned} \tag{3.22}$$

The measured burst phase can now be expanded:

$$\begin{aligned}
\Phi_{burst} &= \theta_2 + \pi a \\
&= \Phi_0 - \Phi_{error} + \pi q + \pi \frac{N_D(\theta_1 - \theta_b)}{2\pi} \\
&= \Phi_0 - \Phi_{error} + \pi(f_{IF} + f_{error} - f_k) \frac{N_R}{f_s} \\
&\quad + (\theta_\Delta + \pi p - \theta_b) \frac{N_D}{2} \\
&= \Phi_0 - \Phi_{error} + f_{IF} \frac{\pi N_R}{f_s} + f_{error} \frac{\pi N_R}{f_s} - \pi k \\
&\quad + \theta_\Delta \frac{N_D}{2} + \pi f_\Delta \frac{N_R N_D}{f_s} - 2\pi \frac{b}{N_D} \frac{N_D}{2} \\
&= \Phi_0 - \Phi_{error} + f_{IF} \frac{\pi N_R}{f_s} + f_{error} \frac{\pi N_R}{f_s} - \pi k \\
&\quad + \theta_\Delta \frac{N_D}{2} + \pi f_\Delta \frac{N_R N_D}{2f_s} - \pi b
\end{aligned} \tag{3.23}$$

The measured burst phase (Φ_{burst}) consists of a number of components, of which only one term (Φ_0) is typically desired. Table 3.1 lists all the phase terms in (3.23), with a short description of each.

Each complex value of $Y(k, b)$ is referred to as a range-Doppler-bin, with the indices k and b corresponding to discrete range and Doppler axis positions. The corresponding range can be calculated as:

$$Range_{bin\ k} = \frac{cf_s}{2\mu N_R} k \quad (3.24)$$

The corresponding speed value will be:

$$Speed_{bin\ b} = \frac{cb}{2f_0 T_{rep} N_D} \quad (3.25)$$

Table 3.1 Burst phase components.

Term	Formula	Expanded Formula	Description
Φ_1	Φ_0	$2\pi f_0 t_{d0}$	Desired phase measurement.
Φ_2	$-\Phi_{error}$	$-2\pi\mu t_{d0}^2$	Additional non-linear phase.
Φ_3	$f_{IF} \frac{\pi N_R}{f_s}$	$\mu t_{d0} \frac{\pi N_R}{f_s}$	Additional phase terms added by range-FFT processing.
Φ_4	$f_{error} \frac{\pi N_R}{f_s}$	$\mu \left(\frac{f_0}{\mu} \frac{2v}{c} - \frac{2v}{c} t_{d0} \right) \frac{\pi N_R}{f_s}$	
Φ_5	$-\pi k$	$-\pi k$	
Φ_6	$\theta_\Delta \frac{N_D}{2}$	$\left(2\pi f_0 \frac{2v}{c} T_{rep} - 2\pi\mu \frac{2v}{c} T_{rep} t_{d0} \right) \frac{N_D}{2}$	Additional phase terms added by Doppler-FFT processing.
Φ_7	$\pi f_\Delta \frac{N_R N_D}{2f_s}$	$\pi\mu \frac{v}{c} T_{rep} \left(1 - \frac{2v}{c} \right) \frac{N_R N_D}{f_s}$	
Φ_8	$-\pi b$	$-\pi b$	

3.4 Confirmation of Theoretical Approximation

This section will present several simulation results to confirm the validity of (3.23), as well as explore the limits of any assumptions or simplifications made previously. These assumptions include:

- The amplitude of s_{IF} remains fairly constant for the duration of a single sweep.
- The amplitude of $y(k, n)$ remains fairly constant for the duration of an entire burst.
- Radial velocity remains fairly constant for the duration of an entire burst.
- The quadratic frequency term f_{sq} is small enough to be negligible.

- The range-Doppler coupling term f_d can be lumped with θ_d .

3.4.1 Amplitude

Figure 3.7 shows the difference between simulated burst phase² and the phase value calculated by (3.23). A very small error is observed, indicating excellent agreement between theoretical approximation and simulated measurement. A second set of graphs is shown in Figure 3.8, which investigates phase error for various velocities. It is clear that an increase in velocity also increases the discrepancy between approximation and reality. One of the assumptions mentioned previously, namely that the amplitude of $y(k,n)$ remains fairly constant, is not valid at higher velocities³.

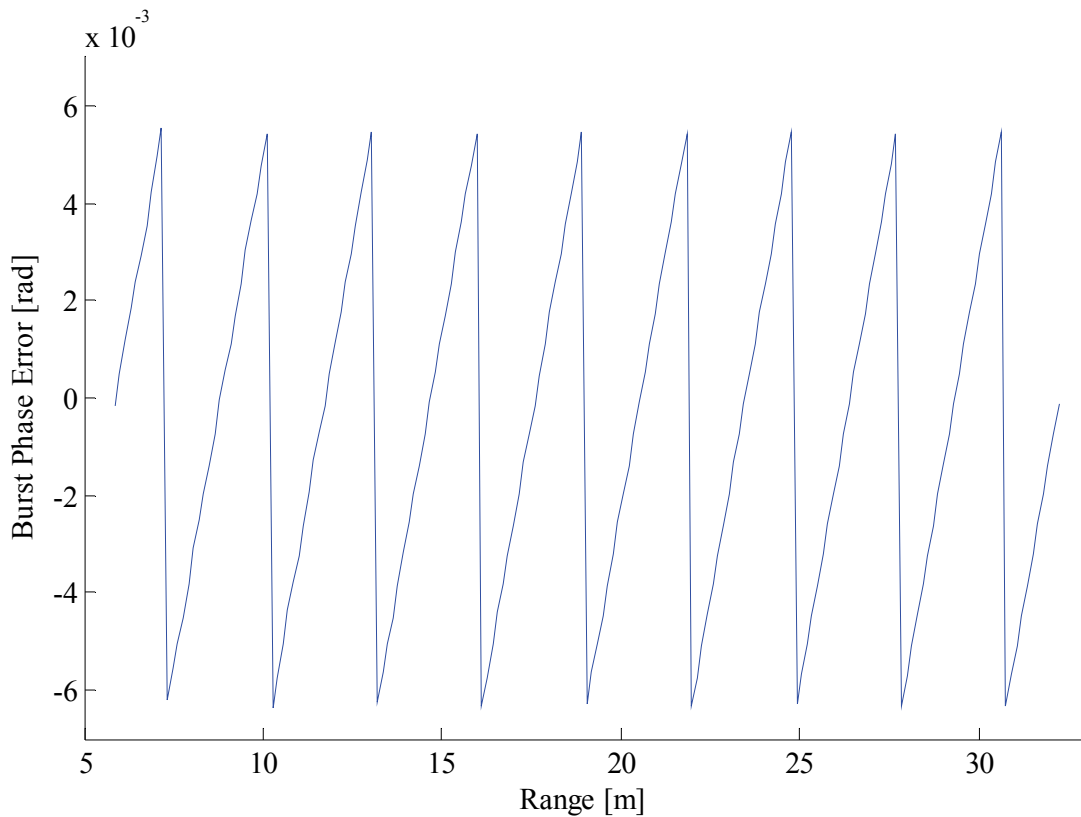


Figure 3.7 Difference between theoretically calculated and simulated burst phase.

Windowing has not been explicitly mentioned thus far; rectangular window functions have been used implicitly in the previous analyses. Most systems, including APS, use window functions to reduce spurious behaviour in the frequency domain. Figure 3.9 shows the difference between approximate and actual burst phase for several velocities, but this time using a Blackman window for both range and Doppler FFTs. A substantial reduction in error can be seen, even at much larger velocities. This can be ascribed to the change in amplitude (of $y(k,n)$) brought about by the use of a windowing function.

² Typical APS system parameters were chosen for this simulation – $f_0 = 10.1$ GHz, $N_r = 256$, $N_d = 256$, $f_{\text{sweep}} = 50$ MHz, $T_{\text{rep}} = 20$ μ s, $T_{\text{sweep}} = 16$ μ s, $T_{\text{rec}} = 2$ μ s and $f_s = 16$ MHz.

³ The change in amplitude is due to sinc/x roll-off.

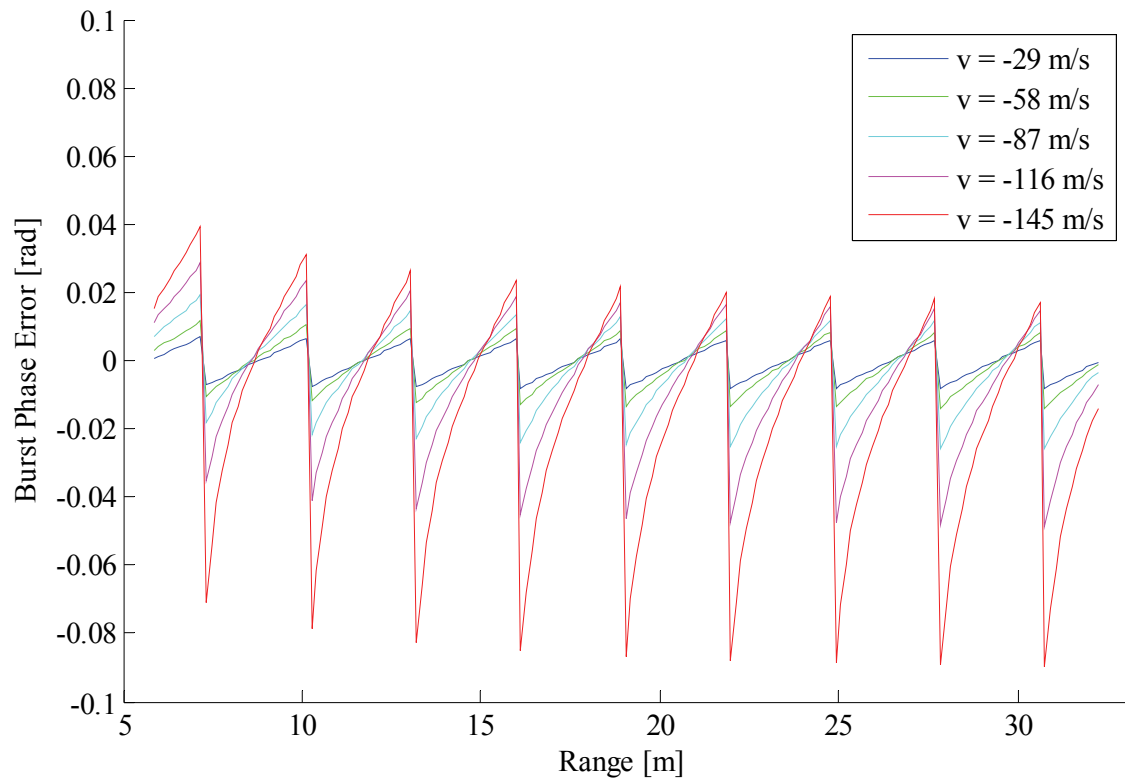


Figure 3.8 Burst phase error for various radial velocities, rectangular windowing function.

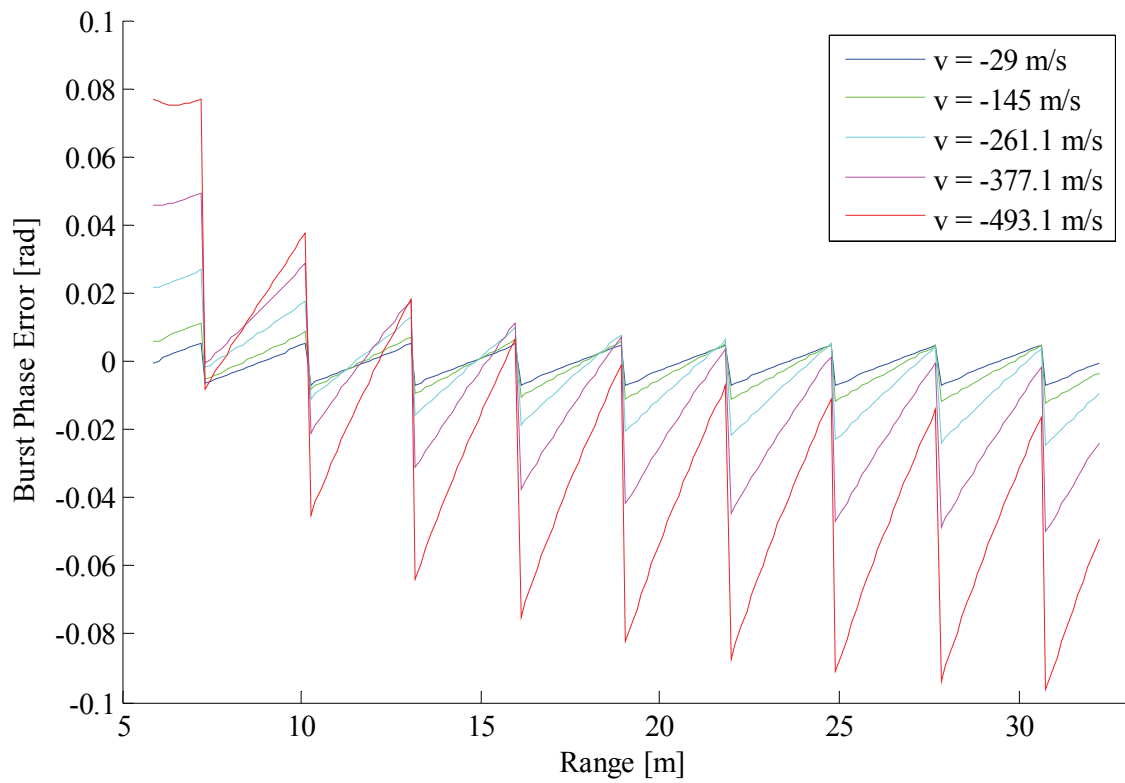


Figure 3.9 Burst phase error for various radial velocities, Blackman windowing function.

3.4.2 Quadratic Frequency

In (3.13) it was assumed that the quadratic frequency term f_{sq} is small enough to be omitted. Recall from (3.1) that a linear frequency sweep produces the following signal:

$$s_{Tx}(t) = A_{Tx} \sin(2\pi f_0 t + \pi \mu t^2 + \theta_0) \quad (3.26)$$

with

$$\mu = \frac{f_{sweep}}{T_{sweep}} \quad (3.27)$$

If we look at an equivalent expression containing f_{sq} , we can compare it to (3.26) and calculate the frequency sweep bandwidth:

$$s_{eq} = A \sin(2\pi f_{IF} t + 2\pi f_{sq} t^2)$$

$$= A \sin(2\pi f'_0 t + \pi \mu' t^2 + \theta'_0)$$

$$\Rightarrow f'_0 = f_{IF}$$

$$\theta'_0 = 0$$

$$\mu' = 2f_{sq}$$

$$= 2\mu \frac{2v}{c} \left(1 - \frac{v}{c}\right)$$

$$\approx 2 \frac{f_{sweep}}{T_{sweep}} \frac{2v}{c}$$

In both cases the sweep time is T_{sweep} , therefore

$$f'_{sweep} \approx 4 \frac{v}{c} f_{sweep}$$

The equivalent sweep bandwidth associated with f_{sq} is in the order of a few tens or hundreds of Hertz, which is small enough to ignore.

3.4.3 Other Negligible Terms

There are three terms that still need to be evaluated in this regard: f_Δ , f_{error} and Φ_{error} . Recall the expression for Doppler frequency:

$$\theta_1 = \theta_\Delta + \pi p \quad (3.28)$$

It was assumed that πp was small enough to be lumped with θ_Δ without any further consideration, but this might not be the case. If πp becomes large enough, it could cause the Doppler frequency (θ_1) to jump to an adjacent bin. A comparison between πp and Doppler-bin width is necessary.

$$\begin{aligned} \pi p &= \pi f_\Delta \frac{N_R}{f_s} \\ &= \pi \frac{N_R}{f_s} \mu \frac{2v}{c} T_{rep} \left(1 - \frac{2v}{c}\right) \\ &\approx \pi \frac{f_s T_{sweep}}{f_s} \frac{f_{sweep}}{T_{sweep}} \frac{2v}{c} T_{rep} \quad \left[N_R = \frac{T_{sweep}}{T_s} = T_{sweep} f_s \right] \\ &= 2\pi \frac{v}{c} f_{sweep} T_{rep} \end{aligned} \quad (3.29)$$

The maximum phase by which consecutive sweeps can differ from each other is 2π radians. The width of a Doppler-bin is therefore:

$$\theta_{bin} = \frac{2\pi}{N_D} \quad (3.30)$$

The ratio between πp and Doppler-bin width can be calculated:

$$\frac{\pi p}{\theta_{bin}} = \frac{v N_D f_{sweep} T_{rep}}{c} \quad (3.31)$$

Figure 3.10 plots the ratio in (3.31) as a function of radial velocity for typical APS system parameters – $N_D = 256$, $f_{sweep} = 50$ MHz and $T_{rep} = 20$ μ s. Even at moderate velocities the effect of f_Δ is enough to push a detection towards an adjacent Doppler-bin and must be accounted for if accurate velocity measurements are required.

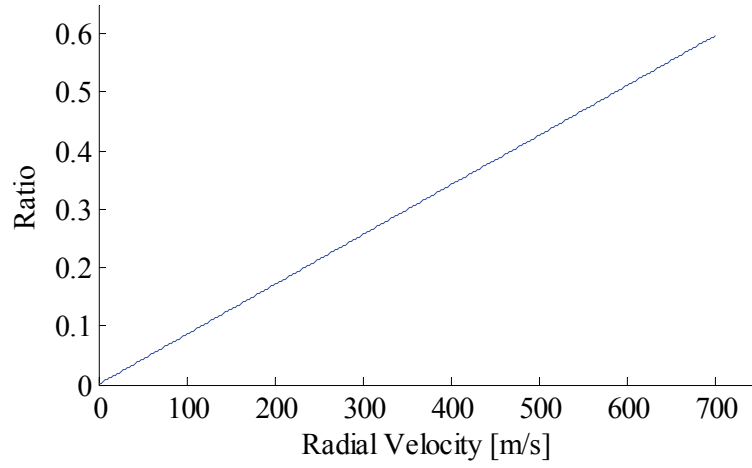


Figure 3.10 Ratio between πp and Doppler-bin width as a function of radial velocity.

For f_{error} it is necessary to look at the width of a range-bin, since a large enough deviation in frequency from f_{IF} could cause a detection to jump to an adjacent range-bin. The range-bin width is:

$$f_{bin} = \frac{f_s}{N_R} \quad (3.32)$$

f_{error} can also be simplified:

$$\begin{aligned} f_{error} &= \mu \left(\frac{f_0}{\mu} \frac{2v}{c} - \frac{2v}{c} t_{d0} \right) \\ &= \frac{2v}{c} (f_0 - f_{IF}) \\ &\approx \frac{2v}{c} f_0 \end{aligned} \quad (3.33)$$

The ratio between f_{error} and f_{bin} can be calculated:

$$\frac{f_{error}}{f_{bin}} \approx \frac{2vf_0 T_{sweep}}{c} \quad (3.34)$$

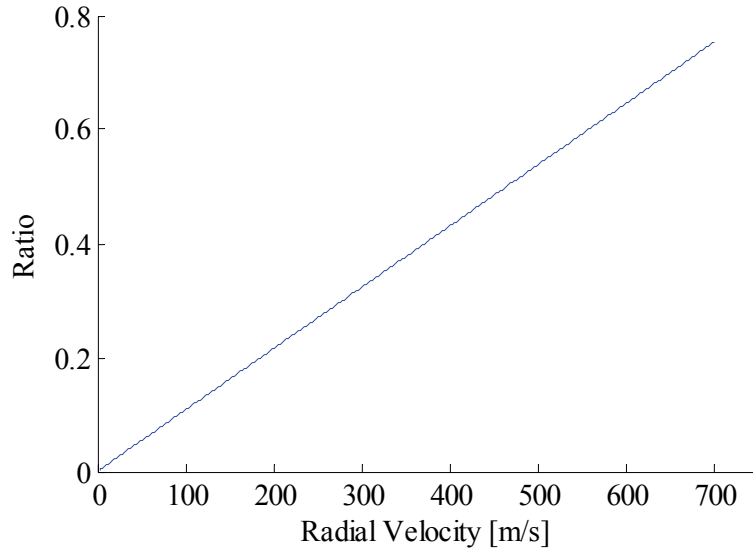


Figure 3.11 Ratio between f_{error} and range-bin frequency as a function of radial velocity.

Figure 3.11 plots this ratio as a function of radial velocity, again with typical system parameters – $f_0 = 10.1$ GHz and $T_{sweep} = 16$ μ s. As with f_d , radial velocity does have a significant effect and should be taken into consideration when accurate range measurements are needed.

The last term that must be investigated is Φ_{error} . This phase term consists of two parts:

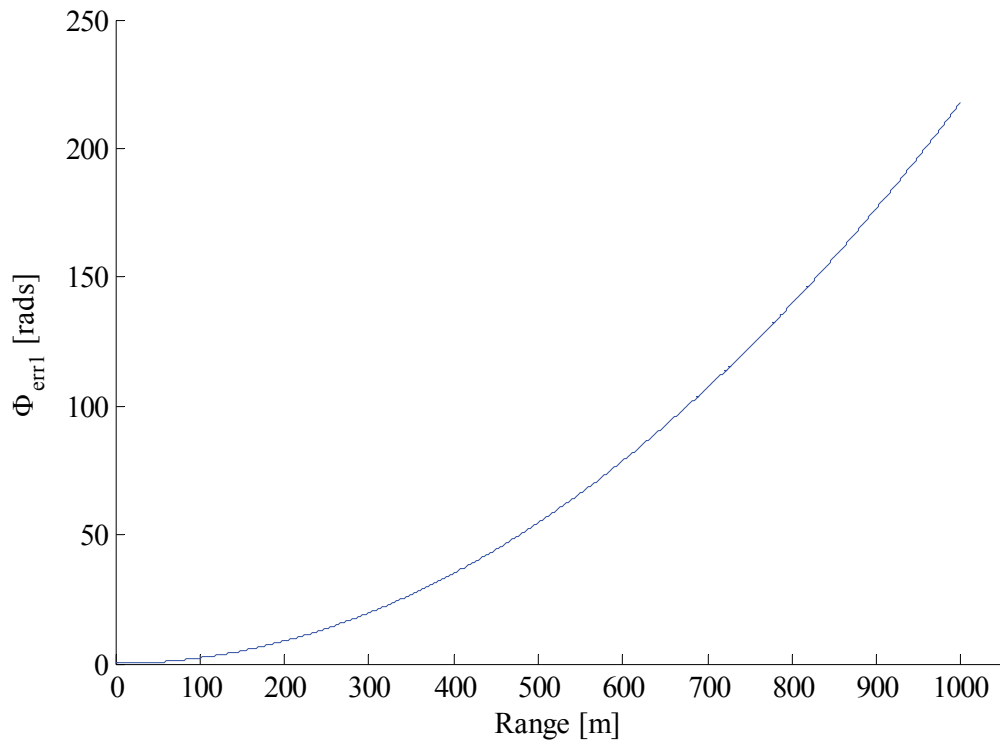
$$\Phi_{error} = \Phi_{err1} + \Phi_{err2} \quad (3.35)$$

with

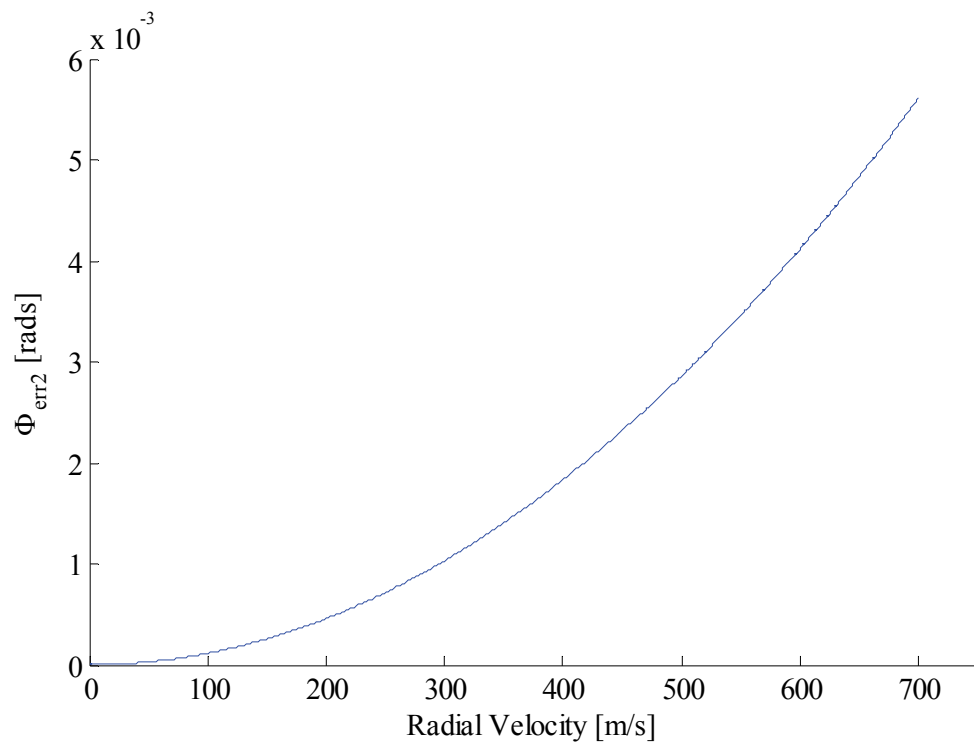
$$\Phi_{err1} = \pi\mu t_{d0}^2 \quad (3.36)$$

$$\Phi_{err2} = 2\pi\mu \frac{2v^2}{c^2} n^2 T_{rep}^2 \quad (3.37)$$

Figure 3.12 (a) and (b) shows the non-linear phase introduced by Φ_{err1} and Φ_{err2} . The first term appears to have a significant impact, but this must be considered in the context of phase interferometry. If two or more receivers are placed close to each other (for the purpose of comparing phase measurements and extracting angles) they will have almost identical values for Φ_{err1} , which would render this term negligible. The second term, Φ_{err2} , is very small and can be ignored.



(a)



(b)

Figure 3.12 Non-linear phase terms Φ_{err1} (a) and Φ_{err2} (b) as functions of radial velocity.

3.5 Conclusion

Chapter 3 discussed the two-dimensional FFT (or range-Doppler) signal processing method employed by FMCW systems. An in-depth mathematical derivation was completed, thereby revealing a number of non-ideal terms in the final burst phase measurement. Each of these terms were scrutinised to determine their potential effect on measured burst phase. All of this will be combined with a multipath interference model in the next chapter.

Chapter 4: Multipath Model

The previous chapter developed formulas for the base-band receiver signal and the measured burst phase – without taking multipath interference into account. This chapter will investigate the multipath phenomenon as observed during test-runs of APS, select an appropriate terrain model, develop a mathematical model and integrate this into the expressions for the zero-IF signal.

4.1 Terrain Model Selection

Terrain model selection can be influenced by a number of factors, such as physical deployment environment, operating frequency and coverage area. A radar system deployed in a maritime scenario might have to take the curvature of the earth into consideration, while automotive radar will most likely assume a flat ground surface. APS was designed for combat environments, with a relatively small (less than 400 m) coverage area. Any ground reflections can consequently be assumed to be from a flat surface.

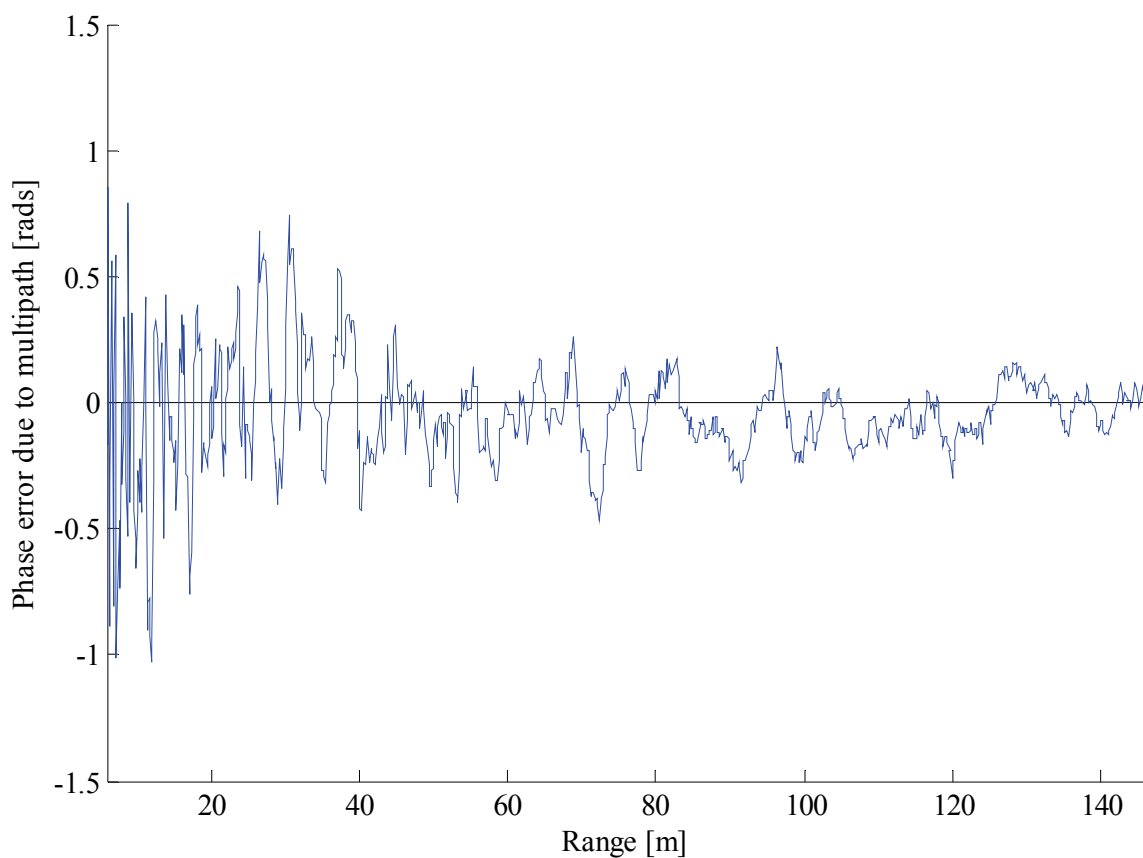


Figure 4.1 Simulated phase error due to diffuse multipath interference.

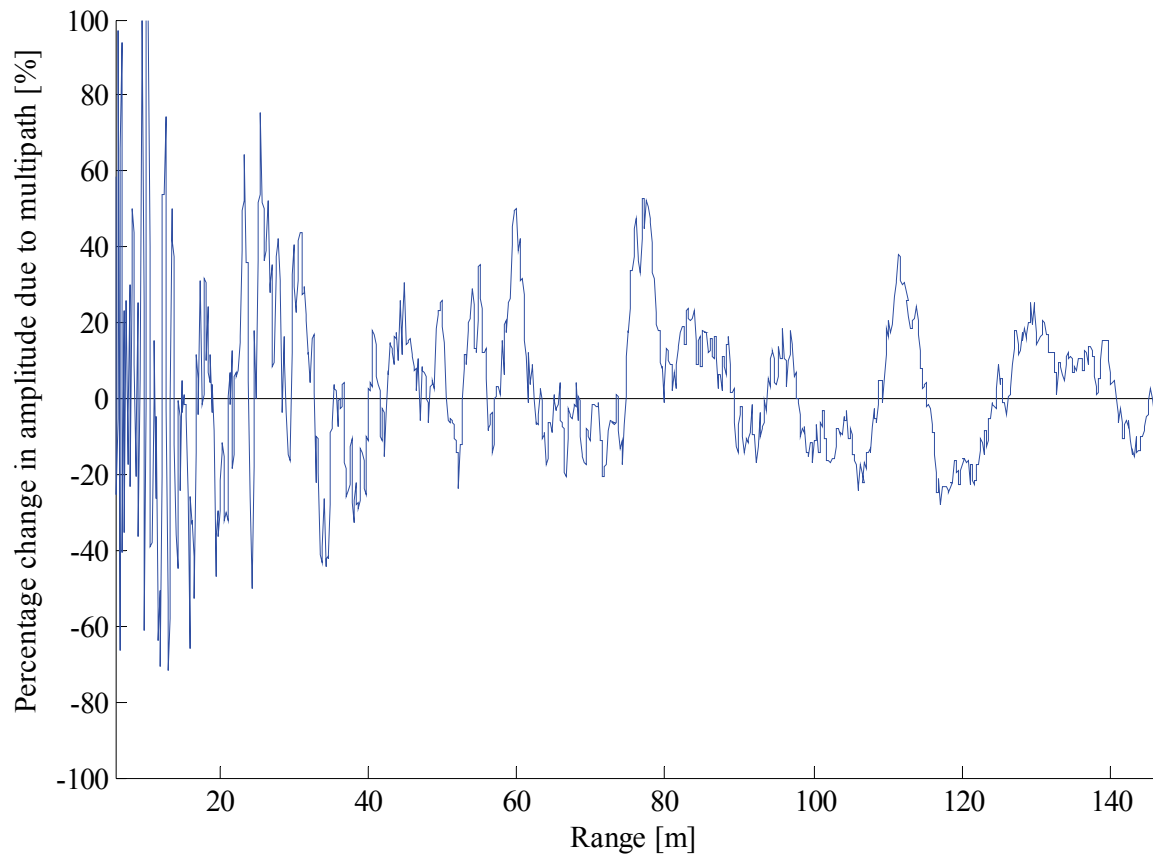


Figure 4.2 Simulated change in amplitude due to diffuse multipath interference.

Figure 4.1 and Figure 4.2 illustrate the effects of diffuse multipath interference on the measured burst phase and signal amplitude. The phase error (shown in Figure 4.1) exhibits random behaviour, which is what one would expect under diffuse multipath conditions. Compare this to the phase error produced by specular multipath, shown in Figure 4.3. Under specular conditions multipath signals combine coherently, which can lead to large phase errors that persist for longer periods of time (such as the phase error at a range of 80 - 120 m).

This can also be seen when looking at the change in amplitude. Figure 4.2 shows the change in received signal amplitude when diffuse multipath is present. Random behaviour can again be seen, as one would expect under such conditions. Compare again to the specular case, shown in Figure 4.4. Larger changes in amplitude occur when signals combine constructively or destructively, which could lead to a reduction in signal-to-noise ratio or even loss of signal.

Most practical scenarios exhibit a combination of diffuse and specular multipath. While diffuse multipath will most certainly degrade measurement accuracy to some extent, practical observations show that specular multipath is the most problematic, which is why this study has opted for the Smooth Flat Surface terrain model (described in Chapter 2).

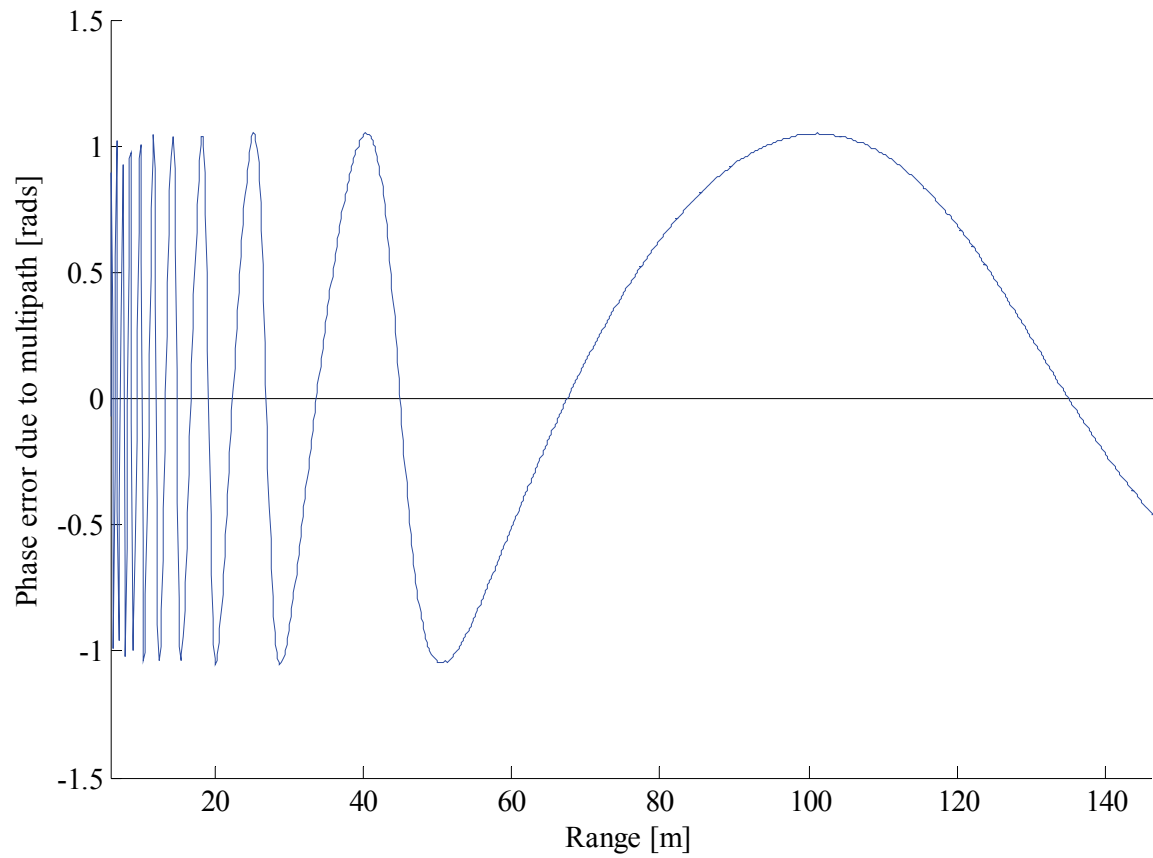


Figure 4.3 Simulated phase error due to specular multipath ($\Gamma = 0.5$).

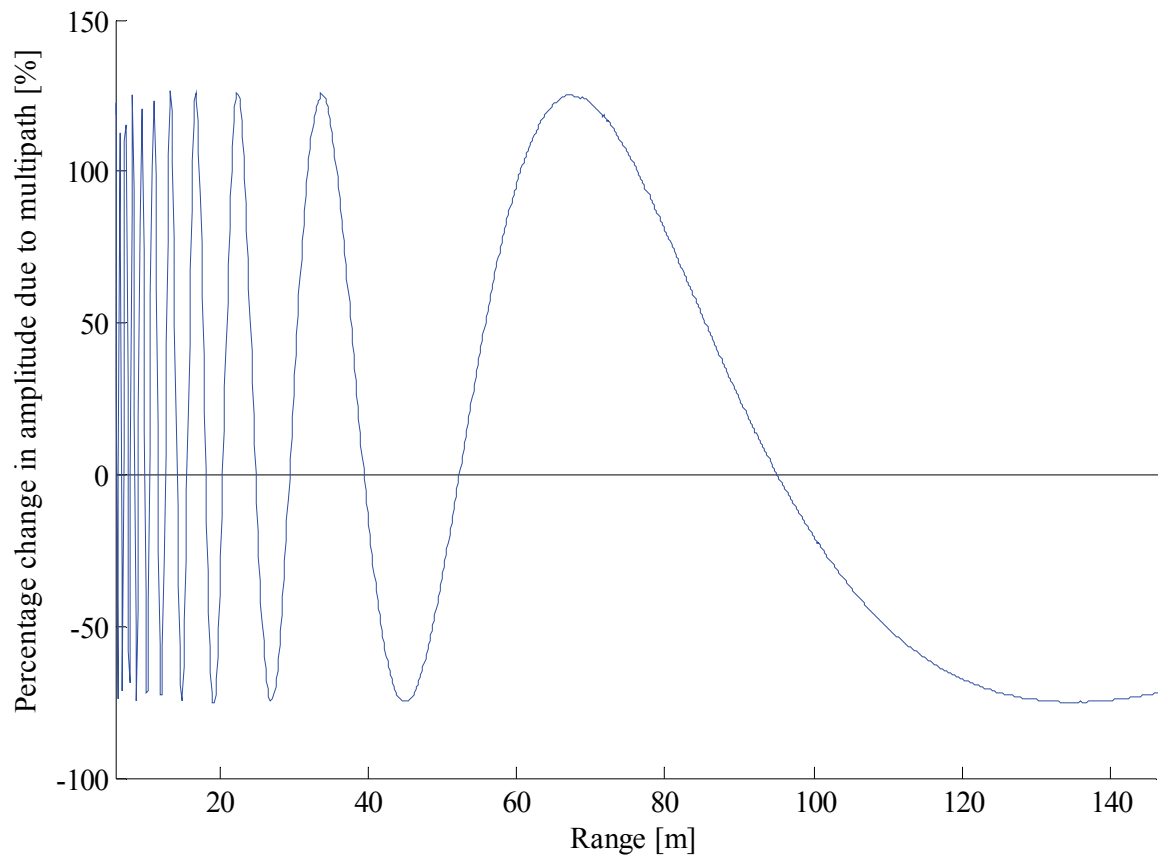


Figure 4.4 Simulated change in amplitude due to specular multipath ($\Gamma = 0.5$).

4.2 Specular Multipath Model

Specular multipath allows for the use of ray-tracing techniques from classical optics. Recall the four possible signal paths for a smooth, flat terrain (shown in Figure 4.5):

1. Direct from transmitter to target, direct from target to receiver.
2. Direct from transmitter to target, reflection from target to receiver.
3. Reflection from transmitter to target, direct from target to receiver.
4. Reflection from transmitter to target, reflection from target to receiver.

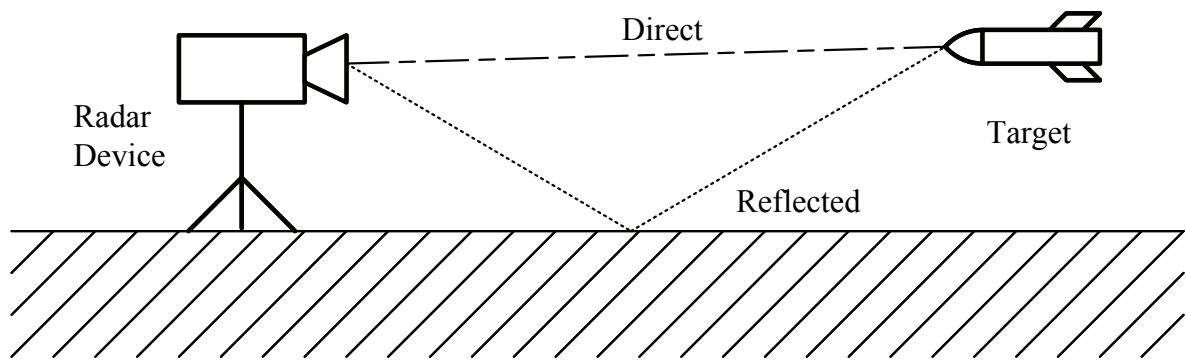


Figure 4.5 Illustration of possible signal paths.

These four signal paths result in four FMCW base-band signal components:

$$s_1(t) = A_1 \cos(2\pi f_{IF1} t + \Phi_{d1} - \pi f_{IF1} t_{d1}) \quad (4.1a)$$

$$s_2(t) = A_2 \cos(2\pi f_{IF2} t + \Phi_{d2} - \pi f_{IF2} t_{d2} + \theta_{\Gamma 2}) \quad (4.1b)$$

$$s_3(t) = A_3 \cos(2\pi f_{IF3} t + \Phi_{d3} - \pi f_{IF3} t_{d3} + \theta_{\Gamma 3}) \quad (4.1c)$$

$$s_4(t) = A_4 \cos(2\pi f_{IF4} t + \Phi_{d4} - \pi f_{IF4} t_{d4} + \theta_{\Gamma 4}) \quad (4.1d)$$

with:

$$s_{IF}(t) = s_1(t) + s_2(t) + s_3(t) + s_4(t) \quad (4.2)$$

A number of approximations can be made, detailed below ((4.3a) - (4.3j)), which will allow the signal components in (4.2) to be combined into a single expression.

$$A_2 = A_3 = A_1 \Gamma \quad (4.3a)$$

$$A_4 = A_1 \Gamma^2 \quad (4.3b)$$

$$\theta_{\Gamma 2} = \theta_{\Gamma 3} = \theta_{\Gamma} \quad (4.3c)$$

$$\theta_{\Gamma 4} = 2\theta_{\Gamma} \quad (4.3d)$$

$$f_{IF2} = f_{IF3} = f_{IF1} + f_{IF\Delta} \quad (4.3e)$$

$$f_{IF4} = f_{IF1} + 2f_{IF\Delta} \quad (4.3f)$$

$$\Phi_{d2} = \Phi_{d3} = \Phi_{d1} + \Phi_{\Delta} \quad (4.3g)$$

$$\Phi_{d4} = \Phi_{d1} + 2\Phi_{\Delta} \quad (4.3h)$$

$$t_{d2} = t_{d3} = t_{d1} + t_{\Delta} \quad (4.3i)$$

$$t_{d4} = t_{d1} + 2t_{\Delta} \quad (4.3j)$$

These approximations can be made in the case of specular multipath. Whenever a transmit or echo signal is reflected by an appropriate surface, it undergoes a change in amplitude (represented here by the factor Γ) and a change in phase (represented by the additional phase term θ_{Γ}). Together, these two terms form the complex reflection coefficient. It is furthermore assumed that the reflection coefficient remains constant for the forward scattering and echo signal paths. The base-band signal components can now be written as:

$$\begin{aligned} s_1(t) &= A_1 \cos(2\pi f_{IF1}t + \Phi_{d1} - \pi f_{IF1}t_{d1}) \\ &= A_1 \cos(X) \end{aligned} \quad (4.4)$$

$$\begin{aligned}
 s_2(t) &= s_3(t) \\
 &= A_1 \Gamma \cos(2\pi f_{IF1}t + \Phi_{d1} - \pi f_{IF1}t_{d1} \\
 &\quad + (2\pi f_{IF\Delta}t + \Phi_{\Delta} - \pi f_{IF1}t_{\Delta} - \pi f_{IF\Delta}t_{d1} - \pi f_{IF\Delta}t_{\Delta} + \theta_{\Gamma})) \\
 &= A_1 \Gamma \cos(X + Y)
 \end{aligned} \tag{4.5}$$

$$\begin{aligned}
 s_4(t) &= A_1 \Gamma^2 \cos(2\pi f_{IF1}t + \Phi_{d1} - \pi f_{IF1}t_{d1} \\
 &\quad + 2(2\pi f_{IF\Delta}t + \Phi_{\Delta} - \pi f_{IF1}t_{\Delta} - \pi f_{IF\Delta}t_{d1} - \pi f_{IF\Delta}t_{\Delta} + \theta_{\Gamma}) \\
 &\quad - 2\pi f_{IF\Delta}t_{\Delta}) \\
 &= A_1 \Gamma^2 \cos(X + 2Y - 2\pi f_{IF\Delta}t_{\Delta}) \\
 &\approx A_1 \Gamma^2 \cos(X + 2Y)
 \end{aligned} \tag{4.6}$$

with

$$X = 2\pi f_{IF1}t + \Phi_{d1} - \pi f_{IF1}t_{d1} \tag{4.7}$$

$$Y = 2\pi f_{IF\Delta}t + \Phi_{\Delta} - \pi f_{IF1}t_{\Delta} - \pi f_{IF\Delta}t_{d1} - \pi f_{IF\Delta}t_{\Delta} + \theta_{\Gamma} \tag{4.8}$$

Substituting (4.4), (4.5) and (4.6) into (4.2) yields:

$$\begin{aligned}
 s_{IF}(t) &\approx A_1 \cos(X) + 2A_1 \Gamma \cos(X + Y) + A_1 \Gamma^2 \cos(X + 2Y) \\
 &= A_1 [\cos(X) + 2\Gamma \cos(X) \cos(Y) - 2\Gamma \sin(X) \sin(Y) \\
 &\quad + \Gamma^2 \cos(X) \cos(2Y) - \Gamma^2 \sin(X) \sin(2Y)] \\
 &= A_1 [1 + 2\Gamma \cos(Y) + \Gamma^2 \cos(2Y)] \cos(X)
 \end{aligned}$$

$$-A_1[2\Gamma \sin(Y) + \Gamma^2 \sin(2Y)]\sin(X) \quad (4.9)$$

The following trigonometric identity can be used to simplify (4.9):

$$\begin{aligned} A\cos(\varphi + \theta) &= A\cos\varphi\cos\theta - A\sin\varphi\sin\theta \\ &= B\cos\varphi - C\sin\varphi \end{aligned} \quad (4.10a)$$

$$A^2 = B^2 + C^2 \quad (4.10b)$$

$$\tan\theta = \frac{C}{B} \quad (4.10c)$$

Applying (4.10) to (4.9) produces:

$$\begin{aligned} s_{IF}(t) &\approx A_1 M \cos(X + \Phi_{mp}) \\ &= A_1 M \cos(2\pi f_{IF1}t + \Phi_{d1} - \pi f_{IF1}t_{d1} + \Phi_{mp}) \end{aligned} \quad (4.11)$$

with

$$\begin{aligned} M &= \sqrt{(1 + 2\Gamma \cos(Y) + \Gamma^2 \cos(2Y))^2 + (2\Gamma \sin(Y) + \Gamma^2 \sin(2Y))^2} \\ &= \sqrt{[(1 + \Gamma \cos(Y))^2 + \Gamma^2 \sin^2(Y)]^2} \\ &= (1 + \Gamma \cos(Y))^2 + \Gamma^2 \sin^2(Y) \end{aligned} \quad (4.12)$$

and

$$\tan(\Phi_{mp}) = \frac{2\Gamma \sin(Y) + \Gamma^2 \sin(2Y)}{1 + 2\Gamma \cos(Y) + \Gamma^2 \cos(2Y)} \quad (4.13)$$

The presence of specular multipath interference will therefore change the amplitude of the base-band signal by a factor of M and the phase by the addition of Φ_{mp} . M and Φ_{mp} are periodic functions of Y , illustrated here in Figure 4.6 and Figure 4.7:

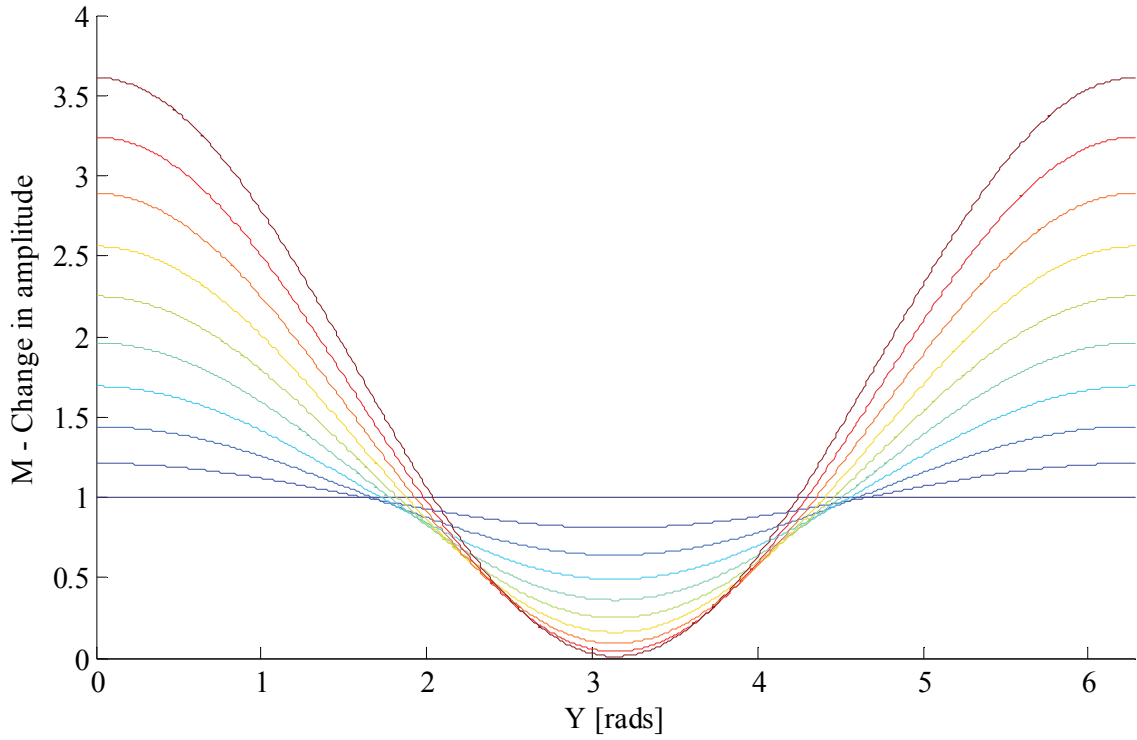


Figure 4.6 Change in base-band signal amplitude as a function of Y for various reflection coefficients (blue denotes a smaller coefficient and red a larger coefficient).

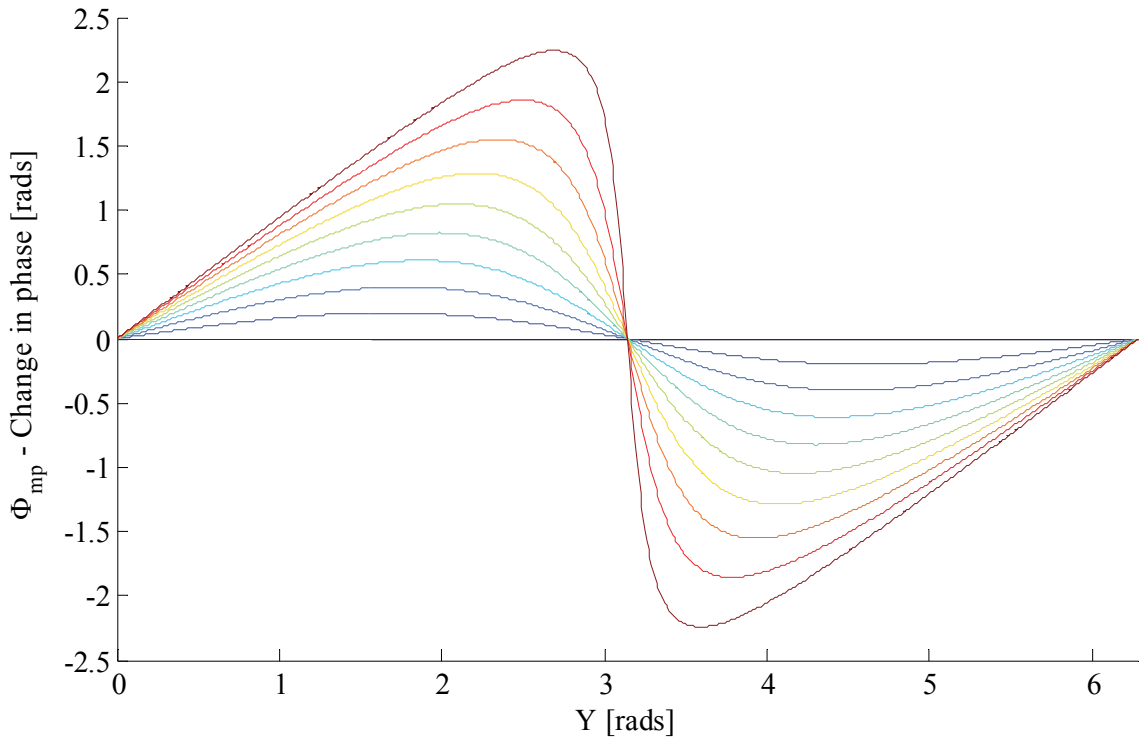


Figure 4.7 Change in base-band signal phase as a function of Y for various reflection coefficients (blue denotes a smaller coefficient and red a larger coefficient).

4.3 Integration of Multipath Model

Section 4.2 showed that the base-band signal's amplitude changes by a factor M and its phase by the addition of Φ_{mp} . Both M and Φ_{mp} will change in value as the target's position changes with time. The following simplifications will therefore be made when taking multipath into account:

- The change in M is small enough that it may be considered constant for the duration of several sweeps.
- The change in Φ_{mp} is small enough that it may be considered constant for the duration of one sweep.
- The increase (or decrease) in Φ_{mp} between consecutive sweeps ($\Phi_{\Delta mp}$) remains constant for several sweeps.

With these simplifications, (3.10) can be updated to include multipath:

$$\begin{aligned}
 s_{IF,mp}(t, n) &= AM \cos(2\pi f_{IF}t + 2\pi f_{\Delta}nt + \Phi_0 + \theta_{\Delta}n + 2\pi f_{sq}t^2 \\
 &\quad + 2\pi f_{error}t - \Phi_{error} + \Phi_{mp} + \Phi_{\Delta mp}n) \\
 &\approx AM \cos(2\pi f_{IF}t + 2\pi f_{\Delta}nt + \Phi_0 + \theta_{\Delta}n \\
 &\quad + 2\pi f_{error}t - \Phi_{error} + \Phi_{mp} + \Phi_{\Delta mp}n)
 \end{aligned} \tag{4.14}$$

where M is the change in amplitude due to multipath at $t = 0$ and $n = 0$,

Φ_{mp} is the change in phase due to multipath at $t = 0$ and $n = 0$, and

$\Phi_{\Delta mp}$ is the difference in multipath phase between consecutive sweeps.

The formulas for range-Doppler processing can be updated to include multipath. The output of the range FFT, (3.17), can be rewritten as:

$$\begin{aligned}
 y(k, n) &= DFT\{s_{IF,mp}(r, n)\} \\
 &\triangleq \sum_{r=0}^{N_R-1} s_{IF,mp}(r, n) e^{-\frac{i2\pi kr}{N_R}} \\
 &= A_r M e^{i[\theta_1 n + \theta_2]}
 \end{aligned} \tag{4.15}$$

with:

$$\theta_1 = \theta_\Delta + \pi p + \Phi_{\Delta mp} \quad (4.16a)$$

$$\theta_2 = \Phi_0 - \Phi_{error} + \pi q + \Phi_{mp} \quad (3.18b)$$

The formula for burst phase, (3.23), will also change:

$$\begin{aligned} \Phi_{burst} &= \theta_2 + \pi a \\ &= \Phi_0 - \Phi_{error} + \pi q + \Phi_{mp} + \pi \frac{N_D(\theta_1 - \theta_b)}{2\pi} \\ &= \Phi_0 - \Phi_{error} + \pi(f_{IF} + f_{error} - f_k) \frac{N_R}{f_s} + \Phi_{mp} \\ &\quad + (\theta_\Delta + \pi p + \Phi_{\Delta mp} - \theta_b) \frac{N_D}{2} \\ &= \Phi_0 - \Phi_{error} + \Phi_{mp} + f_{IF} \frac{\pi N_R}{f_s} + f_{error} \frac{\pi N_R}{f_s} - \pi k \\ &\quad + \theta_\Delta \frac{N_D}{2} + \pi f_\Delta \frac{N_R N_D}{2 f_s} + \Phi_{\Delta mp} \frac{N_D}{2} - \pi b \end{aligned} \quad (4.17)$$

The first multipath phase term, Φ_{mp} , will clearly have a significant impact on burst phase measurements. The second term, $\Phi_{\Delta mp}$, is dependent on environmental factors and target velocity, which makes it more difficult to quantify. There are two main concerns – the effect of $\Phi_{\Delta mp}$ on Doppler frequency (4.16a) and the change in measured burst phase (4.17).

Figure 4.8 shows the ratio between $\Phi_{\Delta mp}$ and Doppler-bin width for typical APS system parameters and a reflection coefficient value $|I|$ of 0.5. Several radial velocities are depicted. It is clear that multipath interference has the potential to influence Doppler frequency substantially, especially at closer ranges.

Figure 4.9 illustrates the effect of $\Phi_{\Delta mp}$ on measured burst phase. Significant changes in measured phase can be seen, even at moderate velocities.

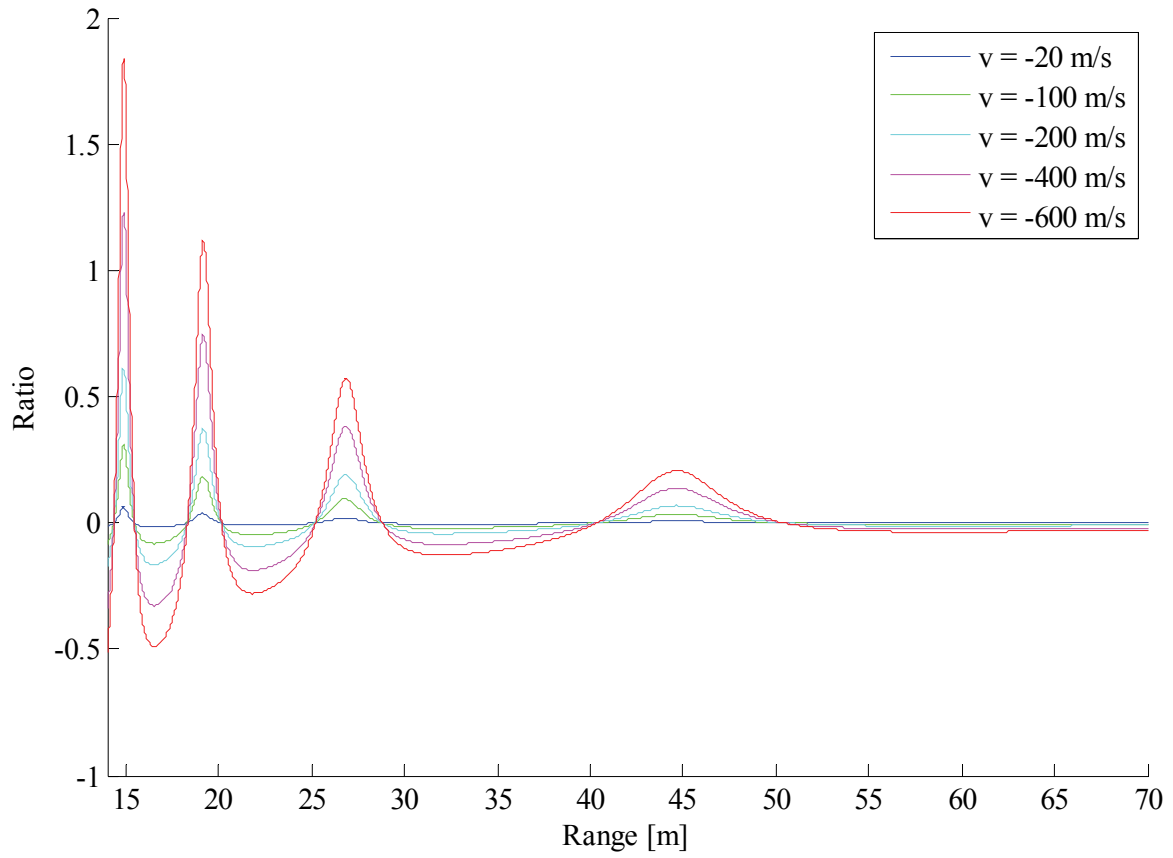


Figure 4.8 Ratio between $\Phi_{\Delta mp}$ and Doppler-bin width as a function of range and for various radial velocities.

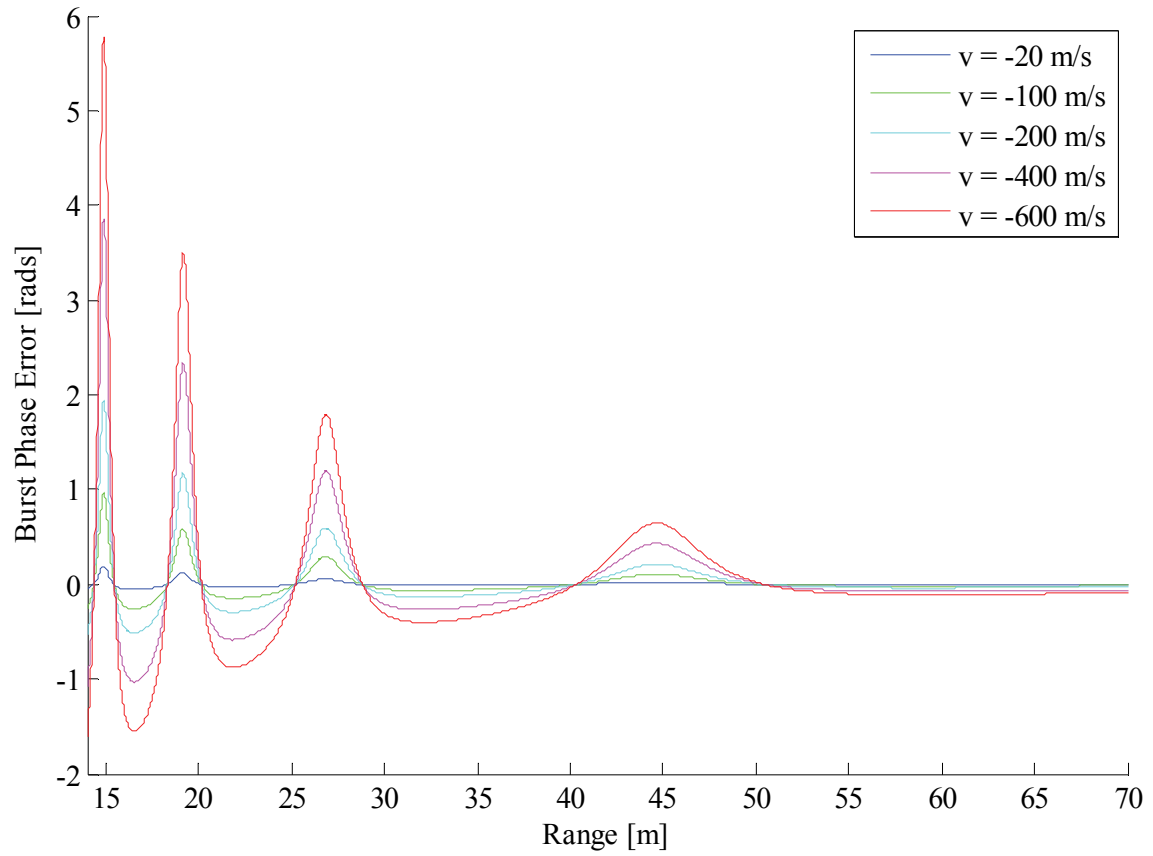


Figure 4.9 Burst phase error due to specular multipath for various radial velocities.

4.4 Confirmation of Integrated Model

This section will present a number of simulation results to validate the formulas that were derived in the previous sections. All simulations were done in Matlab[®].

The first set of results, presented in Figure 4.10, shows the error in measured burst phase for various magnitudes of reflection coefficient and a relatively low radial velocity. Excellent correlation can be seen between the predicted theoretical phase error (Φ_{mp} from (4.13)) and the simulated phase error.

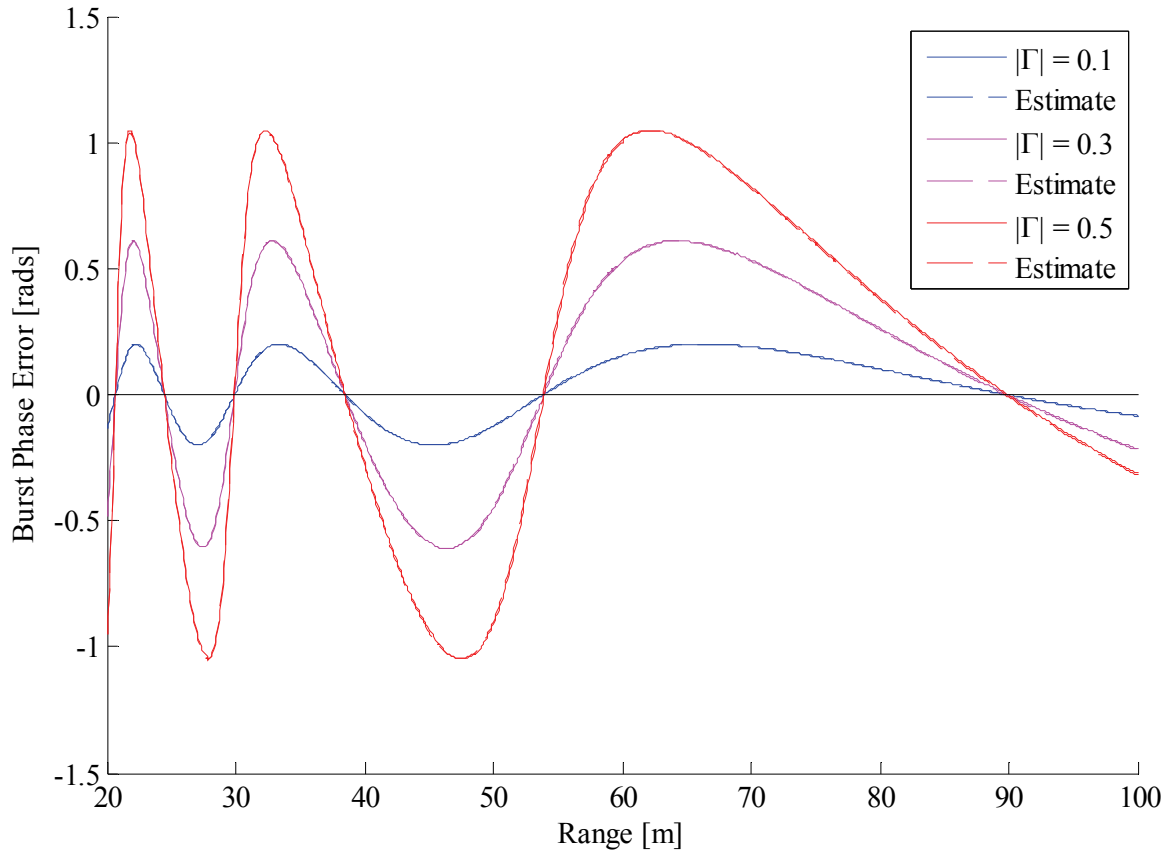


Figure 4.10 Comparison of theoretical and simulated burst phase errors due to specular multipath interference.

The second set of results, presented in Figure 4.11, illustrates the change in multipath phase error at higher radial velocities. At higher velocities the second multipath phase term, $\Phi_{\Delta mp}$, becomes more prominent. Excellent correlation can again be seen between the predicted theoretical phase error ($\Phi_{mp} + \Phi_{\Delta mp} N_D/2$ from (4.17)) and the simulated phase error, except for very sharp changes Φ_{mp} . This is where the assumption that the change in multipath phase error between consecutive sweeps remains fairly constant, no longer holds.

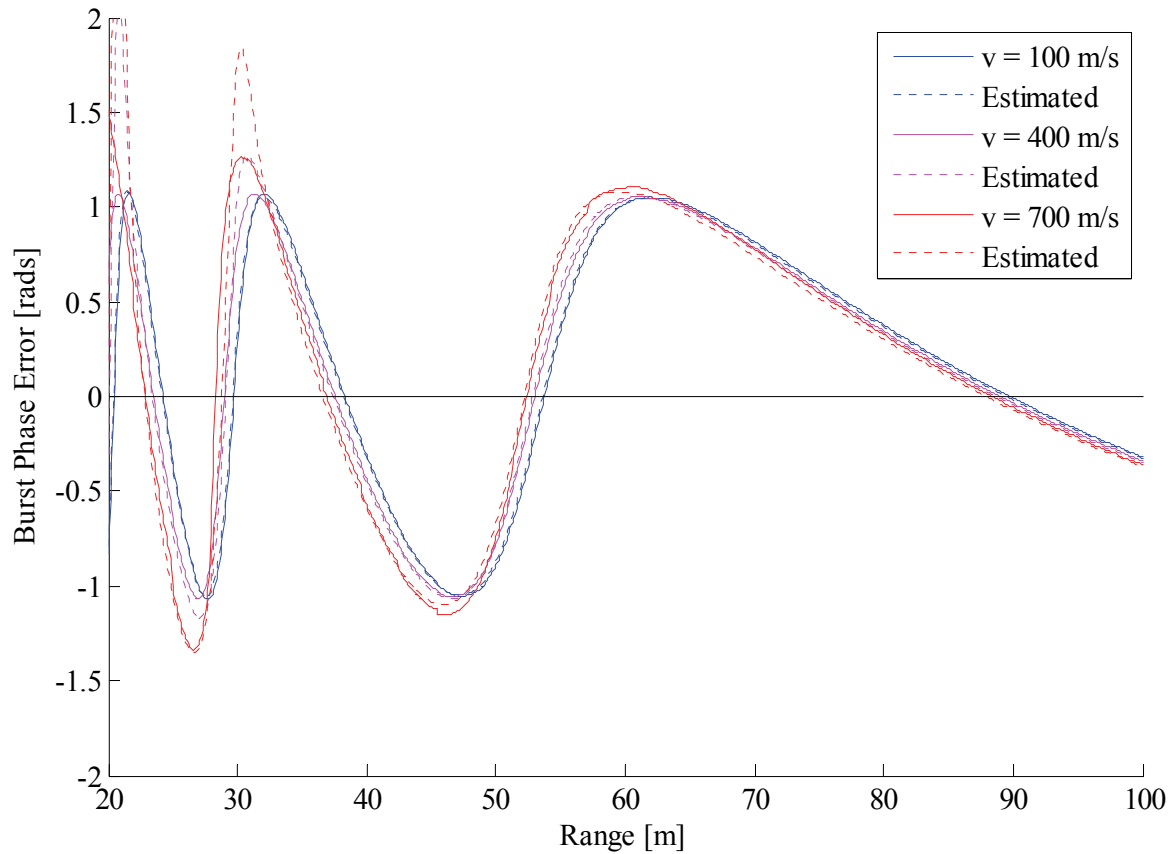


Figure 4.11 Comparison of theoretical and simulated burst phase errors due to specular multipath interference.

4.5 Conclusion

This chapter constructed a new multipath interference model for Dual-Frequency Phase-Comparison FMCW applications. A flat ground plane was assumed as the primary reflective surface; from here expressions were derived for the changes in phase and amplitude of an FMCW base-band signal due to multipath interference. These mathematical expressions were combined with the signal processing derivations in Chapter 3 to produce the final model. Extensive simulations were also conducted to prove the validity and establish the limits of the new model. Chapter 5 will look at phase interferometry and angle extraction, which should provide a benchmark for determining the severity of any multipath phase errors.

Chapter 5: Phase Interferometry

Chapters 3 and 4 developed a new model for specular multipath interference in FMCW systems. This chapter will take a closer look at Angle-of-Arrival (AoA) determination, as well as calculation of elevation and azimuth angles, which is necessary to quantify the error introduced by multipath reflections.

5.1 Basic Angle-of-Arrival Extraction

Figure 5.1 shows two receivers, separated by a distance d , as well as an incoming signal. Assuming the origin of the signal is far enough away, the incoming wave fronts can be approximated as planar (instead of spherical), which means that lines A and B can be drawn parallel to each other. Signal path B is slightly longer than signal path A ; this causes a difference in phase between the two receive signals. The phase difference, $\Delta\Phi$, is related to the incidence angle, γ , and can therefore be used to determine AoA.

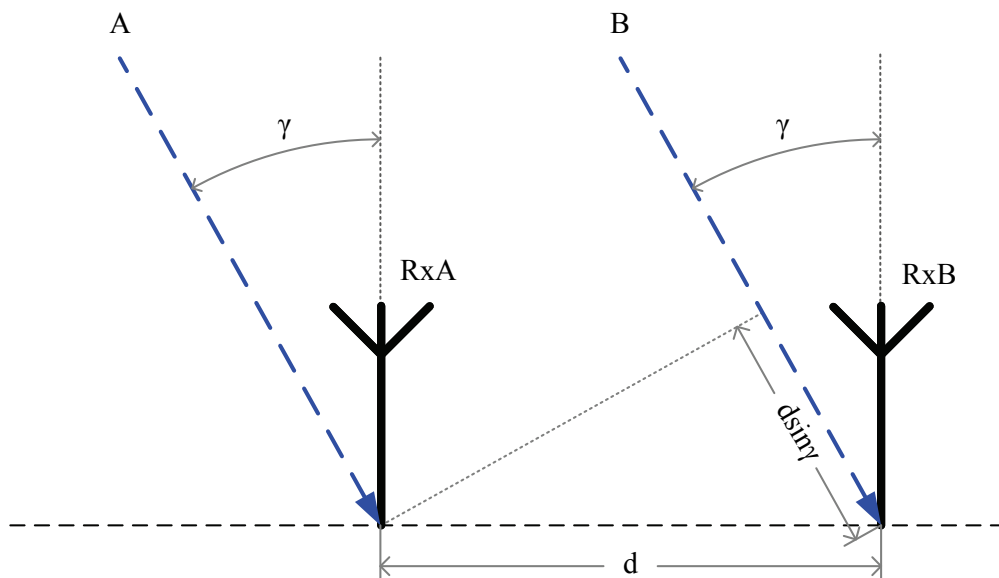


Figure 5.1 The Angle-of-Arrival (γ) determines the difference in path length ($d \sin \gamma$) that a signal travels to two receivers separated by a distance of d .

Recall from Table 3.1 that the measured burst phase (without any interference or error components) for receiver A can be expressed as:

$$\Phi_{A0} = 2\pi f_0 t_{d0} \quad (5.1)$$

Receiver B 's signal will be delayed by a short time period:

$$\Phi_{B0} = 2\pi f_0 (t_{d0} - \Delta t) \quad (5.2)$$

$$\begin{aligned} \Delta t &= \frac{\Delta d}{c} \\ &= \frac{d \sin \gamma}{c} \end{aligned}$$

The phase difference will then be:

$$\begin{aligned} \Delta \Phi &= \Phi_{A0} - \Phi_{B0} \\ &= 2\pi f_0 \frac{\Delta d}{c} \\ &= \frac{2\pi d \sin \gamma}{\lambda_0} \end{aligned} \quad (5.3)$$

The relationship in (5.3) can be used to calculate AoA when $\Delta \Phi$ is known:

$$\gamma = \text{asin} \left(\frac{\Delta \Phi \lambda_0}{2\pi d} \right) \quad (5.4)$$

5.2 Translating AoA into Elevation and Azimuth Angles

Figure 5.2 illustrates the coordinate system used in this text. Elevation (θ) is defined as the angle that the line (RT) from the target to the origin ($x = 0, y = 0, z = 0$) makes with the horizontal plane (xy). Azimuth (φ) is defined as the angle that the vertical plane containing line RT makes with the y -axis. The radar is at the origin, and the range is the distance from radar to target, which would be the length of line RT .

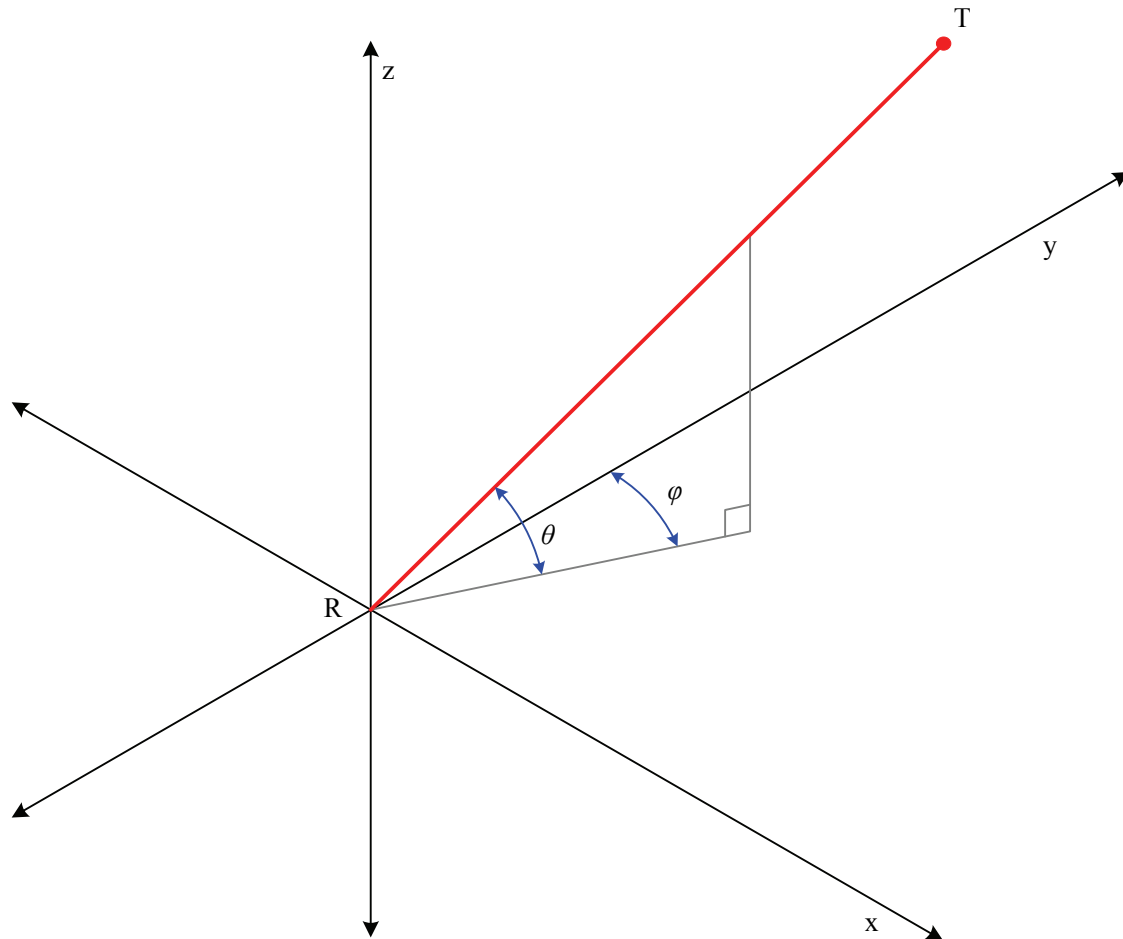


Figure 5.2 Elevation and azimuth angles relative to a global coordinate system.

There are several receive antenna configurations that could potentially be used to obtain elevation and azimuth angles. They will be discussed in the following sub-sections.

5.2.1 Equilateral Triangle Antenna Constellation

The APS radar device uses an equilateral triangle configuration, shown in Figure 5.3. Three receive antennas, all operating at 9.1 and 10.1 GHz, are placed at equal distances from each other with a transmit antenna placed in the centre. This allows for a compact and efficient system design.

Each pair of two receive antennas creates an axis around which an AoA can be measured. These axes do not relate directly to elevation and azimuth. Consequently, additional calculations are required. Three axes, each with an AoA and a range measurement, produce three toroids. The intersection of these toroids marks the target location. This can become a very complex problem to solve, especially if range and angle resolution are taken into account. A two-dimensional approximation is shown in Figure 5.4, where the toroids are projected onto the xz -plane and treated as lines.

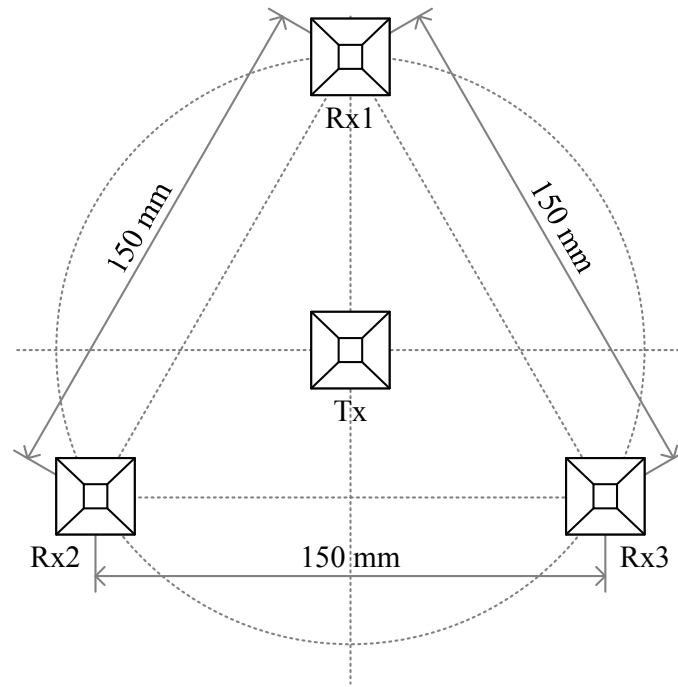


Figure 5.3 Equilateral triangle antenna configuration (as seen from the back).

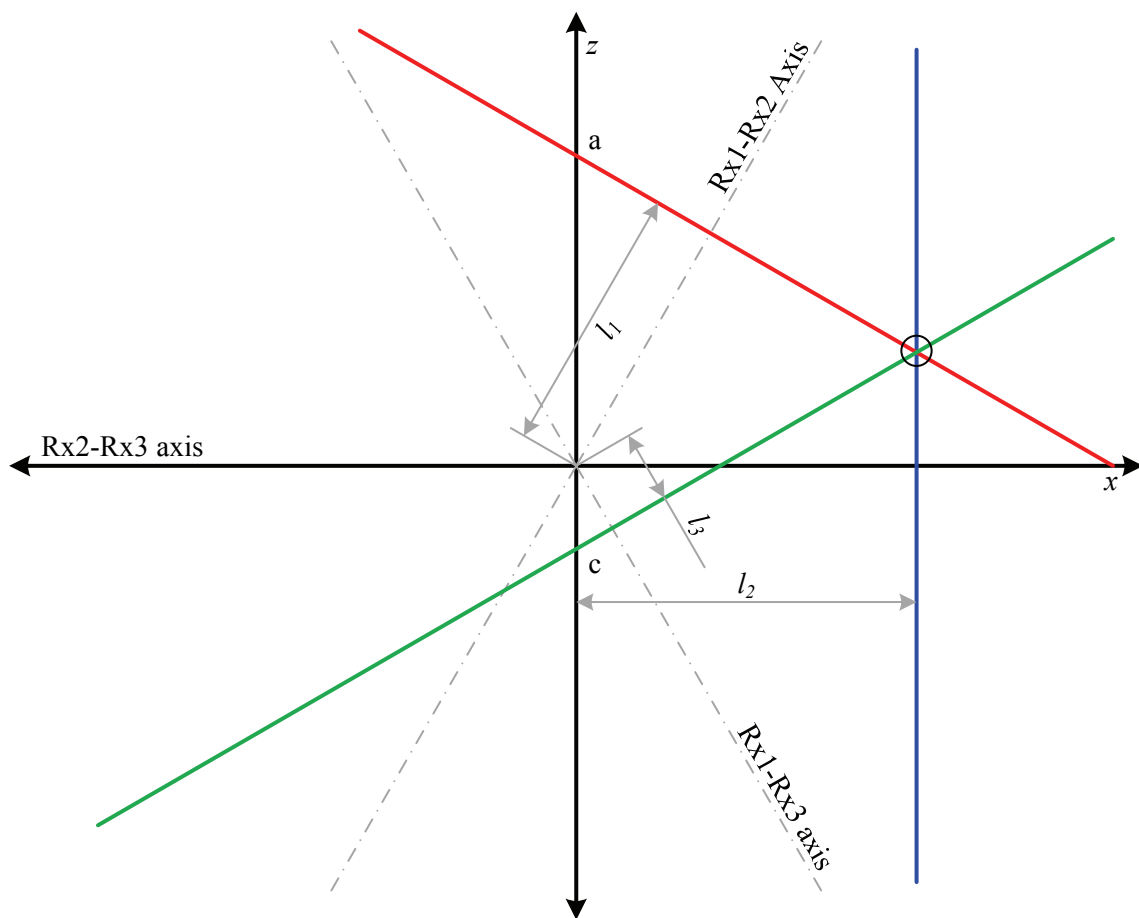


Figure 5.4 Two-dimensional approximation to determine elevation and azimuth angles (equilateral triangle).

The three projected lines should intersect at a point (x_l, z_l) . Together with range, x_l and z_l can be used to calculate target position in three-dimensional space. The three phase differences are defined as:

$$\Delta\Phi_1 = \Phi_{Rx1} - \Phi_{Rx3} \quad (5.5)$$

$$\Delta\Phi_2 = \Phi_{Rx2} - \Phi_{Rx3}$$

$$\Delta\Phi_3 = \Phi_{Rx1} - \Phi_{Rx2}$$

which can be used to calculate three AoAs:

$$\gamma_1 = \text{asin}\left(\frac{\Delta\Phi_1 \lambda_0}{2\pi d}\right) \quad (5.6)$$

$$\gamma_2 = \text{asin}\left(\frac{\Delta\Phi_2 \lambda_0}{2\pi d}\right)$$

$$\gamma_3 = \text{asin}\left(\frac{\Delta\Phi_3 \lambda_0}{2\pi d}\right)$$

Referring to Figure 5.4, lengths l_1 , l_2 and l_3 will be:

$$l_1 = r \sin \gamma_1 \quad (5.7)$$

$$l_2 = r \sin \gamma_2$$

$$l_3 = r \sin \gamma_3$$

Lines A and C will intersect the z -axis at:

$$z_a = \frac{2l_1}{\sqrt{3}} \quad (5.8)$$

$$z_c = \frac{-2l_3}{\sqrt{3}}$$

The three-dimensional intersection point can now be expressed as:

$$x_1 = l_2 \quad (5.9)$$

$$z_1 = \frac{z_a + z_c}{2}$$

$$y_1 = \sqrt{R^2 - x_1^2 - z_1^2}$$

where R is the range from radar to target.

Elevation and azimuth will be:

$$\theta = \arcsin\left(\frac{z_1}{R}\right) \quad (5.10)$$

$$\varphi = \arctan\left(\frac{x_1}{y_1}\right)$$

5.2.2 Right-Angled Triangle Antenna Constellation

A right-angled configuration, illustrated in Figure 5.5, was used extensively during the early stages of this study while investigating multipath effects. The vertical Rx1-Rx2 axis allows for direct translation from AoA to elevation angle.

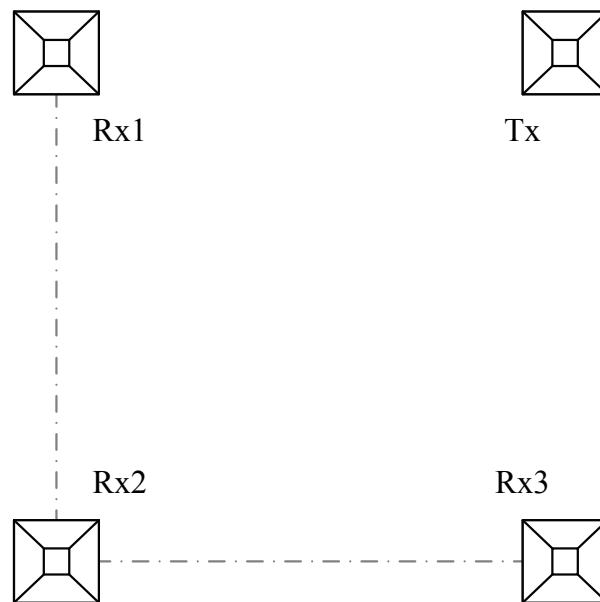


Figure 5.5 Right-angle antenna configuration (as seen from the back).

Figure 5.6 illustrates the geometry when solving for elevation and azimuth in a right-angled configuration. Elevation is given by:

$$\theta = \text{asin}\left(\frac{\Delta\Phi_1\lambda_0}{2\pi d}\right) \quad (5.11)$$

with

$$\Delta\Phi_1 = \Phi_{Rx1} - \Phi_{Rx2}$$

Azimuth is related to the geometry as follows:

$$\sin \varphi = \frac{x}{r'} \quad (5.12)$$

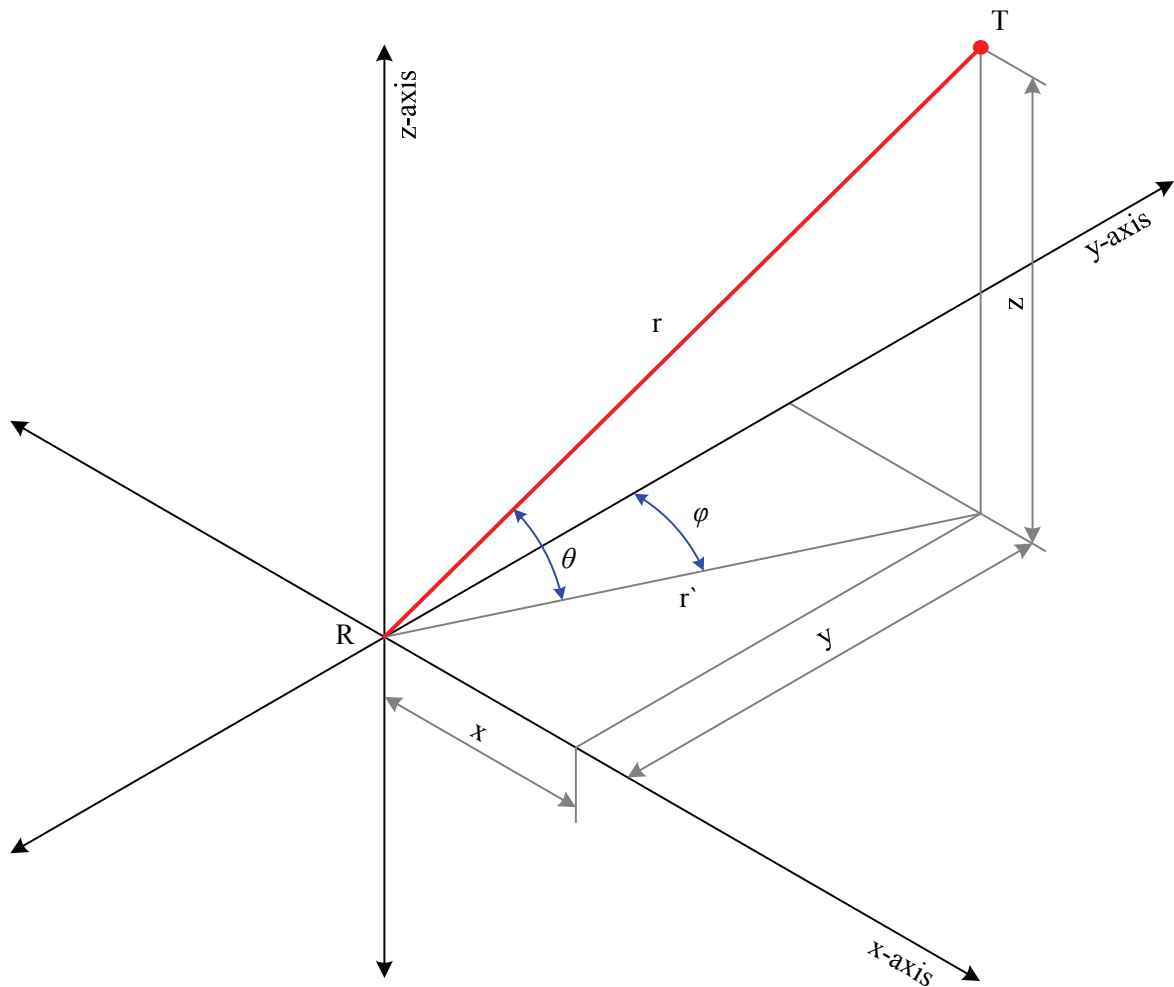


Figure 5.6 Elevation and azimuth angle geometry for the right-angled configuration.

The second phase difference (between $Rx2$ and $Rx3$) can be used to calculate x , while elevation can be used to obtain r' :

$$x = r \cos \gamma \quad (5.13)$$

$$r' = r \cos \theta$$

$$\gamma = \text{asin} \left(\frac{\Delta\Phi_2 \lambda_0}{2\pi d} \right)$$

$$\Delta\Phi_2 = \Phi_{Rx3} - \Phi_{Rx2}$$

$$\Rightarrow \varphi = \text{asin} \left(\frac{\cos \gamma}{\cos \theta} \right)$$

5.2.3 Two-by-Three Matrix Antenna Constellation

The six-antenna configuration, shown in Figure 5.7, was used during a proof-of-concept demonstration [54]. It is included here because these measurements will be presented in a subsequent chapter. Each antenna is used for a single operating frequency only, which necessitates the use of six receive and two transmit antennas. Angle extraction remains the same as in the equilateral triangle configuration.

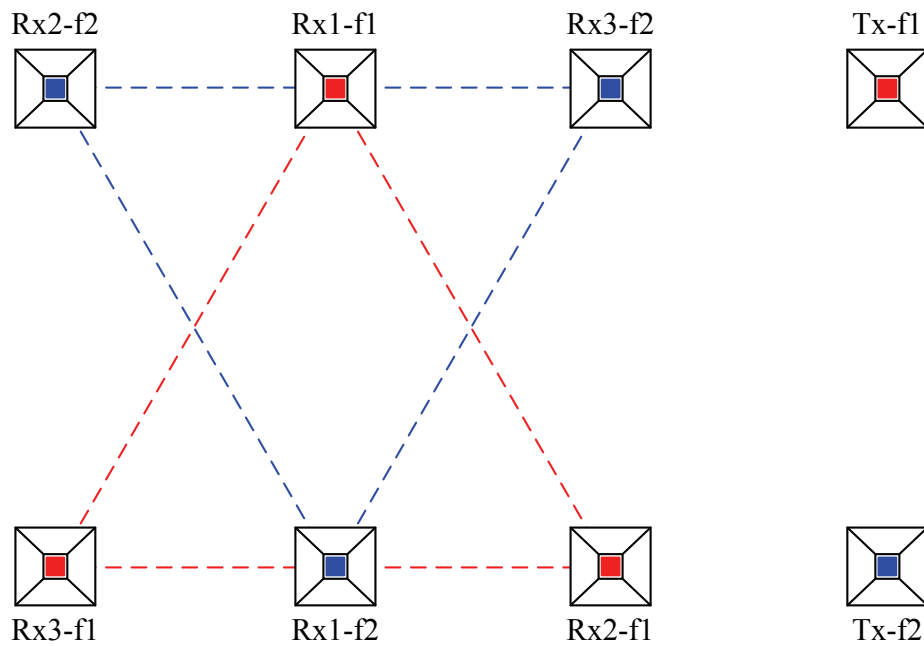


Figure 5.7 Two-by-three matrix antenna constellation (as seen from the back).

5.3 Receiver Spacing and AoA Ambiguities

Section 5.1 showed how the phase difference between two closely spaced receivers was related to the incoming signal's incidence angle:

$$\Delta\Phi = \frac{2\pi d \sin \gamma}{\lambda_0} \quad (5.14)$$

Aside from incidence angle, operating frequency and receiver spacing also determine phase difference. For a given wavelength (or operating frequency), there is a maximum receiver spacing (d) where unambiguous angle extraction is still possible. Assuming the incidence angle (γ) can range from -90° to $+90^\circ$:

$$\begin{aligned} -\frac{\pi}{2} &\leq \gamma \leq \frac{\pi}{2} \\ \Rightarrow -2\pi \frac{d}{\lambda_0} &\leq \Delta\Phi \leq 2\pi \frac{d}{\lambda_0} \end{aligned} \quad (5.15)$$

This implies that a maximum receiver spacing of half a wavelength (approximately 15 mm at 10 GHz) is required for unambiguous AoA determination. The APS radar sensor was designed with a receiver spacing ten times wider, approximately five wavelengths. An additional mechanism is needed to resolve the angle ambiguity, which will be discussed in the following sub-section.

5.4 Dual-frequency Angle Extraction

The AoA ambiguity mentioned in the previous sub-section can be resolved by incorporating a second operating frequency. Burst phase measurements from two operating frequencies (and a single receive antenna) can be used to create a third artificial operating frequency. Recall the ideal burst phase expression from (5.1) for operating frequency f_l :

$$\Phi_{A1} = 2\pi f_1 t_{d0} \quad (5.16)$$

A second burst phase measurement at f_2 for the same receive antenna will be:

$$\Phi_{A2} = 2\pi f_2 t_{d0} \quad (5.17)$$

Subtracting Φ_{A2} from Φ_{A1} yields:

$$\begin{aligned}\Phi_{A3} &= 2\pi f_1 t_{d0} - 2\pi f_2 t_{d0} \\ &= 2\pi f_3 t_{d0}\end{aligned}\tag{5.18}$$

Using APS as an example:

$$\begin{aligned}f_3 &= f_1 - f_2 \\ &= 10.1 \text{ GHz} - 9.1 \text{ GHz} \\ &= 1 \text{ GHz}\end{aligned}$$

A third artificial operating frequency of 1GHz was created, which can be used to resolve the angle ambiguity at f_1 and f_2 (also called coarse angle estimation). At 1 GHz, the receive antenna spacing of 150 mm is approximately equivalent to half a wavelength.

5.5 Multipath Effect

This section will investigate the effect of multipath on extracted angles. Chapter 4 developed a mathematical model that describes the change in measured burst phase due to specular multipath interference. Errors in burst phase will lead to errors in extracted elevation and azimuth angles, but it is the error in coarse angle that is of greatest practical concern. If the phase error is large enough, it could lead to incorrect ambiguities being resolved.

Consider the case where the receive antenna spacing is 5λ . The AoA is given by:

$$\begin{aligned}\sin \gamma &= \frac{\Delta\Phi\lambda_0}{2\pi d} & \left[-\frac{\pi}{2} < \gamma < \frac{\pi}{2}\right] \\ &= \frac{\Delta\Phi\lambda_0}{2\pi 5\lambda_0}\end{aligned}\tag{5.19}$$

There are ten possible angles⁴ for γ , which correspond to ten possible phase differences:

⁴ In the case where $\Delta\Phi = 0$, there will be nine possible angles, since $\pm\pi/2$ is excluded.

$$\Delta\Phi_{possible} = \Delta\Phi \pm 2\pi n \quad [n = 0, 1, 2, 3, 4, 5] \quad (5.20)$$

Figure 5.8 shows all possible angles (γ) for a burst phase difference measurement ($\Delta\Phi$) of 0. It can clearly be seen that a coarse angle estimation error as small as approximately 0.1 radians (6°) is enough to result in an incorrect ambiguity being chosen.

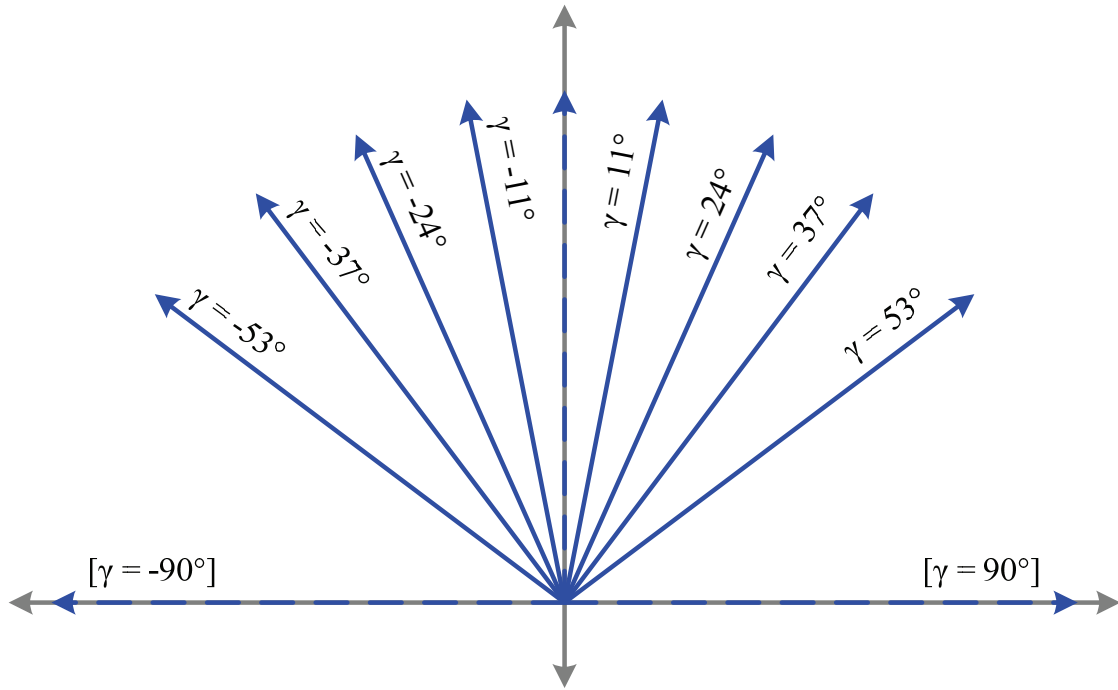
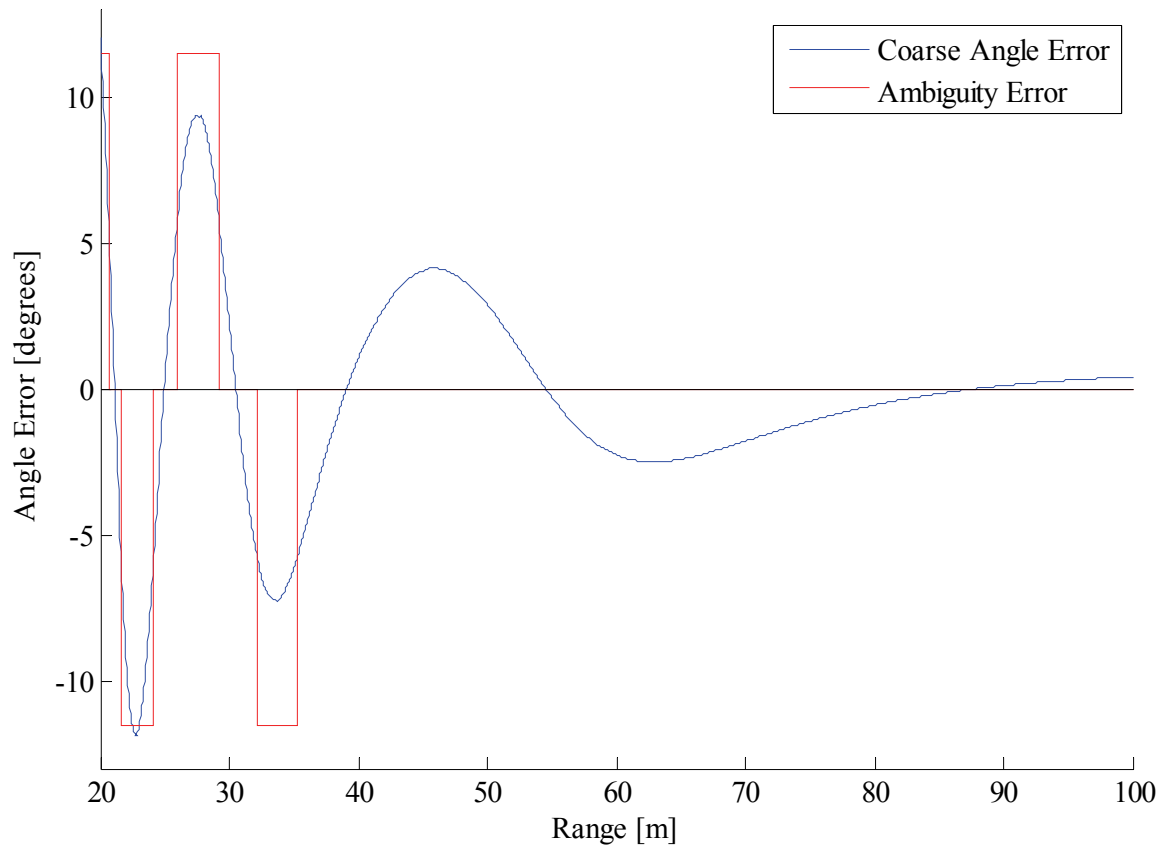
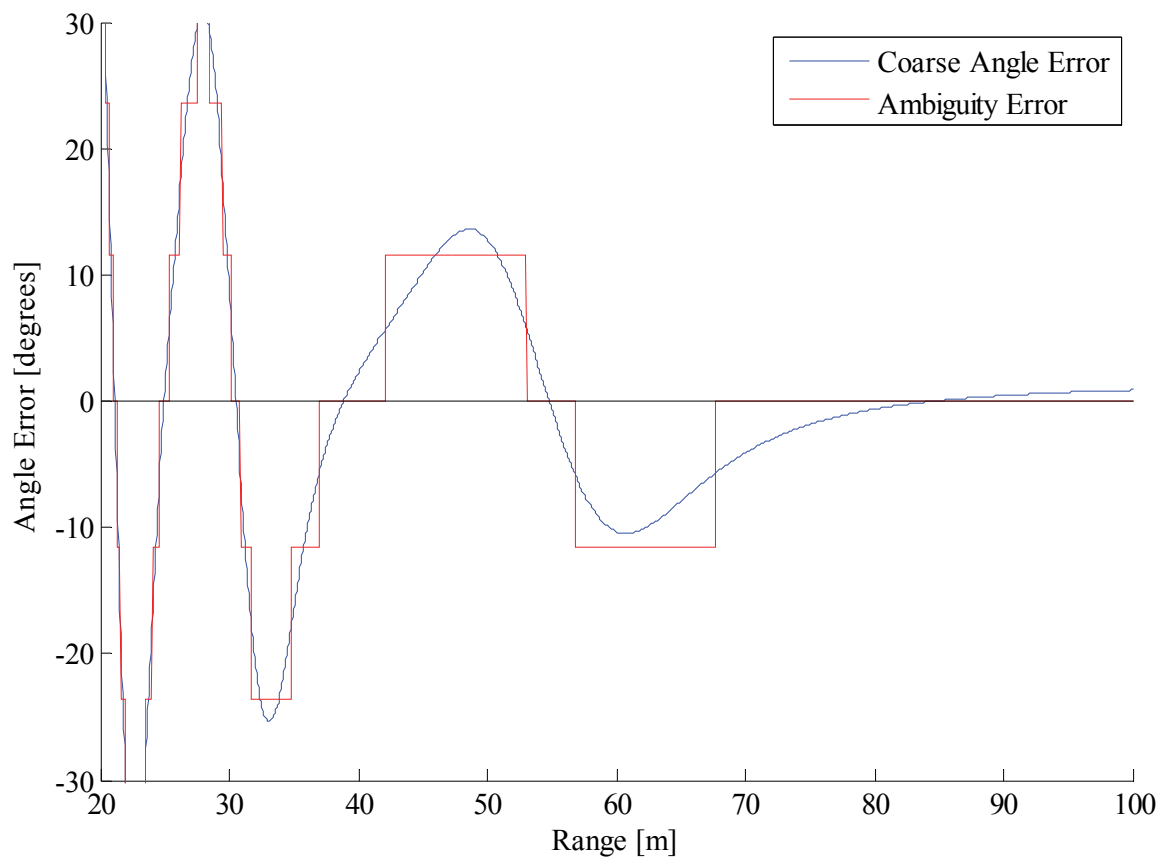


Figure 5.8 Ambiguous angles for a phase difference measurement of 0.

Figure 5.9 (a - c) shows the simulated coarse angle error and the resulting ambiguity angle error (error due to incorrect ambiguity being chosen). The first graph (Figure 5.9 a) illustrates angle errors under mild multipath conditions ($|I| = 0.1$). While the coarse angle error is fairly small, there are some instances where an incorrect ambiguity is chosen. The second and third graphs are for moderate ($|I| = 0.3$) and severe ($|I| = 0.5$) multipath conditions. Coarse angle errors become very large under these circumstances, which is why a mitigation method is essential. Mitigation methods will be discussed in the next chapter.



(a)



(b)

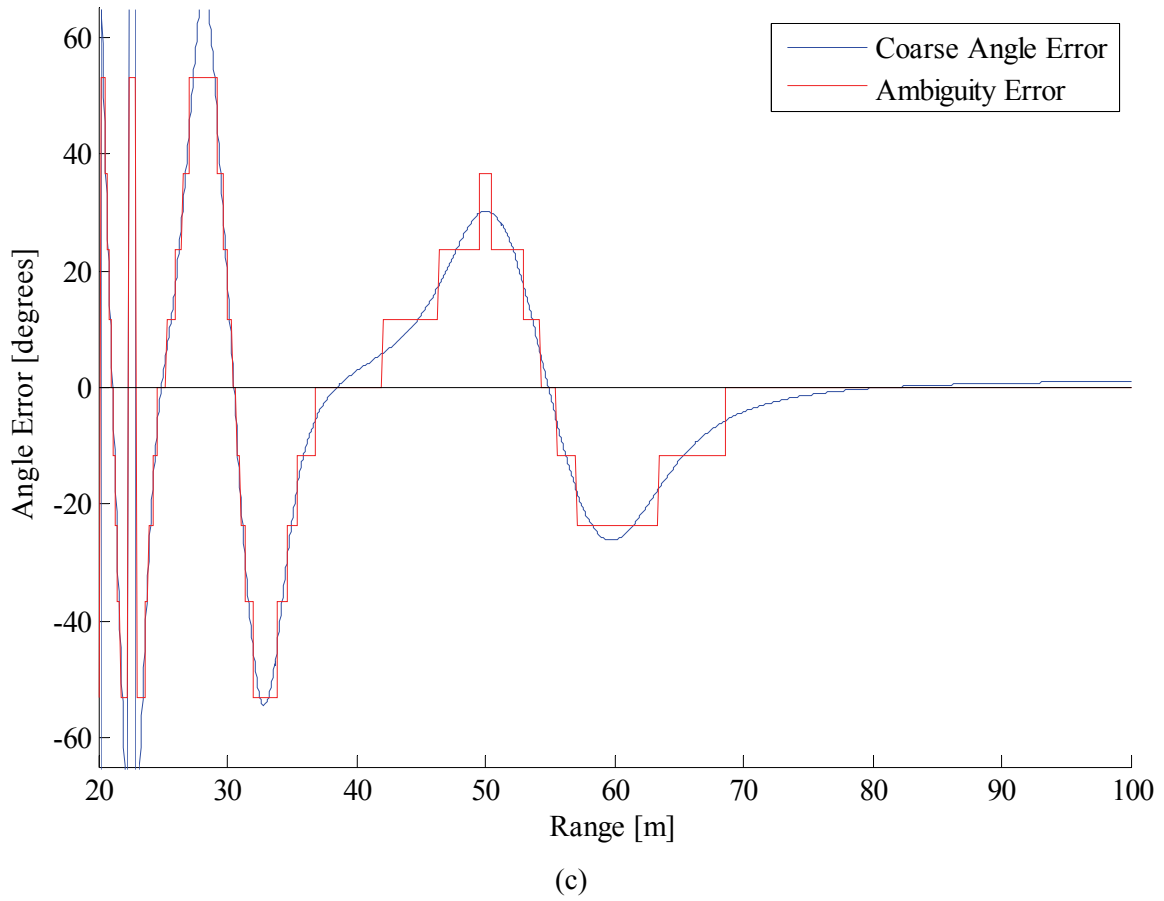


Figure 5.9 Coarse angle error and the resulting ambiguity angle error for (a) $|I| = 0.1$, (b) $|I| = 0.3$ and (c) $|I| = 0.5$.

5.6 Conclusion

This chapter discussed some of the algorithms and antenna configurations that can be utilised to calculate elevation and azimuth angles in phase-comparison systems. This allowed for a qualitative evaluation of multipath phase error, which will be needed in Chapter 6 when possible mitigation methods are proposed.

Chapter 6: Mitigation Methods

Previous chapters investigated the effects of specular multipath interference on the measured burst phase and the resulting errors in angle estimation. It was shown that, even under moderate multipath conditions, serious coarse angle errors can occur. This chapter will investigate three mitigation techniques that can be implemented to cope with multipath interference.

6.1 Method 1: Single Channel Phase Unwrapping

The ideal burst phase, Φ_0 , is a function of the distance between the target and the radar. As this distance changes (due to target movement), the burst phase will change, continually wrapping itself around the $(-\pi, \pi]$ range. This mitigation method will attempt to unwrap the measured burst phase and then look for any periodic variations caused by multipath.

6.1.1 Algorithm Description

Recall the expression for measured burst phase from (3.23):

$$\begin{aligned}
 \Phi_{burst} &= \Phi_0 - \Phi_{error} + \Phi_{mp} + f_{IF} \frac{\pi N_R}{f_s} + f_{error} \frac{\pi N_R}{f_s} - \pi k \\
 &\quad + \theta_\Delta \frac{N_D}{2} + \Phi_{\Delta mp} \frac{N_D}{2} + \pi f_\Delta \frac{N_R N_D}{2 f_s} - \pi b \\
 &= (\Phi_0 - \Phi_{error}) + q\pi + a\pi + (\Phi_{mp} + \Phi_{\Delta mp} \frac{1}{2} N_D)
 \end{aligned} \tag{6.1}$$

There are four main components: $(\Phi_0 - \Phi_{error})$, q (which changes as the target moves from range-bin to range-bin), a (which changes as the target moves from Doppler-bin to Doppler-bin) and the multipath phase error.

- Φ_0 and Φ_{error} can be estimated by using (3.11a) and (3.11a).
- q can be estimated by calculating the time spent in each range-bin.
- a can be estimated by calculating the time spent in each Doppler-bin.

The estimates for $(\Phi_0 - \Phi_{error})$, $q\pi$ and $a\pi$ are subtracted from Φ_{burst} to produce an intermediary phase:

$$\Phi_{temp} = \Phi_{burst} - \Phi_{0est} - q\pi_{est} - a\pi_{est}$$

$$\approx \Phi_{remainder} + (\Phi_{mp} + \Phi_{\Delta mp} \frac{1}{2} N_D) \quad (6.2)$$

The intermediary phase is then unwrapped and compared with the range data. The graphs of the unwrapped phase and the range should be similar in shape. The last step is to remove the remaining non-multipath phase by subtracting an appropriately scaled version of the range graph. Figure 6.1 illustrates the process:

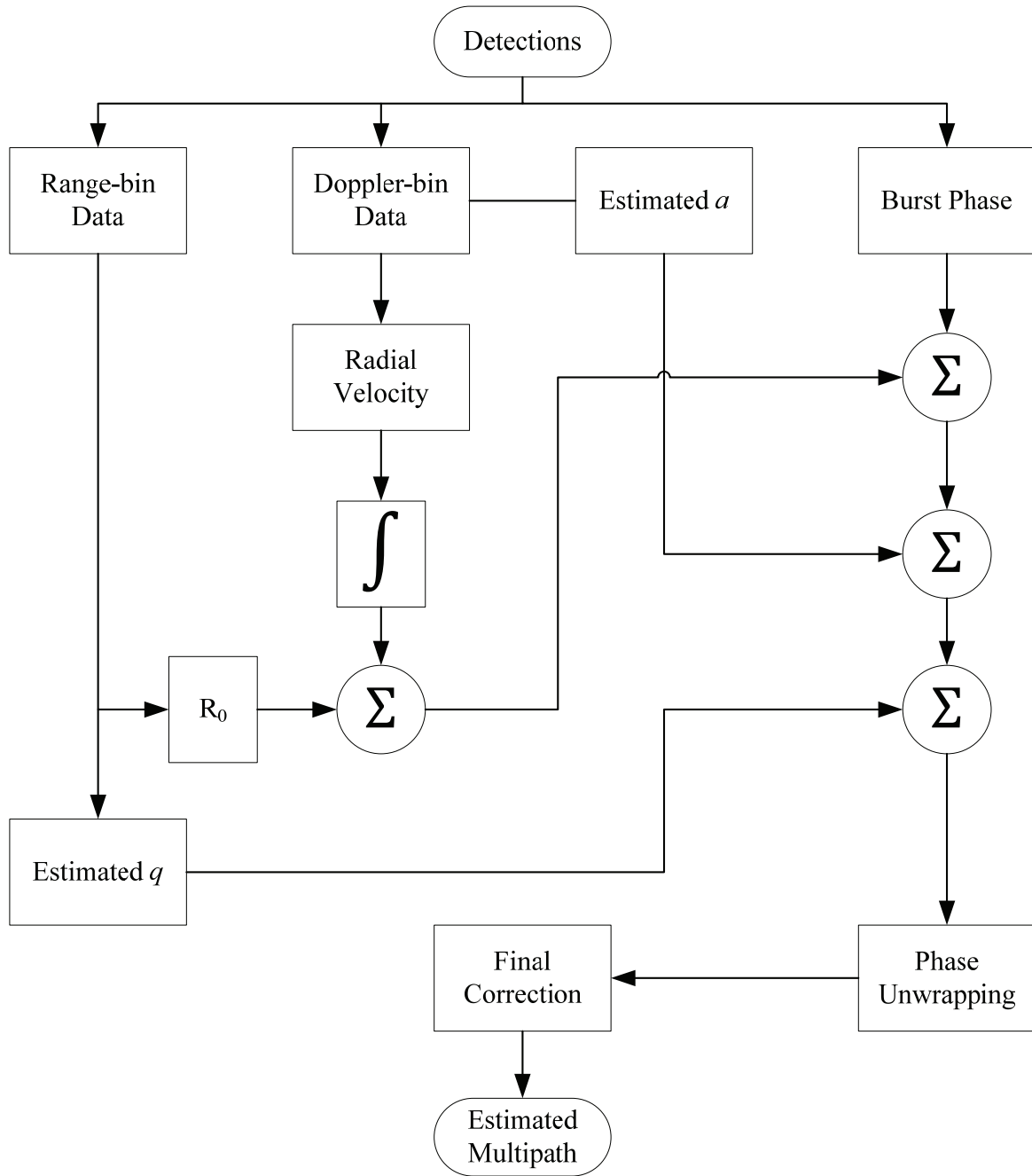


Figure 6.1 Single-channel phase unwrapping algorithm.

6.1.2 Simulation Example

This sub-section will illustrate the mitigation method step-by-step using a simulation example. Two receive antennas were placed directly above each other at heights of 1 m and 1.15 m respectively. The simulation parameters are listed in Table 6.1.

Table 6.1 Simulation parameters.

Parameter	Value	Notes
Target Velocity	-100 m/s	Velocity remained constant.
Initial Target Range	20 m	
Target Placement (Height, Offset)	(1 m, 0 m)	Target directly in front of radar.
Target Attitude (Azimuth, Elevation)	(0 rads, 0 rads)	Target moved directly towards radar.
SNR	20 dB	After range-Doppler processing.
Antenna Separation Distance	0.15 m	
Operating Frequencies (f_1, f_2)	(10.1 GHz, 9.1 GHz)	
Sample Rate, f_s	15.625 MHz	
Samples per Sweep, N_R	256	
Sweeps per Burst, N_D	256	
Sweep Duration, T_{rep}	20 μ s	
Sweep Rate, μ	3.125 THz/s	
Reflection Coefficient, $ I $	0.5	

The first step is to extract range-bin and Doppler-bin data. The Doppler-bin data is trivial to obtain in this case, as the target is maintaining a constant velocity. Substituting into (3.25) and solving for b yields:

$$\text{Doppler} - \text{bin}_{f_1} = 34$$

$$\text{Doppler} - \text{bin}_{f_2} = 31$$

The Doppler-bin data can also be measured (as it would be in a real-world scenario). Radial velocity is estimated as the average of the velocities obtained via Doppler-bin_{f1} and Doppler-bin_{f2} (from (3.25)):

$$v_{est} = \frac{1}{2} \left[\frac{cb_1}{2f_1 T_{rep} N_D} + \frac{cb_2}{2f_2 T_{rep} N_D} \right] \quad (6.3)$$

$$= 99.21 \text{ m/s}$$

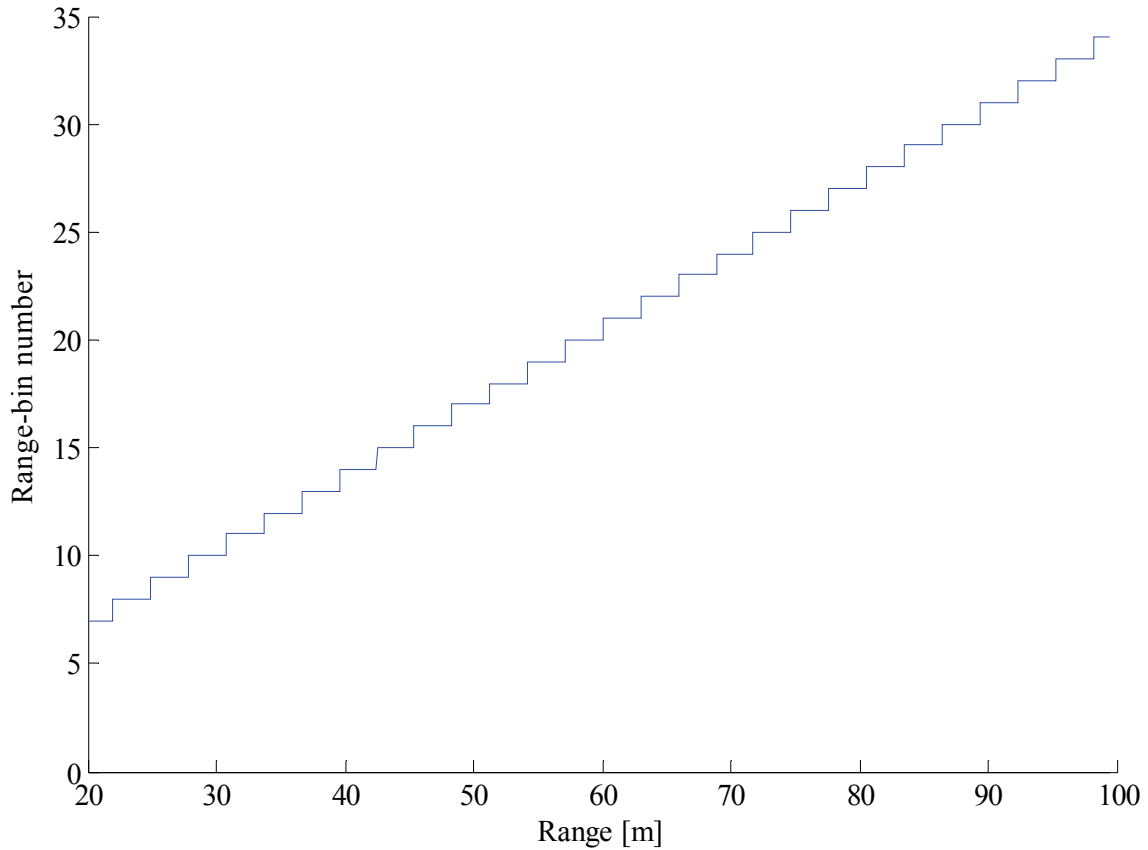


Figure 6.2 Range-bin number as a function of range.

The range-bin data is presented in Figure 6.2. From this it is possible to estimate the initial range (R_0) using (3.24):

$$R_0 = \frac{cf_s}{2\mu N_R} k \quad (6.4)$$

$$= 20.51 \text{ m}$$

R_0 is combined with velocity to estimate range (shown in Figure 6.3):

$$R_{est} = R_0 + \int_0^t v_{est} du \quad (6.5)$$

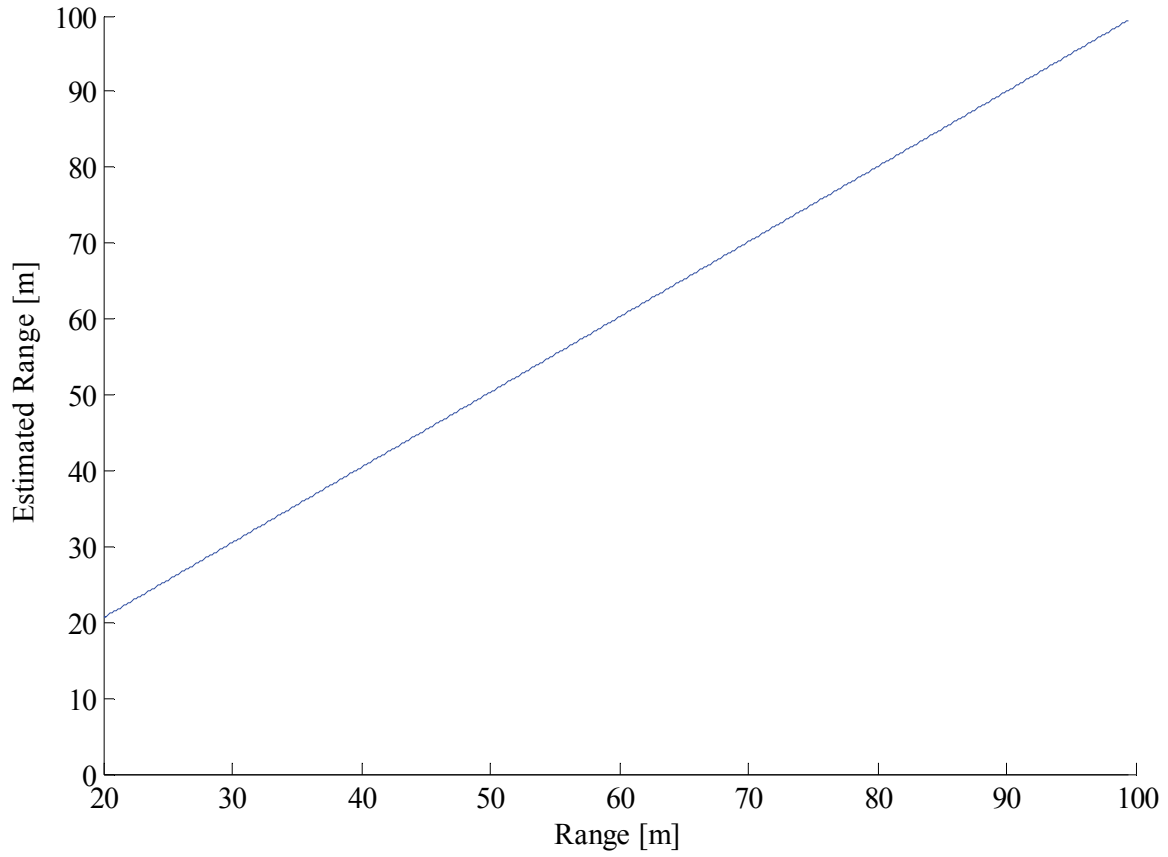
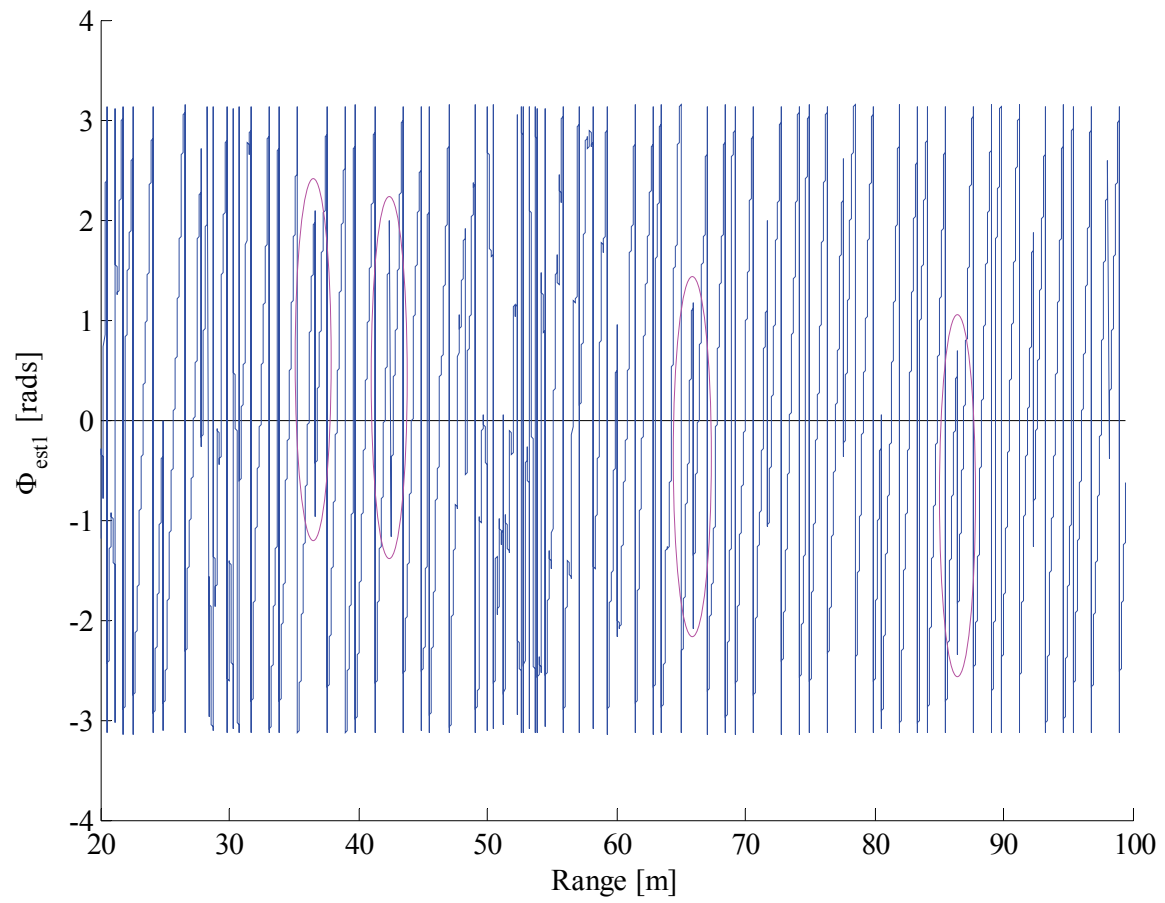


Figure 6.3 Estimated range as a function of range.

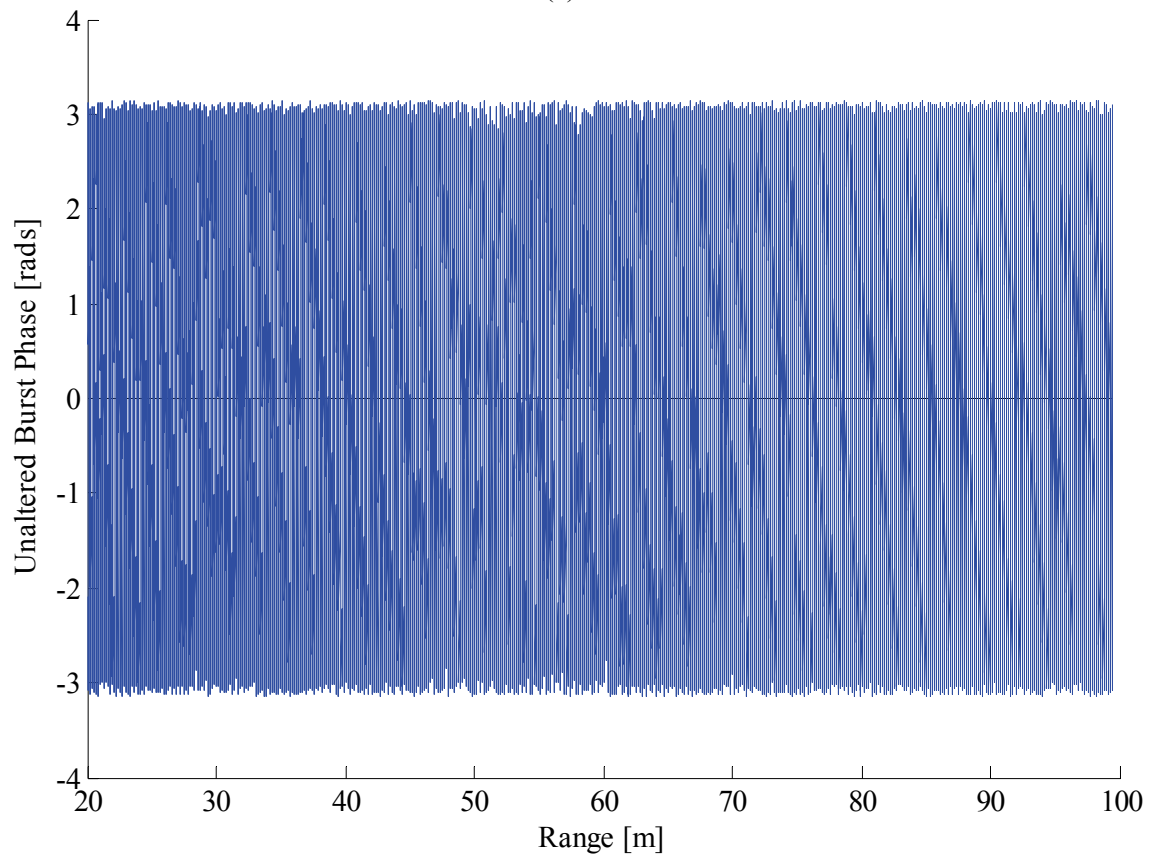
With R_{est} it is possible to obtain an estimate of $(\Phi_0 - \Phi_{error})$, which allows for the first part of the multipath estimation algorithm to be completed:

$$\begin{aligned} \Phi_0 - \Phi_{error} &= 2\pi f_0 \frac{2R}{c} - 2\pi\mu \left(\frac{1}{2} t_{d0}^2 + \frac{2v^2}{c^2} n^2 T_{rep}^2 \right) \\ &\approx 2\pi f_0 \frac{2R}{c} - 4\pi\mu \frac{R^2}{c^2} \\ \Rightarrow \Phi_{0est} &= 2\pi f_0 \frac{2R_{est}}{c} - 4\pi\mu \frac{R_{est}^2}{c^2} \end{aligned} \quad (6.6)$$

and:



(a)



(b)

Figure 6.4 Comparison of burst phase (a) after and (b) before compensation.

$$\begin{aligned}
\Phi_{est1} &= (\Phi_0 - \Phi_{error}) + q\pi + a\pi + \left(\Phi_{mp} + \Phi_{\Delta mp} \frac{1}{2} N_D\right) - \Phi_{0est} \\
&= \left(\Phi_{mp} + \Phi_{\Delta mp} \frac{1}{2} N_D\right) + q\pi + a\pi + \Phi_{Remainder}
\end{aligned} \tag{6.7}$$

Figure 6.4 (a and b) illustrates this, where the unaltered burst phase is compared with the phase after subtracting Φ_{0est} . The altered phase changes at a far slower rate, and it is now possible to see the transitions (circled in magenta) from one range-bin to the next range-bin.

The next step is to estimate q and a (from (6.1)). Recall from (3.14b) that the value of q changes from -0.5 to 0.5 as the target moves from one boundary of the range-bin to the other boundary. It should be possible to deduce an estimate for q from the range-bin data presented in Figure 6.2.

Since the simulated target is moving at a constant velocity, it is not necessary to estimate a (which will also remain constant), but a similar method as for q can be followed.

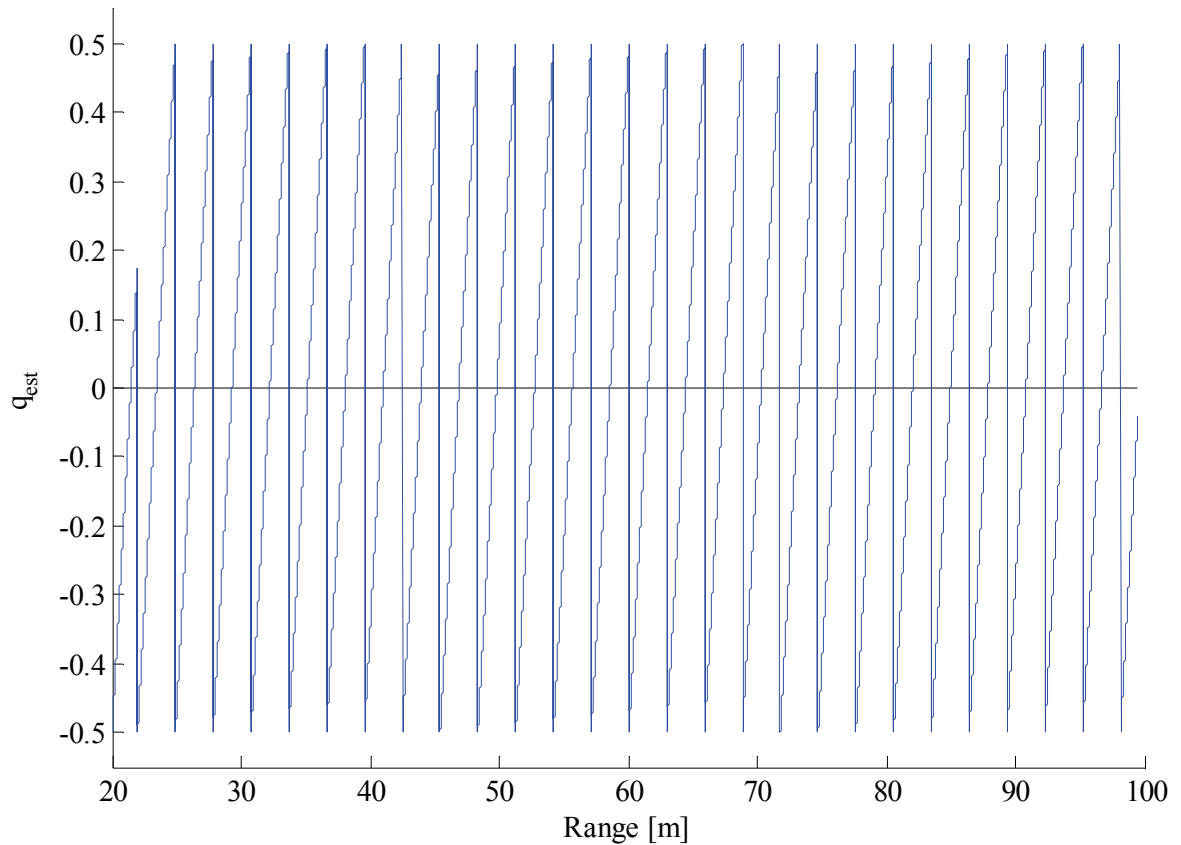


Figure 6.5 Estimated q as a function of range.

Figure 6.5 shows the estimated q for this simulation example, which was obtained by converting the step-function range-bin data into a corresponding saw-tooth function. The multipath estimate can be further refined by subtracting πq (and πa , if applicable):

$$\begin{aligned}\Phi_{est2} &= \Phi_{est1} - \pi q_{est} - \pi a_{est} \\ &= \left(\Phi_{mp} + \Phi_{\Delta mp} \frac{1}{2} N_D \right) + \Phi_{Remainder}\end{aligned}\quad (6.8)$$

This produces the graph in Figure 6.6. The phase discontinuities (where the target transitioned from one range-bin to the next) have been removed, but there is still a remaining non-multipath phase component. The remainder ($\Phi_{remainder}$) is due to the small difference between estimated and actual range.

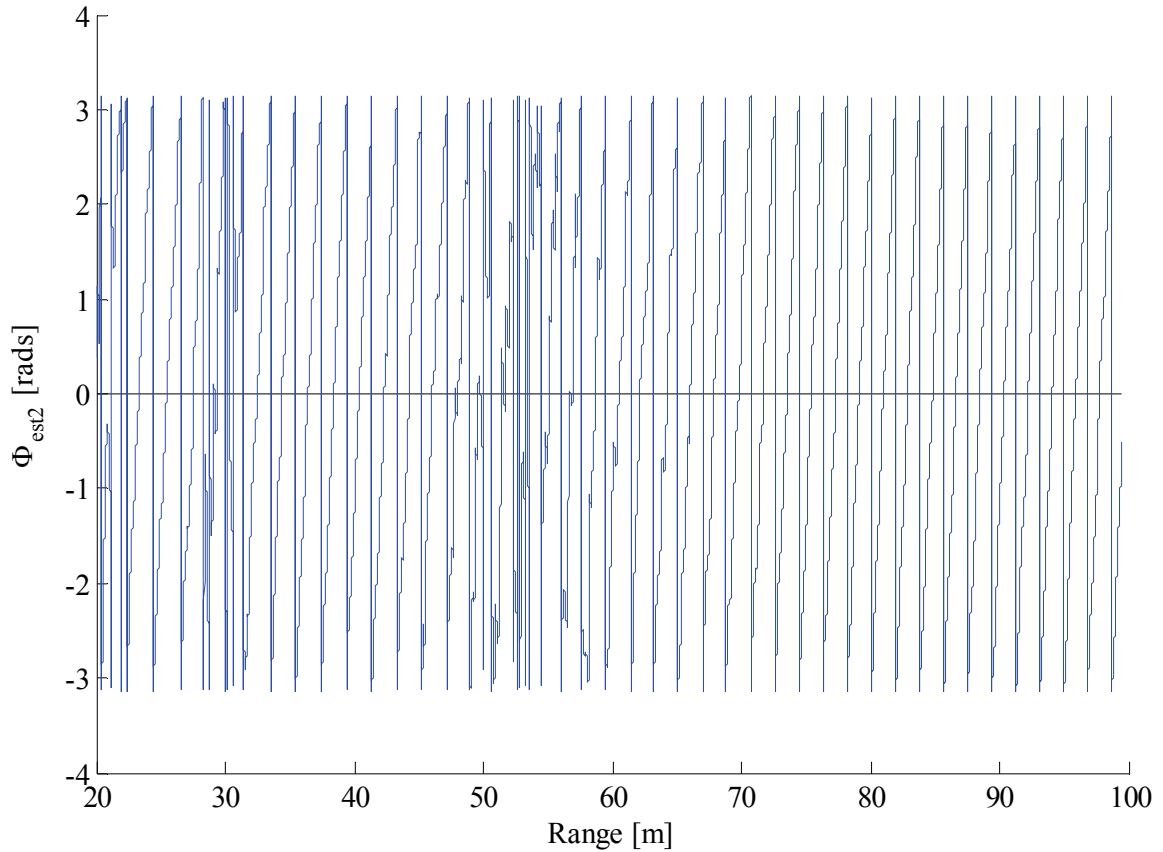


Figure 6.6 Compensated burst phase after subtracting πq .

Figure 6.7 compares a graph of Φ_{est2} after unwrapping with a scaled graph of estimated range. They are similar in shape, since the estimated range (and therefore Φ_{0est}) should be similar in shape to the

actual range. Subtracting an appropriately scaled version of the estimated range should therefore produce something very close to the desired multipath phase:

$$\begin{aligned}\Phi_{est3} &= \Phi_{est2} - K_1 R_{est} \\ &\approx \left(\Phi_{mp} + \Phi_{\Delta mp} \frac{1}{2} N_D \right) + K_{Const}\end{aligned}\quad (6.9)$$

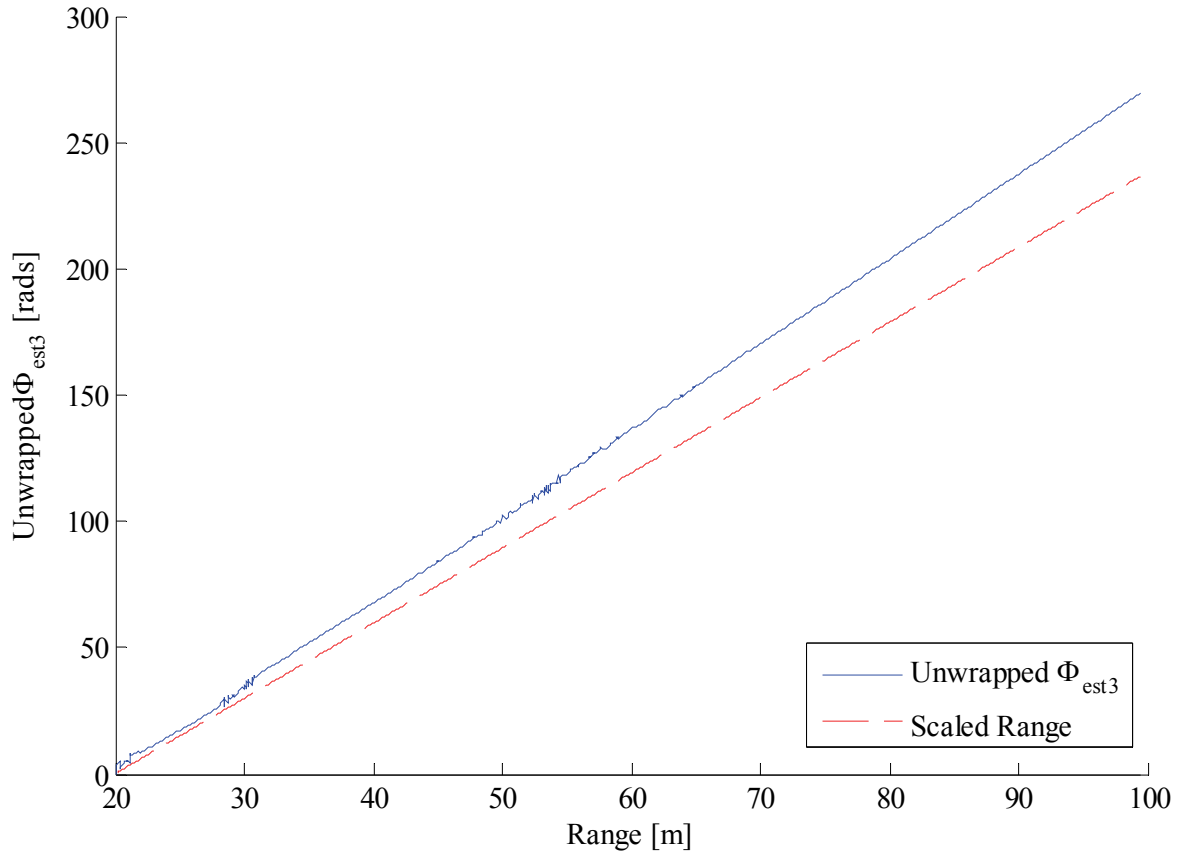


Figure 6.7 Unwrapped, compensated burst phase as a function of range.

The only remaining undesired component should be an approximately constant phase, K_{Const} . Recall from Figure 4.7 that the multipath phase error should have a zero mean (for the duration of one period), which implies that K_{Const} can be eliminated by subtracting an appropriate value:

$$\begin{aligned}Multipath_{est} &= \Phi_{est3} - \overline{\Phi_{est3}} \\ &\approx \left(\Phi_{mp} + \Phi_{\Delta mp} \frac{1}{2} N_D \right)\end{aligned}\quad (6.10)$$

A final estimate for the multipath phase error is compared to the actual multipath phase error in Figure 6.8, clearly showing very good agreement between the two.

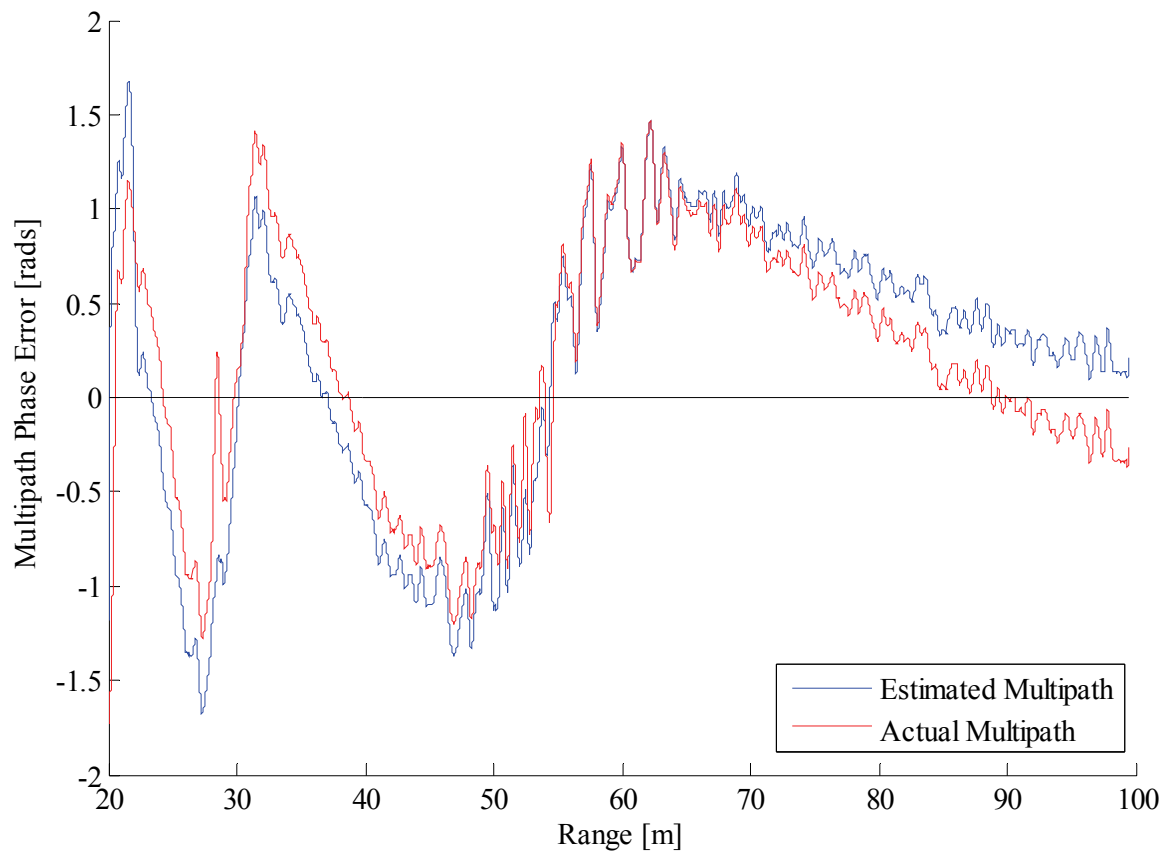


Figure 6.8 Final estimation of multipath phase error.

6.1.3 Measured Data Example

This sub-section will apply the phase unwrapping method to real-world measured data obtained from a Reutech Radar Systems demonstrator radar. During measurement, a rocket-propelled grenade (RPG) was launched from approximately 200 m away towards a target area 14 m to the right of the radar system. An eight-antenna configuration was used (six receive and two transmit antennas), similar to that shown in Figure 5.7.

The first step is extracting range-bin and Doppler-bin information, presented here in Figure 6.9 and Figure 6.10 respectively. Data from all six receivers are shown to illustrate the effects of noise (and other interfering signals). The Doppler-bin data can then be used to estimate radial velocity, shown in Figure 6.11, which can in turn be used to estimate range, shown in Figure 6.12. Estimates for q and a can also be computed, as illustrated in Figure 6.13.

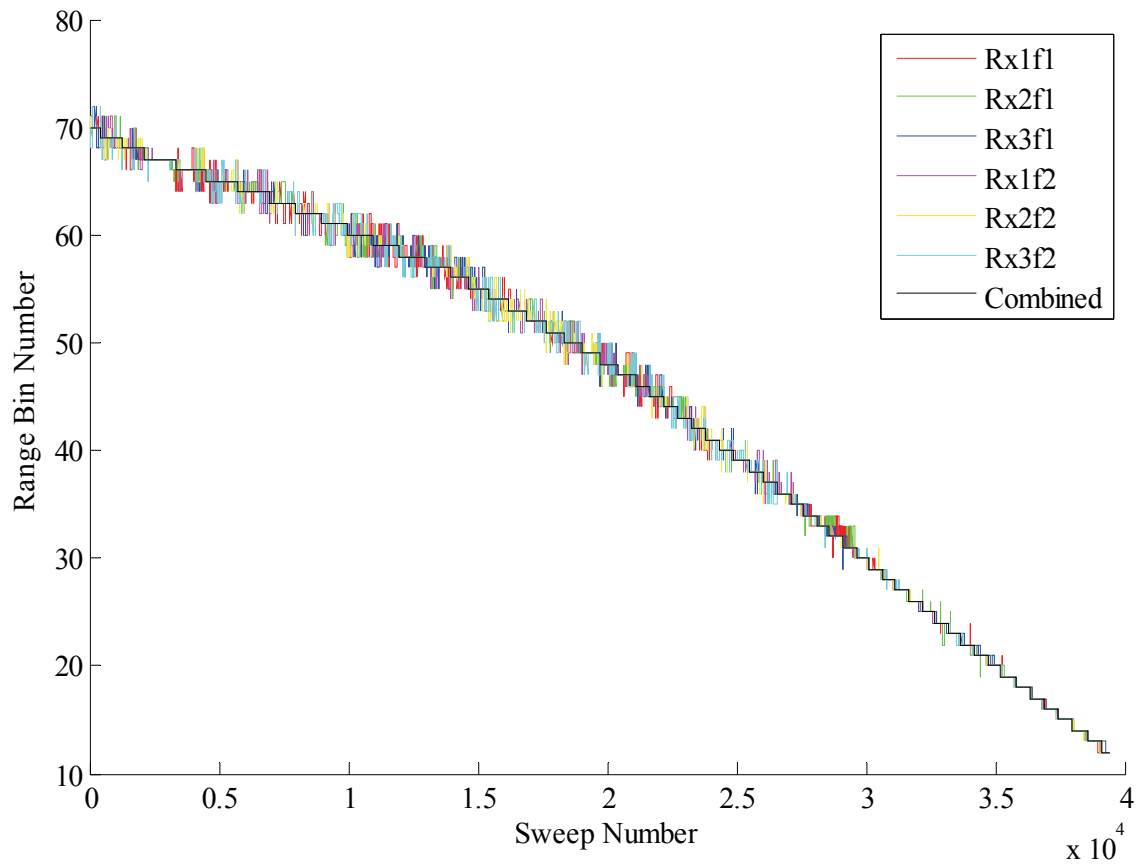


Figure 6.9 Detected range-bins for all channels.

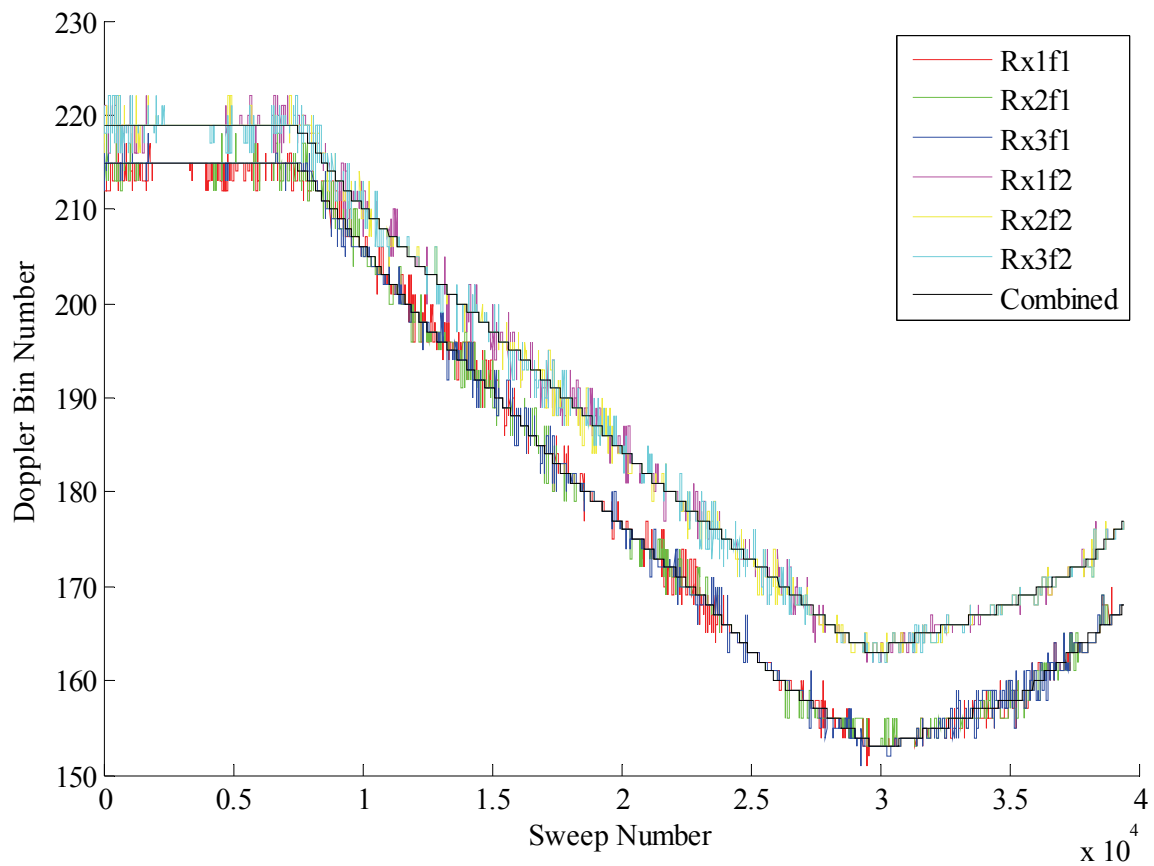


Figure 6.10 Detected Doppler-bins for all channels.

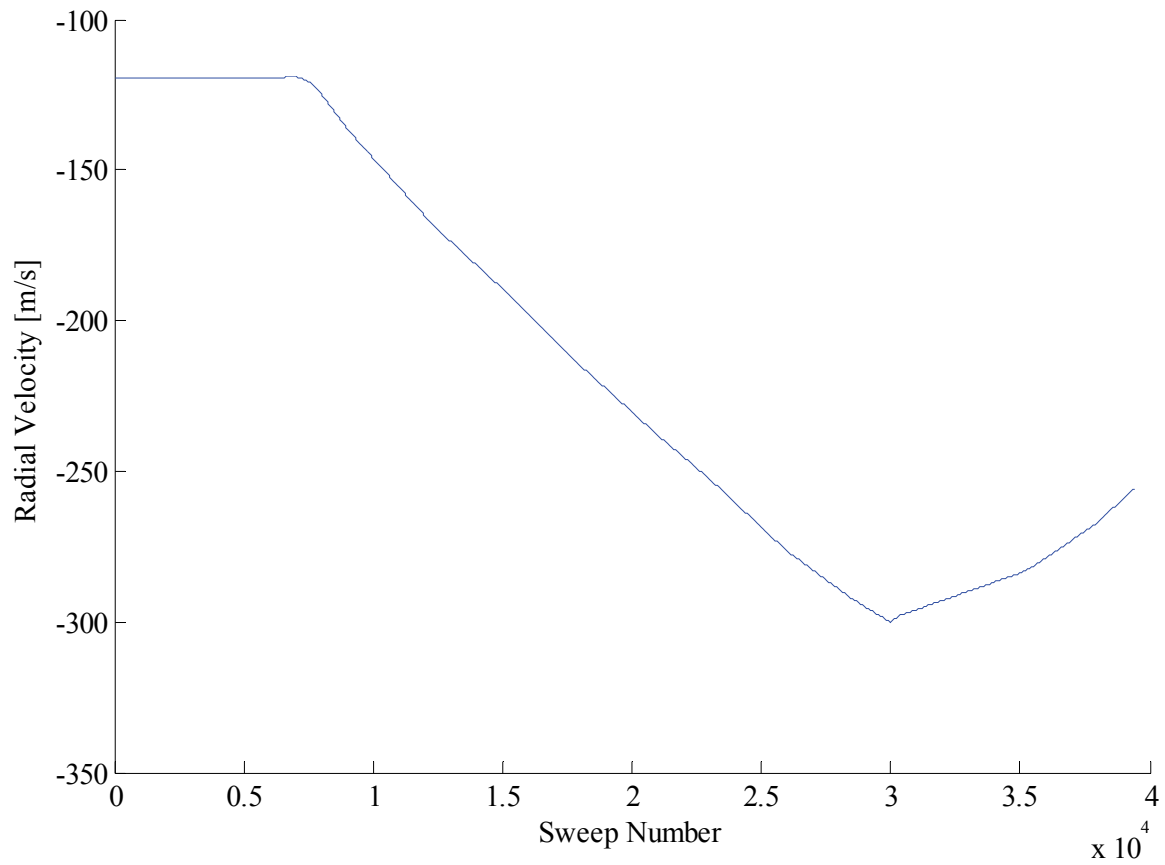


Figure 6.11 Estimated radial velocity.

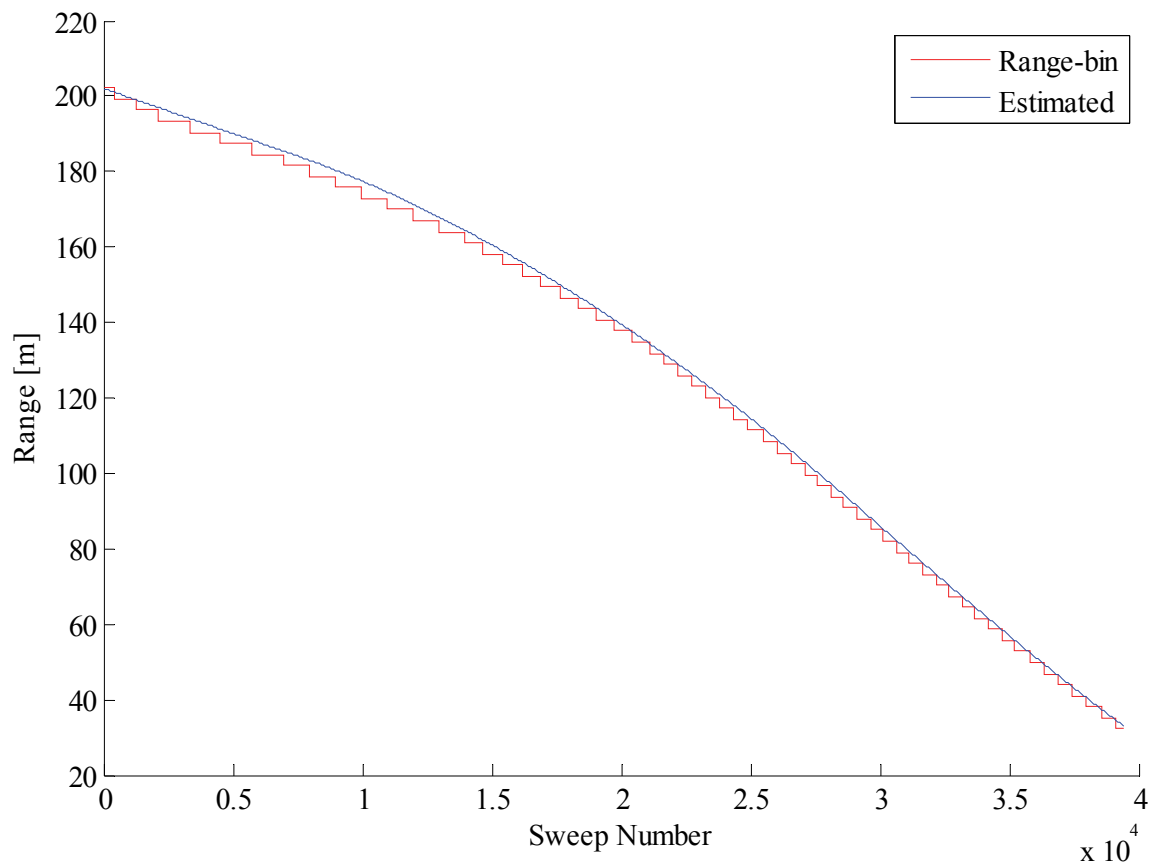
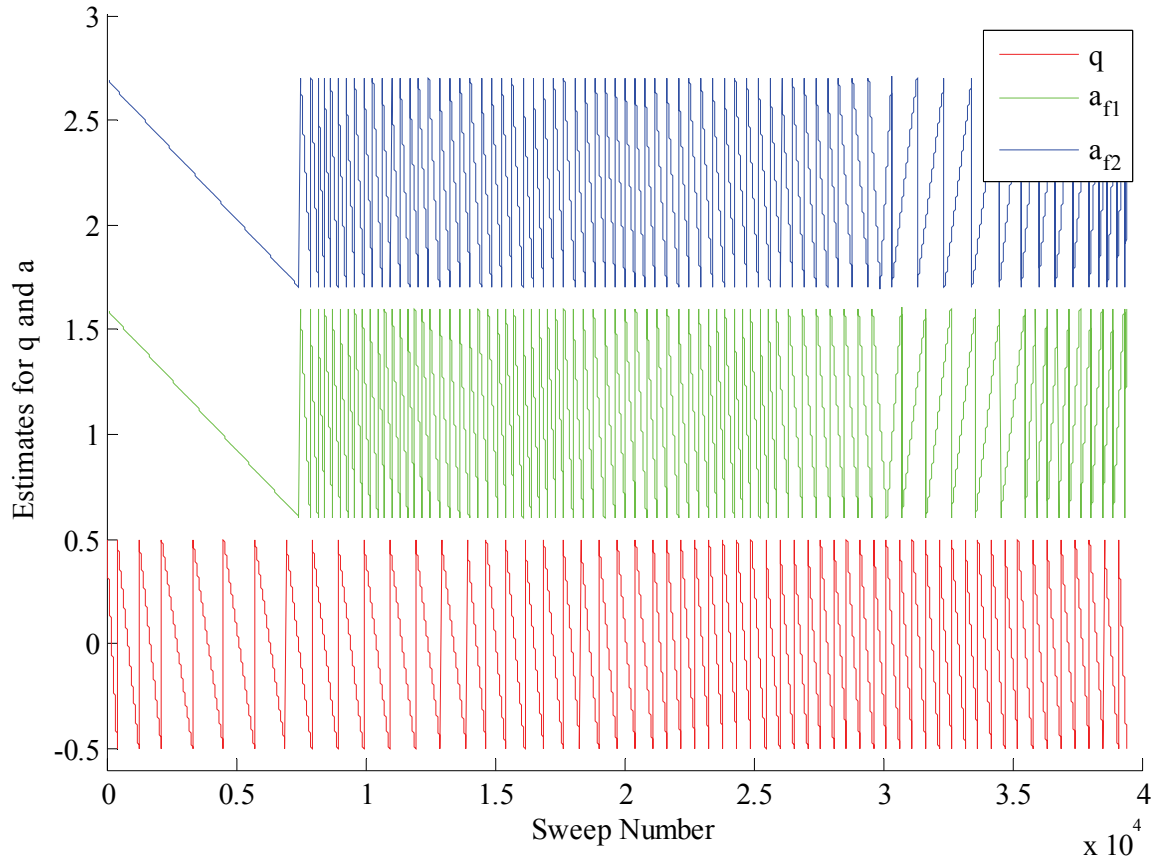


Figure 6.12 Comparison of estimated range and corresponding bin range.


 Figure 6.13 Estimates for q and a (offset from each other for clarity).

The next step is to combine all these estimates to calculate Φ_{est2} :

$$\begin{aligned}\Phi_{est2} &= \Phi_{est1} - \pi q_{est} - \pi a_{est} \\ &= \left(\Phi_{mp} + \Phi_{\Delta mp} \frac{1}{2} N_D \right) + \Phi_{Remainder}\end{aligned}\quad (6.11)$$

Φ_{est2} for all six channels is shown in Figure 6.14. These phases, which comprise a multipath component and a remainder component, are unwrapped, producing the graphs in Figure 6.15. An appropriately scaled version of the range graph is subtracted from each channel's unwrapped phase, which produces the estimates in Figure 6.16. These graphs are fairly close to the desired multipath error phases, with only a small portion of $\Phi_{Remainder}$ that still has to be accounted for. A final estimate, comprised of several straight lines, is subtracted to produce the single-channel multipath error estimates shown in Figure 6.17.

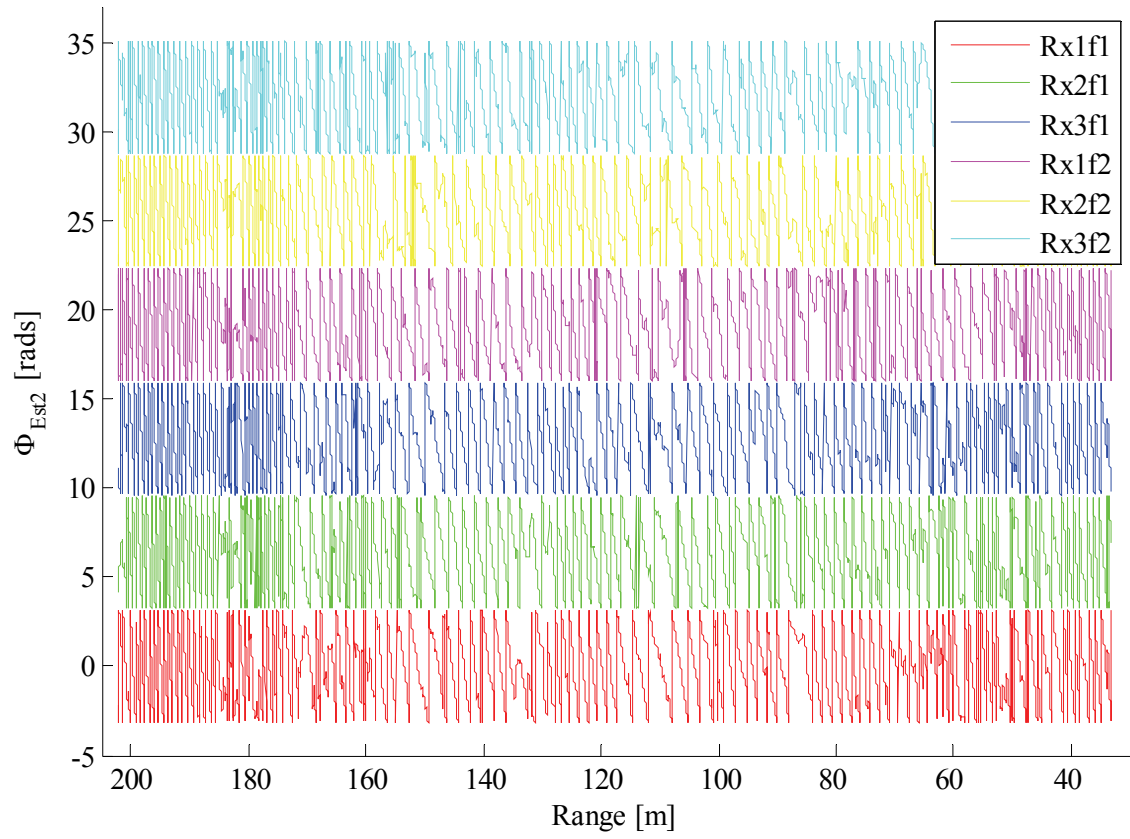


Figure 6.14 Compensated burst phase for all channels.

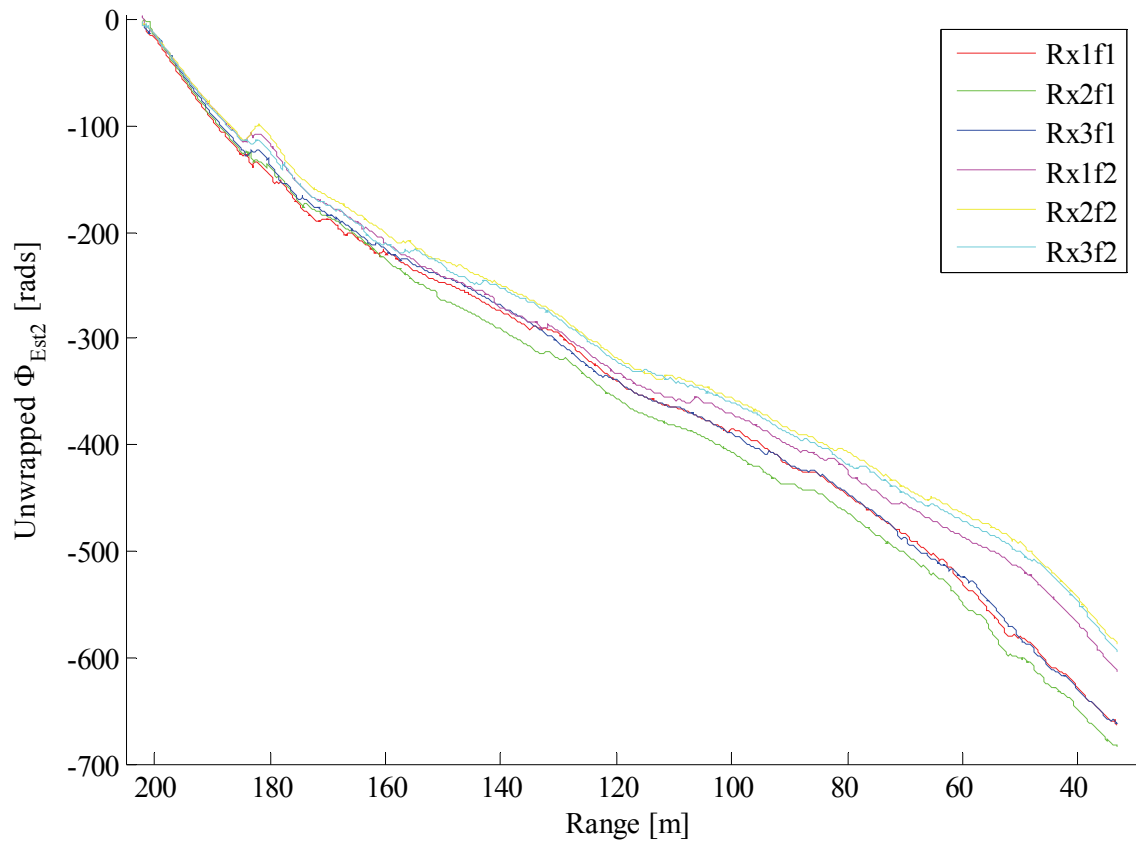


Figure 6.15 Unwrapped, compensated burst phase for all channels.

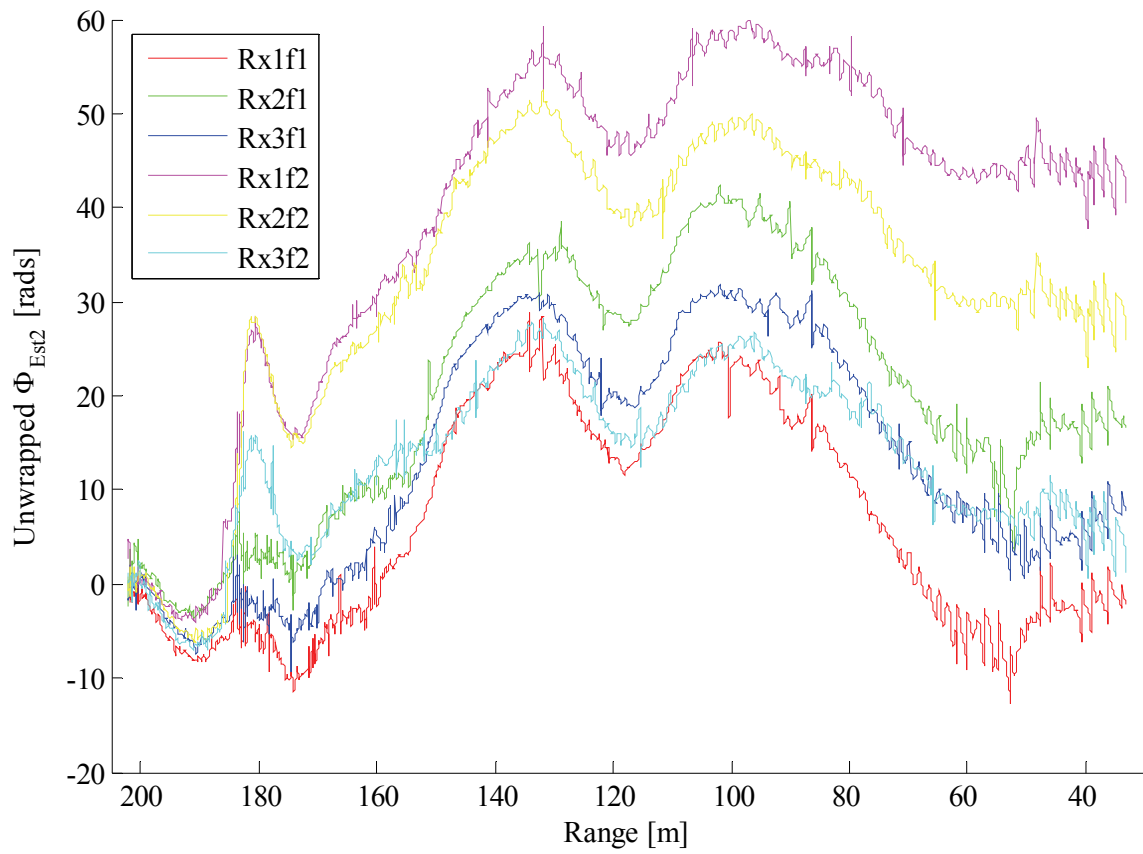


Figure 6.16 Unwrapped, compensated burst phase for all channels after additional correction.

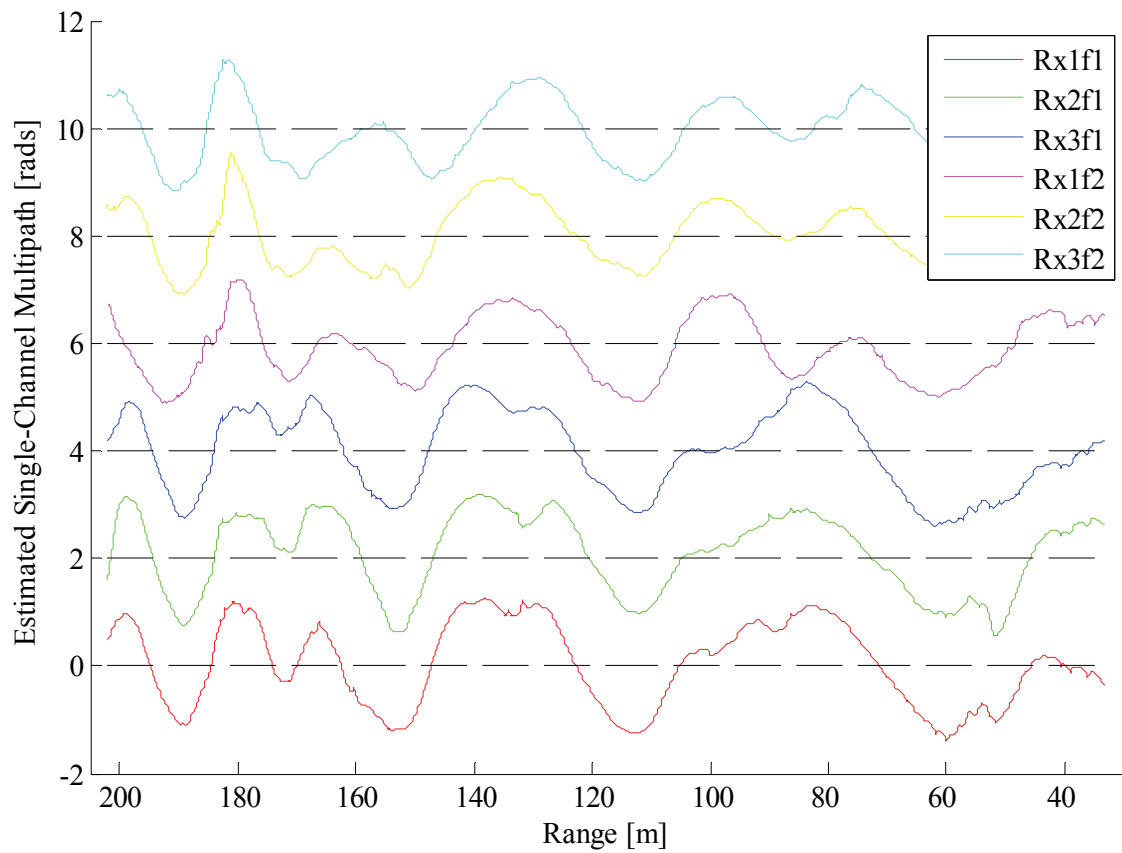


Figure 6.17 Single-channel multipath phase error estimates.

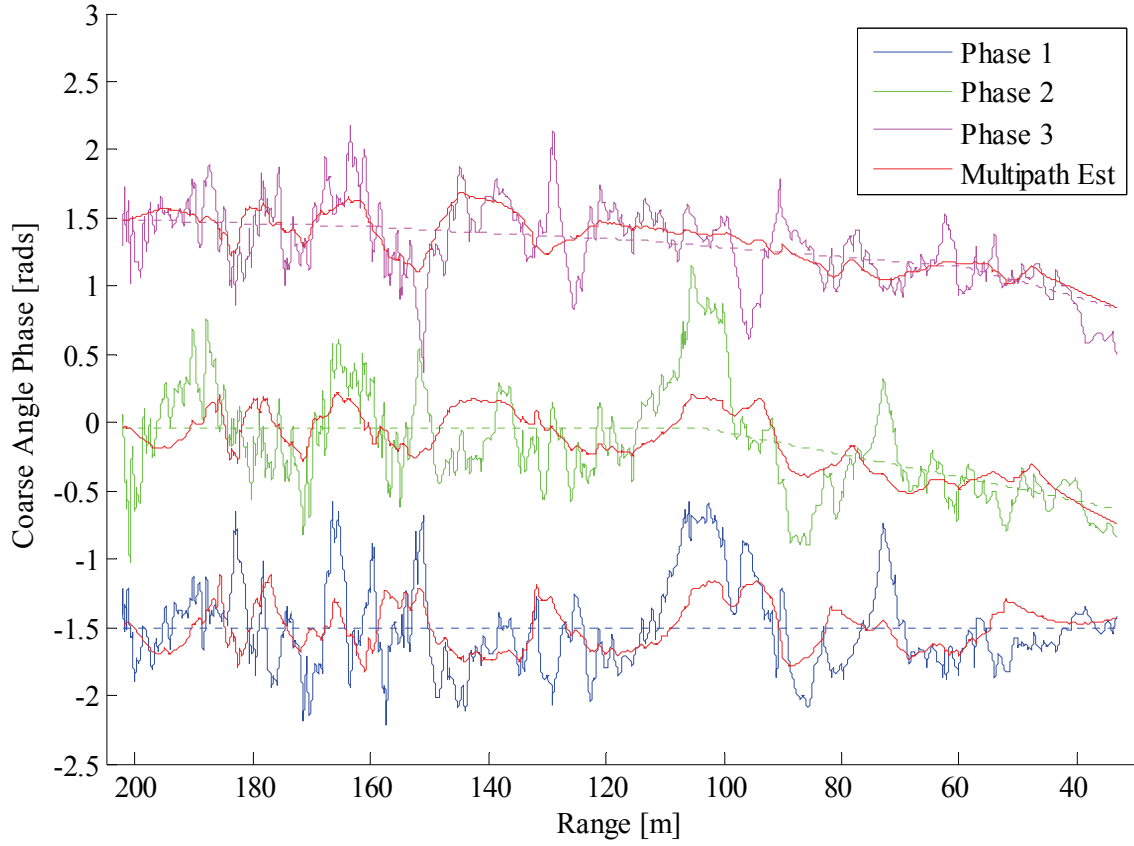


Figure 6.18 Comparison between coarse angle phases and their estimated multipath components. Expected coarse angle phases (calculated from the physical geometry of the measurement setup) are displayed as dashed lines.

Figure 6.18 shows the result when combining all the single-channel multipath estimates during coarse angle extraction. Recall from Section 5.4 that an artificial operating frequency can be created by subtracting the phase difference at f_2 from the phase difference at f_1 , which can be used to resolve the angle ambiguity when receiver spacing is larger than $\lambda/2$. The antenna configuration used during this set of measurements (see Section 5.2.3) will have the following coarse angle phases:

$$\Phi_{ca1} = (\Phi_{rx1f1} - \Phi_{rx2f1}) - (\Phi_{rx2f2} - \Phi_{rx1f2}) \quad (6.12)$$

$$\Phi_{ca2} = (\Phi_{rx1f1} - \Phi_{rx3f1}) - (\Phi_{rx3f2} - \Phi_{rx1f2}) \quad (6.13)$$

$$\Phi_{ca3} = (\Phi_{rx2f1} - \Phi_{rx3f1}) - (\Phi_{rx3f2} - \Phi_{rx2f2}) \quad (6.14)$$

Subtracting the coarse angle multipath estimates in Figure 6.18 from Φ_{ca1} , Φ_{ca2} and Φ_{ca3} reduces the mean error by 14.4%, -3% and 22.9% respectively.

6.2 Method 2: Sum-Difference Processing

This method compares the difference and sum of consecutive sweeps in an attempt to estimate the second multipath term ($\Phi_{\Delta mp}$). Recall the following expression for sweep n from (4.14):

$$\begin{aligned} s_{IF}(t, n) &= A \cos(2\pi f_{IF}t + 2\pi f_{\Delta}nt + \Phi_0 + \theta_{\Delta}n + 2\pi f_{sq}t^2 \\ &\quad + 2\pi f_{error}t - \Phi_{error} + \Phi_{mp} + \Phi_{\Delta mp}n) \\ &= A \cos(X) \end{aligned} \quad (6.15)$$

and for sweep $n + 1$:

$$\begin{aligned} s_{IF}(t, n + 1) &= A \cos(2\pi f_{IF}t + 2\pi f_{\Delta}nt + \Phi_0 + \theta_{\Delta}n + 2\pi f_{sq}t^2 \\ &\quad + 2\pi f_{error}t - \Phi_{error} + \Phi_{mp} + \Phi_{\Delta mp}n + 2\pi f_{\Delta}t + \theta_{\Delta} + \Phi_{\Delta mp}) \\ &= A \cos(X + Y) \end{aligned} \quad (6.16)$$

Sum and difference signals can be defined as:

$$\begin{aligned} s_{\Sigma}(t, n) &\triangleq s_{IF}(t, n + 1) + s_{IF}(t, n) \\ &= A \cos(X + Y) + A \cos(X) \\ &= 2A \cos \frac{Y}{2} \cos \frac{2X + Y}{2} \end{aligned} \quad (6.17)$$

and

$$\begin{aligned} s_{\Delta}(t, n) &\triangleq s_{IF}(t, n + 1) - s_{IF}(t, n) \\ &= A \cos(X + Y) - A \cos X \end{aligned}$$

$$= -2A \sin \frac{Y}{2} \sin \frac{2X + Y}{2} \quad (6.18)$$

The signals described by (6.17) and (6.18) can be subjected to range-Doppler processing in the same way that regular input signals would be. Dividing the burst amplitude of the difference signal by the burst amplitude of the sum signal produces the following:

$$\begin{aligned} \frac{Amp\{s_{\Delta}\}}{Amp\{s_{\Sigma}\}} &= \frac{2A \sin \frac{Y}{2}}{2A \cos \frac{Y}{2}} \\ &= \tan \frac{Y}{2} \end{aligned} \quad (6.19)$$

Taking the arctangent of (6.19) gives an estimate for Y :

$$\begin{aligned} 2 \operatorname{atan} \left(\frac{Amp\{s_{\Delta}\}}{Amp\{s_{\Sigma}\}} \right) &= Y \\ &= 2\pi f_{\Delta} t + \theta_{\Delta} + \Phi_{\Delta mp} \\ &\approx \theta_{\Delta} + \Phi_{\Delta mp} \end{aligned} \quad (6.20)$$

Radial velocity determines θ_{Δ} , which means that the multipath term ($\Phi_{\Delta mp}$) can be estimated.

6.2.1 Algorithm Description

Figure 6.19 contains a flow diagram that describes the sum-difference processing method. Raw input signal data from a single channel are used to construct the sum and difference signals. After range-Doppler processing, the amplitude information (from the same range-Doppler-bin as the original detection) is used to estimate Y . Velocity data is used to estimate θ_{Δ} , which is subtracted from Y_{est} to give $\Phi_{\Delta mp-est}$. Integration is applied to obtain an estimate of the multipath phase error, which can then be subtracted from corrupted burst phase measurements to improve accuracy.

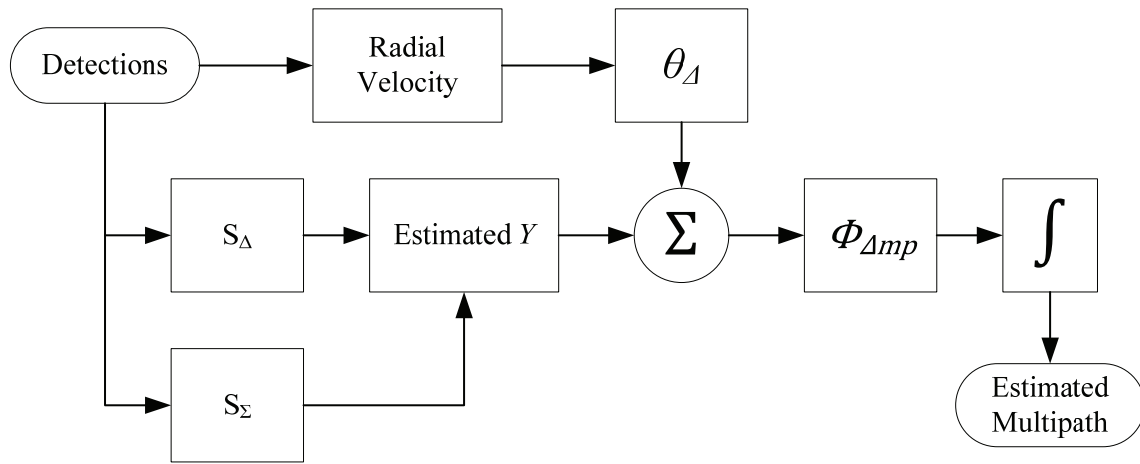


Figure 6.19 Sum-difference processing algorithm.

6.2.2 Simulation Example

Table 6.2 Simulation parameters.

Parameter	Value	Notes
Target Velocity	-400 m/s	Velocity remained constant.
Initial Target Range	20 m	
Target Placement (Height, Offset)	(1 m, 0 m)	Target directly in front of radar.
Target Attitude (Azimuth, Elevation)	(0 rads, 0 rads)	Target moved directly towards radar.
SNR	50 dB	After range-Doppler processing.
Antenna Separation Distance	0.15 m	
Operating Frequencies (f_1, f_2)	(10.1 GHz, 9.1 GHz)	
Sample Rate, f_s	15.625 MHz	
Samples per Sweep, N_R	256	
Sweeps per Burst, N_D	256	
Sweep Duration, T_{rep}	20 μ s	
Sweep Rate, μ	3.125 THz/s	
Reflection Coefficient, $ I $	0.5	

Table 6.2 contains all the relevant simulation parameters for this example. Figure 6.20 shows the estimated $\Phi_{\Delta mp}$ after applying sum-difference processing and removing the velocity component (θ_A). Integrating this result produces an estimate for multipath phase error, shown in Figure 6.21. Care must be taken to remove any erroneous offset before integration, as this could lead to large errors in estimated multipath.

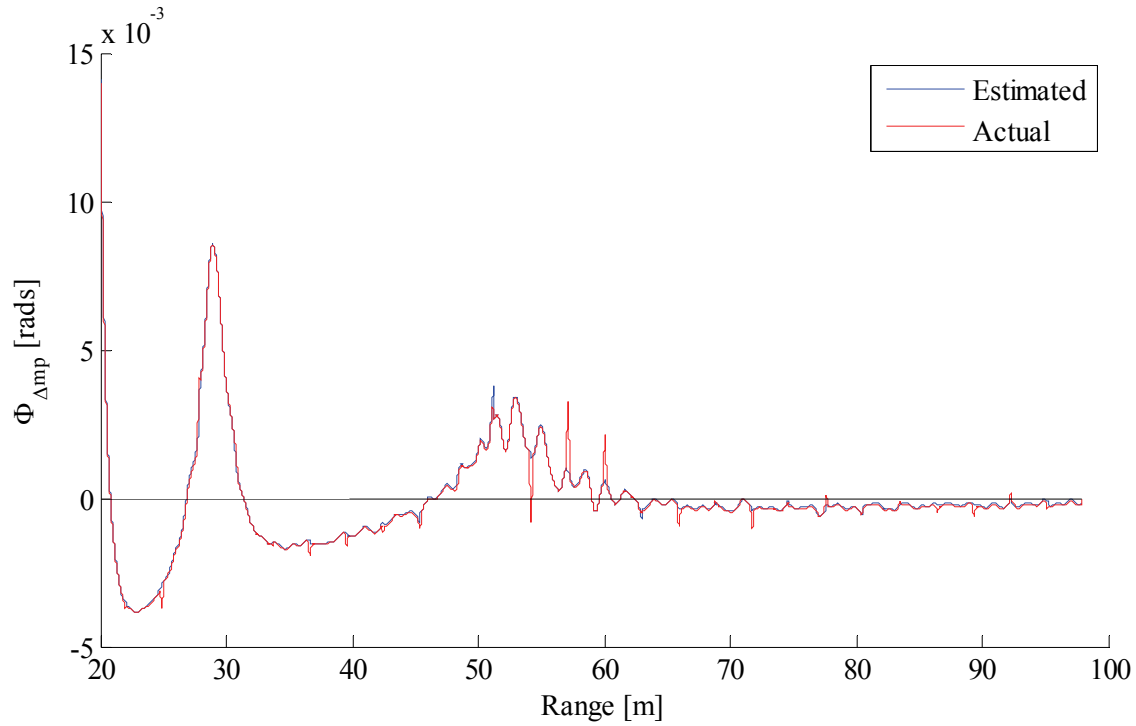


Figure 6.20 Comparison between estimated and actual multipath phase difference.

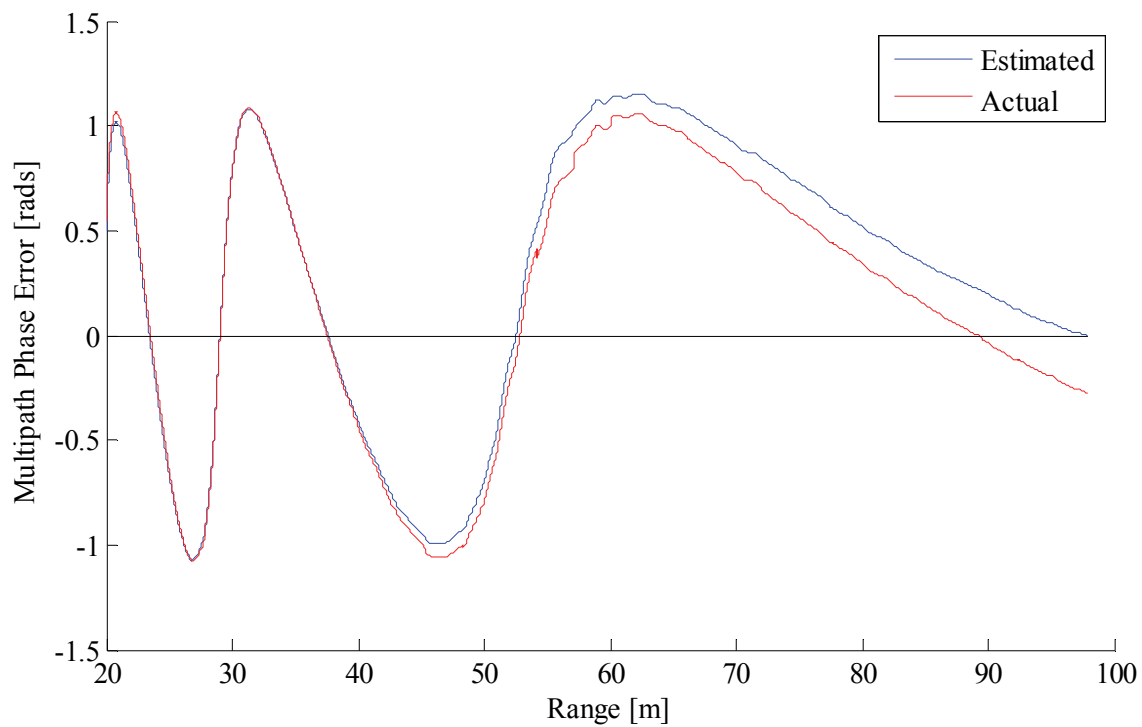


Figure 6.21 Comparison between estimated and actual multipath phase error.

6.2.3 Measured Data Example

The same data that was captured and used in Section 6.1.3 will be used here. After sum-difference processing, an estimate for Y is obtained, shown here in Figure 6.22. The two graphs are very similar in shape to the radial velocity from 6.1.3 (as expected). Removing θ_A gives an estimate of $\Phi_{\Delta mp}$, of which an example is illustrated in Figure 6.23.

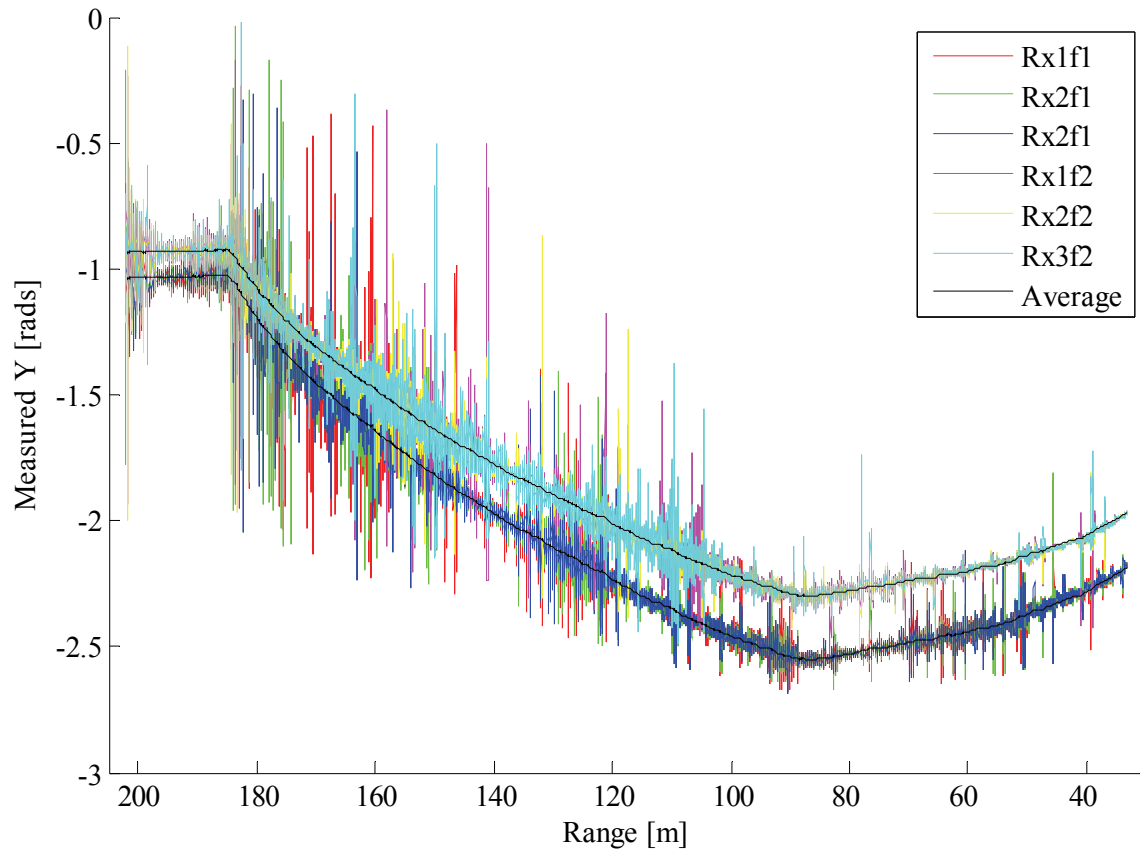


Figure 6.22 Estimated Y for all channels.

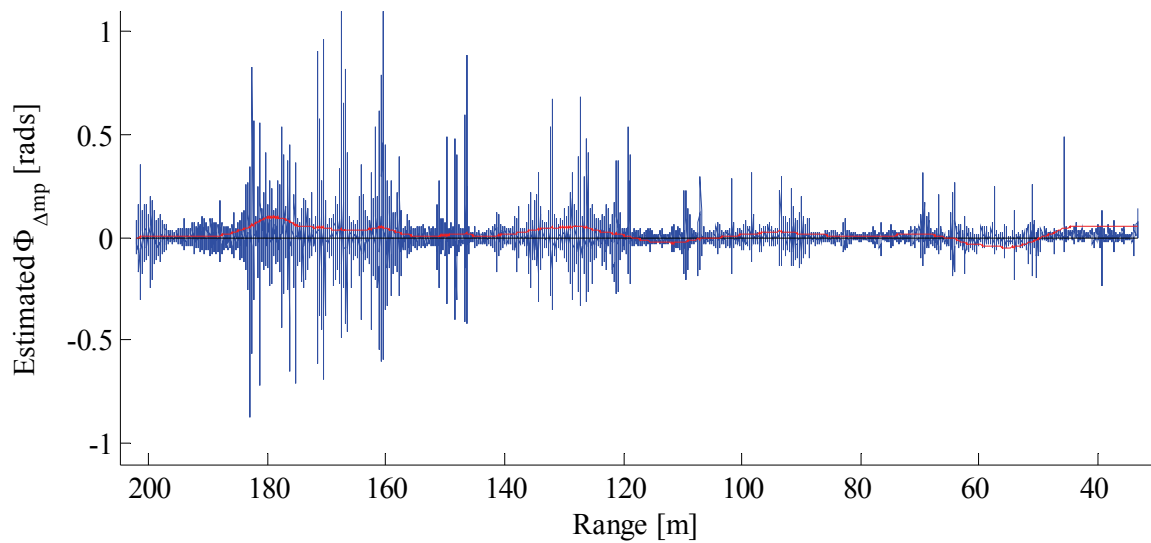
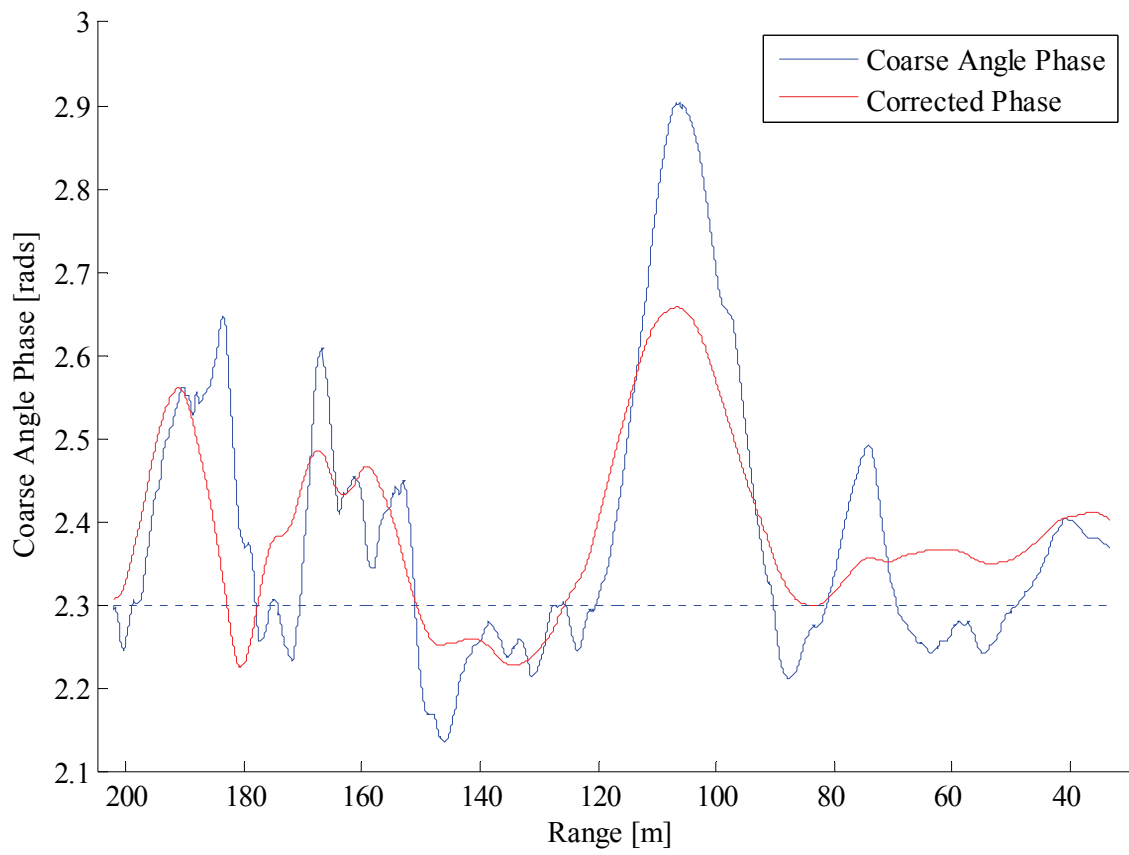
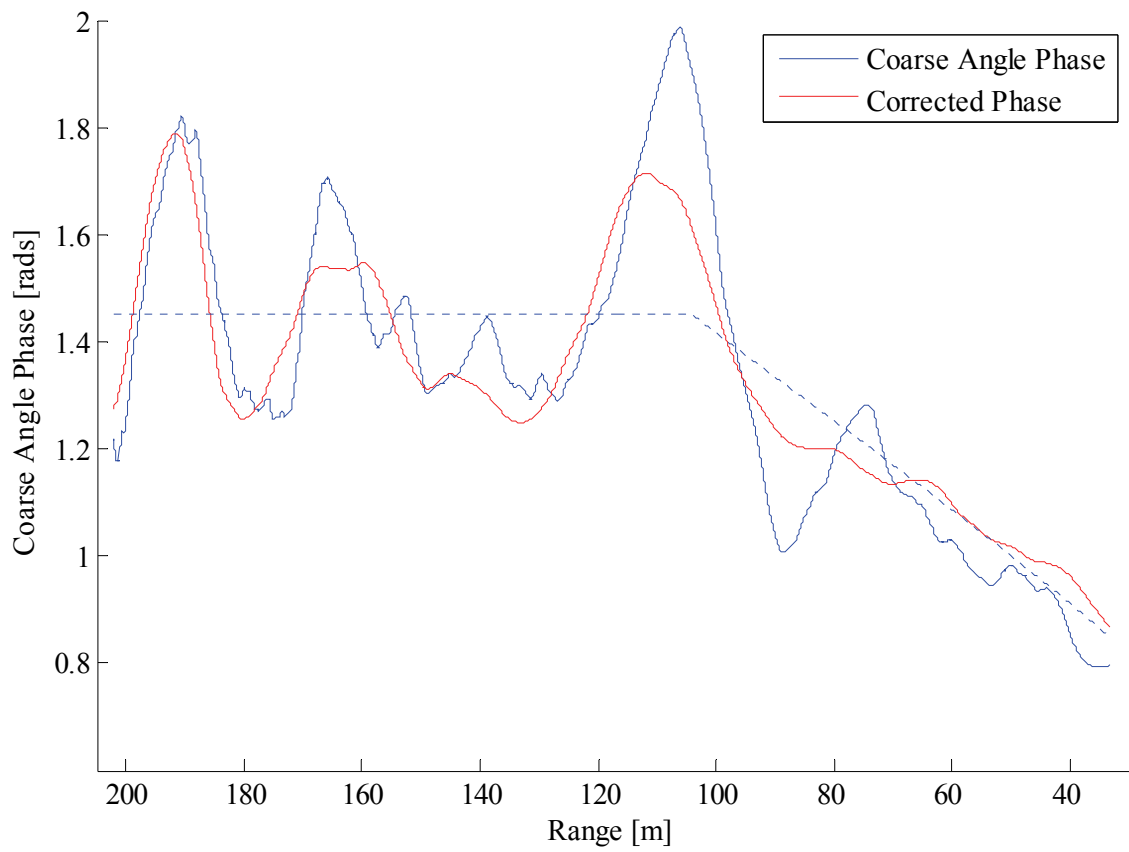


Figure 6.23 Estimated multipath phase difference for Rx1f1 channel, shown in blue. A magnified version of the offset correction is shown in red.



(a)



(b)

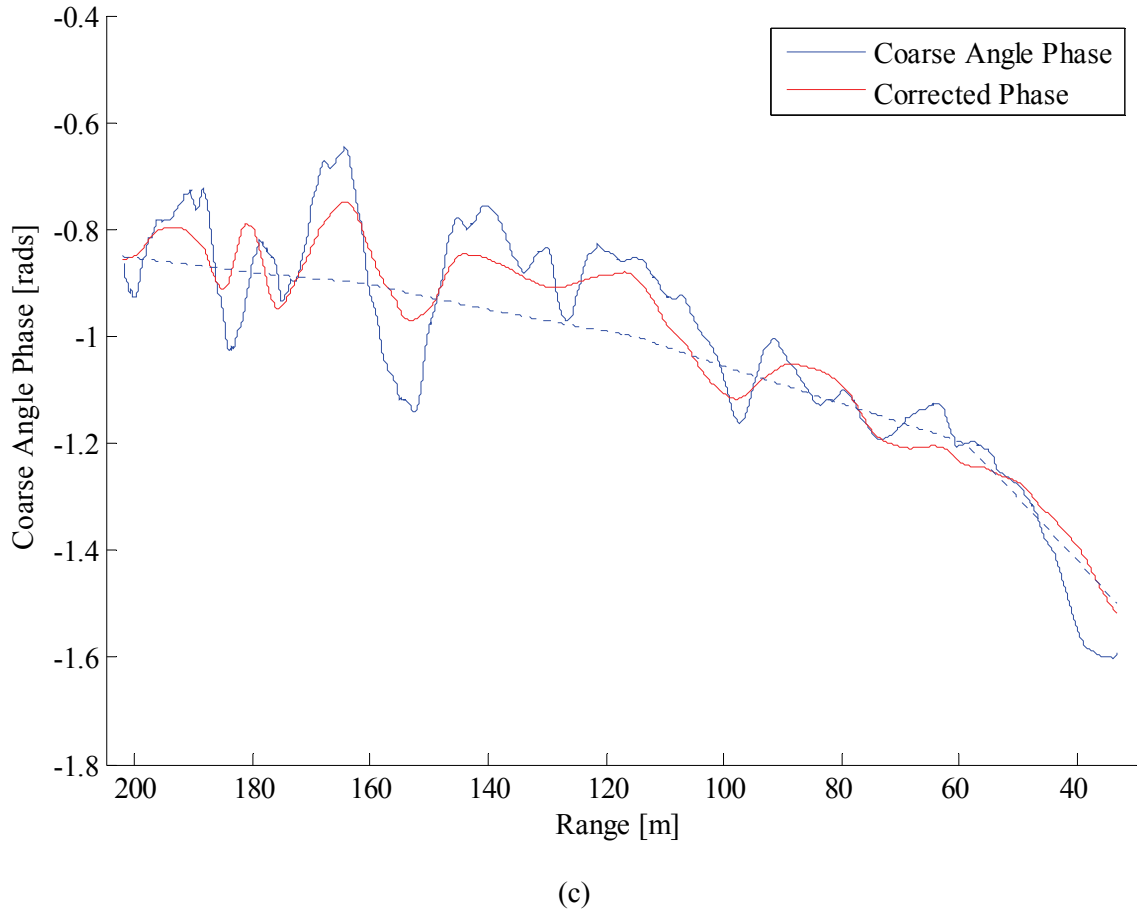


Figure 6.24 Comparison between corrected and non-corrected coarse angle phase for (a) Φ_{ca1} , (b) Φ_{ca2} and (c) Φ_{ca3} .

Figure 6.24 (a), (b) and (c) show the original coarse angle phases (Φ_{ca1} , Φ_{ca2} and Φ_{ca3}) with their respective multipath corrected versions. Mean error reductions of 15.5%, 20.3% and 41.7% were achieved.

6.3 Method 3: Filtering

This section will investigate a basic α -filter solution as mitigation method. The assumption is that the AoA will change slowly over time, as compared with multipath phase errors, noise interference and other disturbances. A suitable low-pass filter should be able to suppress unwanted signals, while leaving the desired angle information intact.

6.3.1 Filter Description

There are several filter solutions that could potentially be used for this application. The α -filter was selected as a computationally inexpensive option that is also very simple to design. It is well known from radar tracking that α - β filtering is an effective method for estimating position from noisy observation data [55] [56] [57].

The working of an α -filter is described by (6.21):

$$x_n = x_{n-1} + \alpha x_{res} \quad (6.21)$$

and

$$x_{res} = x_{obs} - x_{n-1}$$

where x_n is the filtered output,

x_{res} is the residue (difference between a new observation x_{obs} and the previous output) and

α is a constant that determines how quickly new observation data is incorporated into the filtered output.

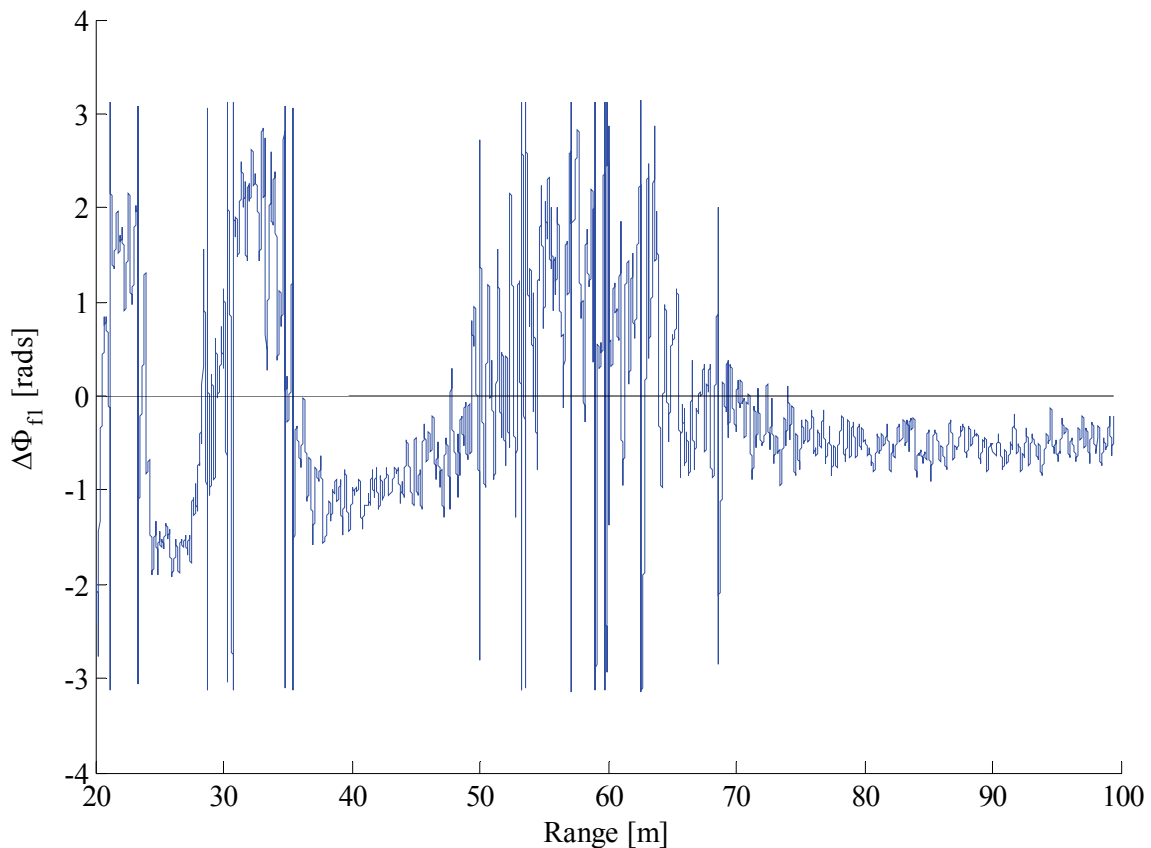
6.3.2 Simulation Example

Table 6.3 Simulation parameters.

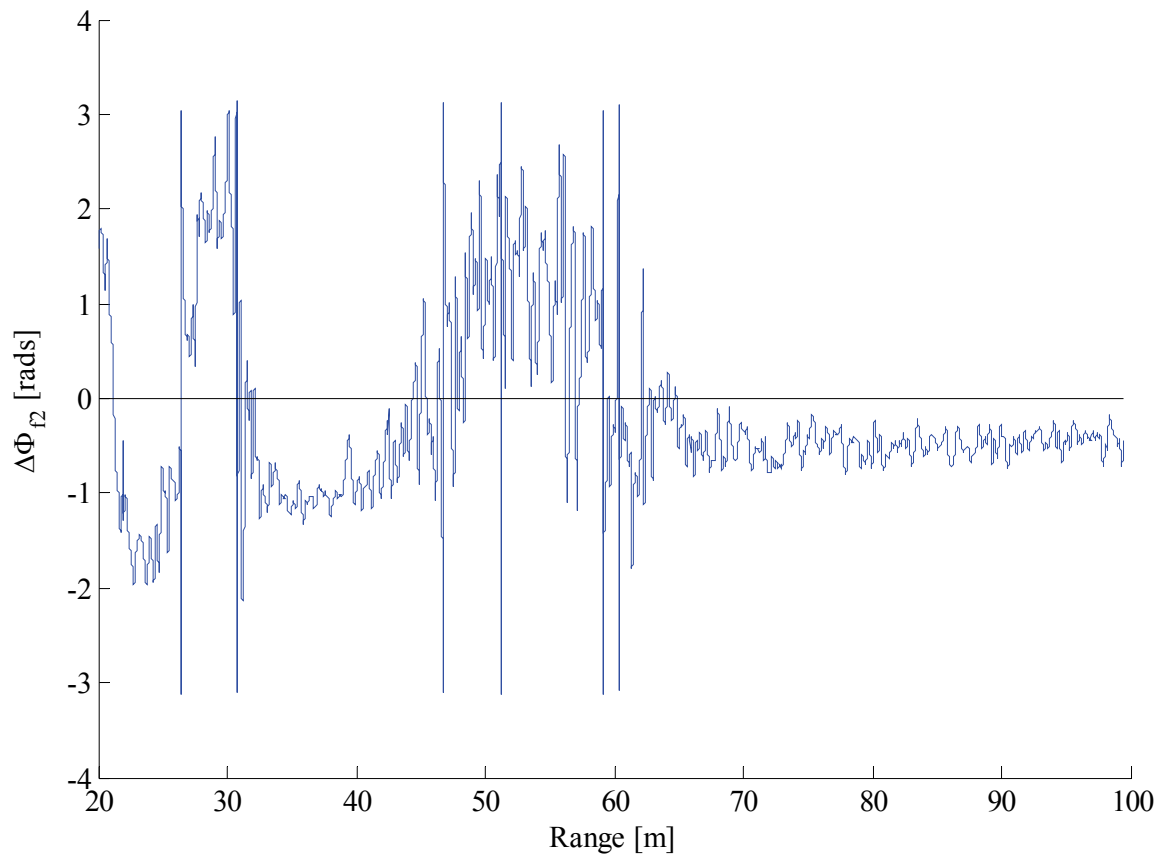
Parameter	Value	Notes
Target Velocity	-100 m/s	Velocity remained constant.
Initial Target Range	20 m	
Target Placement (Height, Offset)	(1 m, 0 m)	Target directly in front of radar.
Target Attitude (Azimuth, Elevation)	(0 rads, 0 rads)	Target moved directly towards radar.
SNR	20 dB	After range-Doppler processing.
Antenna Separation Distance	0.15 m	
Operating Frequencies (f_1, f_2)	(10.1 GHz, 9.1 GHz)	
Sample Rate, f_s	15.625 MHz	
Samples per Sweep, N_R	256	
Sweeps per Burst, N_D	256	
Sweep Duration, T_{rep}	20 μ s	
Sweep Rate, μ	3.125 THz/s	
Reflection Coefficient, $ I $	0.5	

Table 6.3 details all the relevant simulation parameters for this example. Two receive antennas were placed in a vertical line with a distance of 0.15 m between them (approximately 5λ). Severe multipath interference can be seen in Figure 6.25 (a and b), where the burst phase difference ($\Delta\Phi$) for operating frequencies f_1 and f_2 is shown. Figure 6.25 (c) shows the phase difference ($\Delta\Phi$) at f_3 , the artificial operating frequency created by subtracting $\Delta\Phi$ at f_2 from $\Delta\Phi$ at f_1 . It is this phase information that will be used to calculate the coarse angle.

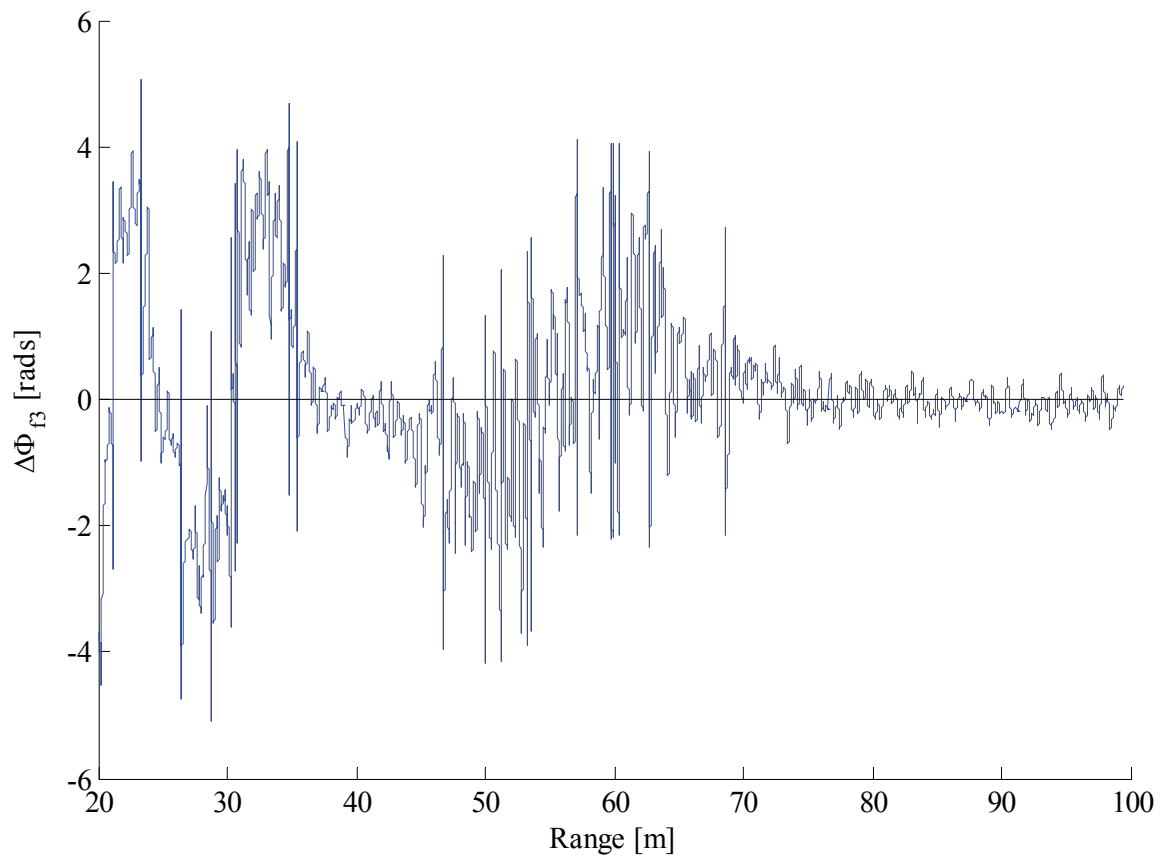
The next step is to apply an α -filter to the coarse angle phase data. There is a design trade-off between filter response time and unwanted signal rejection: if α is chosen too high, the filter will not provide sufficient interference rejection, but if α is chosen too low, it might take a long time for the filter to settle on the correct value. Figure 6.26 (a, b and c) illustrates the effect of different α values. In the case of (a), α was chosen too high and the filter output does not remove multipath interference. Scenario (c) has an α value that is too low, and it takes too long for the output to settle at the correct level. A midway value was chosen for (b); here the filter output provides sufficient multipath suppression (most of the time), while settling time is reduced to an acceptable level.



(a)

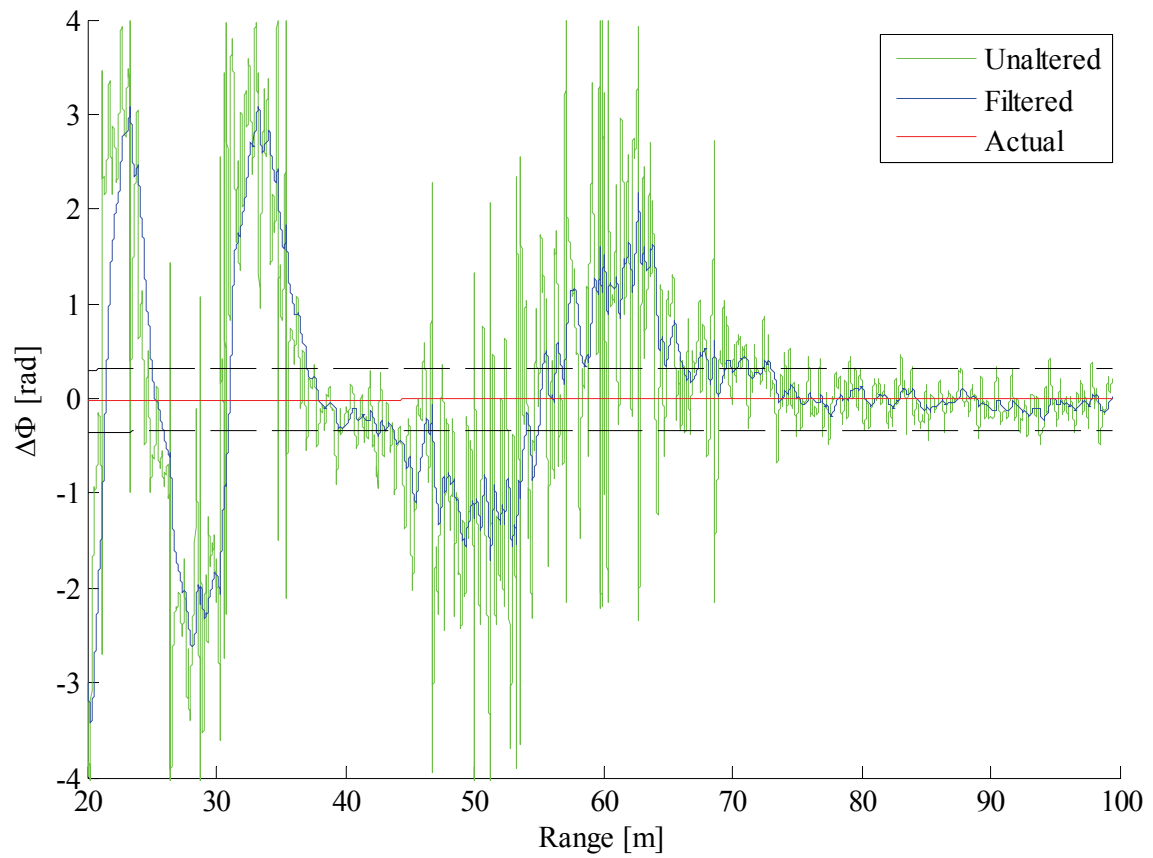


(b)

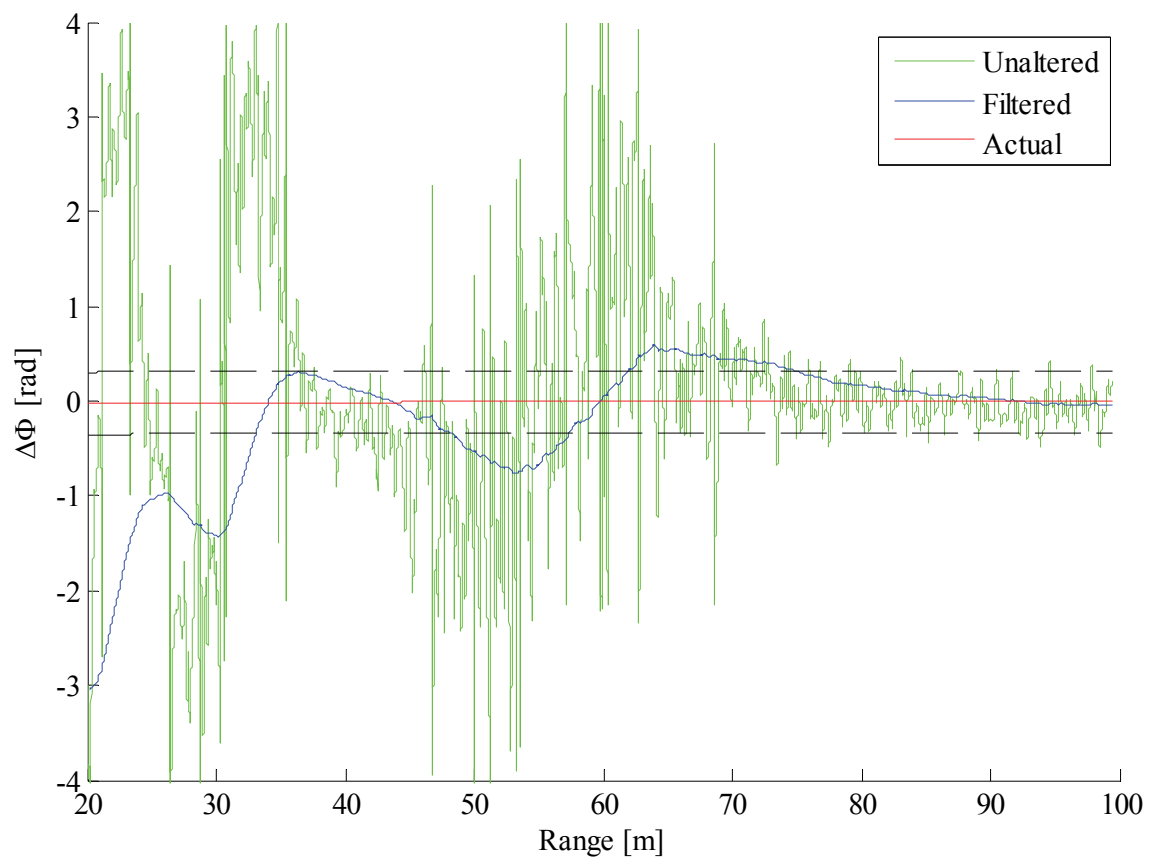


(c)

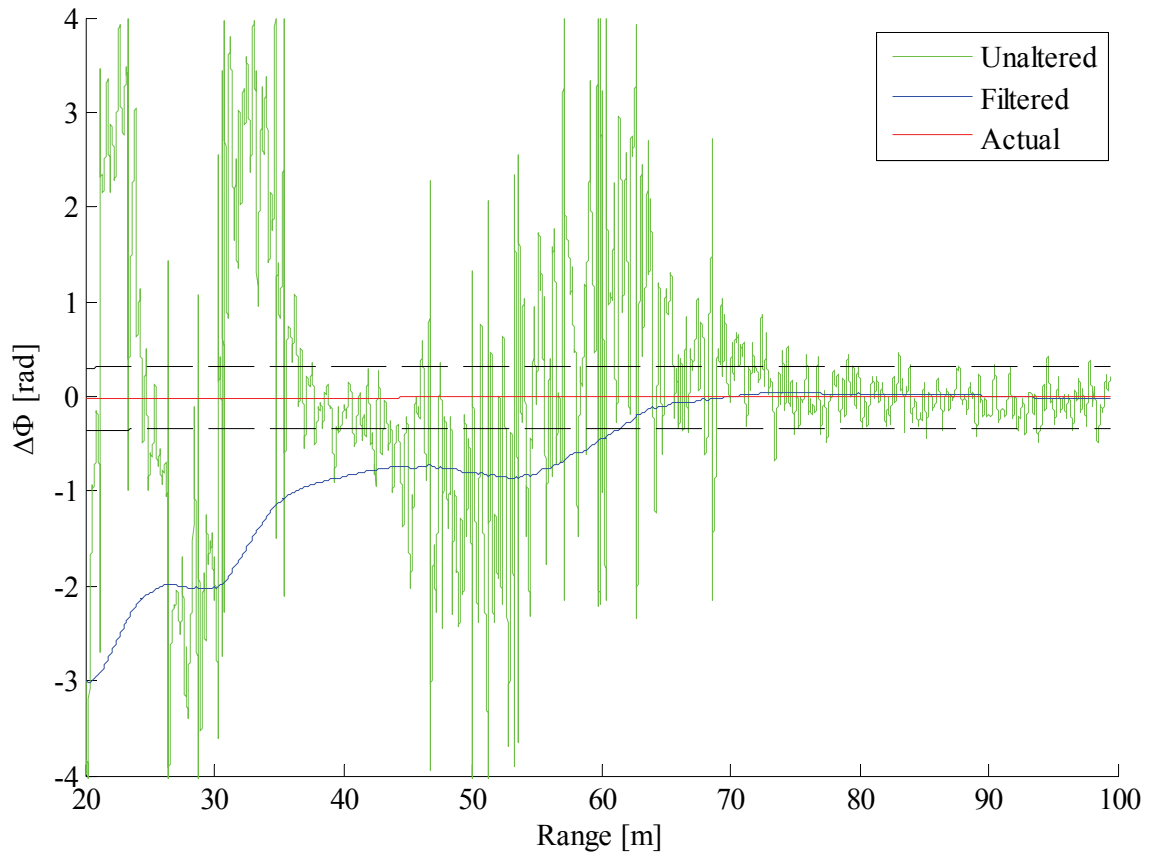
Figure 6.25 Angle-of-arrival phases ($\Delta\Phi$) for (a) $f_1 = 10.1$ GHz, (b) $f_2 = 9.1$ GHz and (c) $f_3 = f_1 - f_2 = 1$ GHz.



(a)



(b)



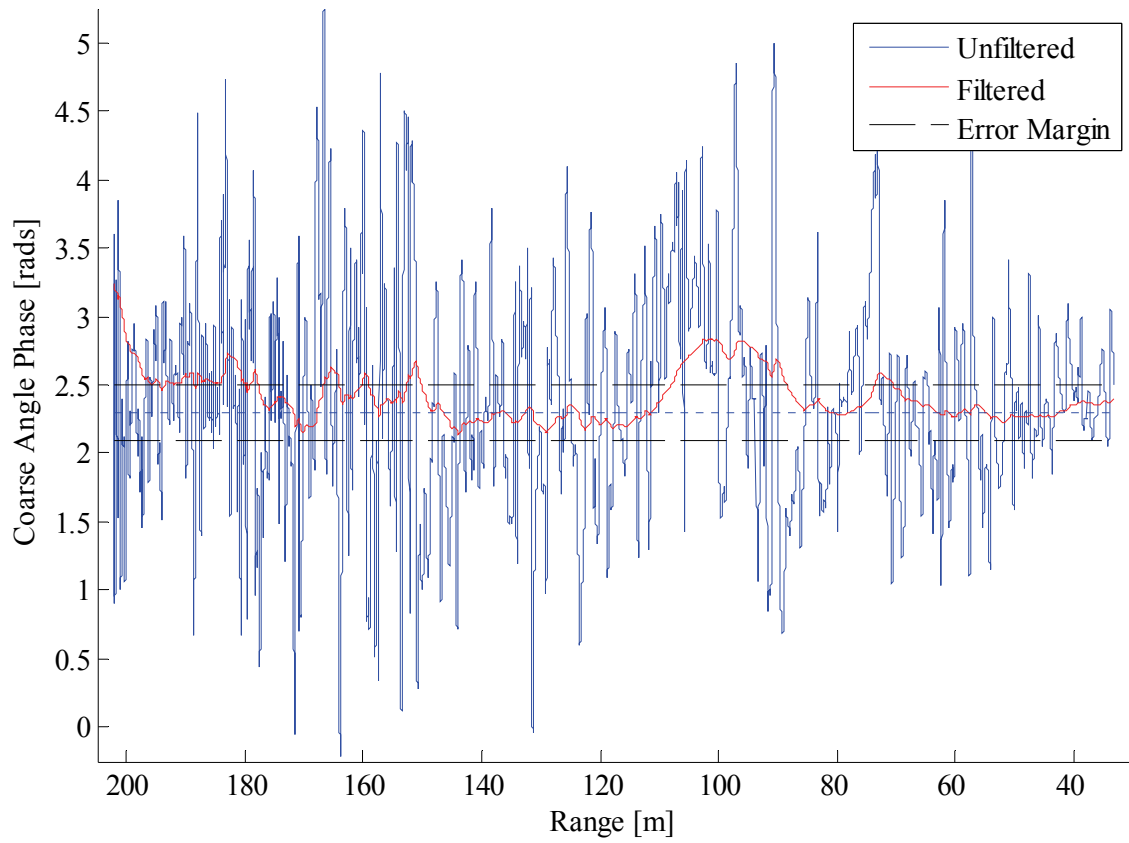
(c)

Figure 6.26 Comparison of filtered and unfiltered coarse angle phase ($\Delta\Phi$ at f3) for (a) $\alpha = 1/300$, (b) $\alpha = 1/4000$ and (c) $\alpha = 1/10000$.

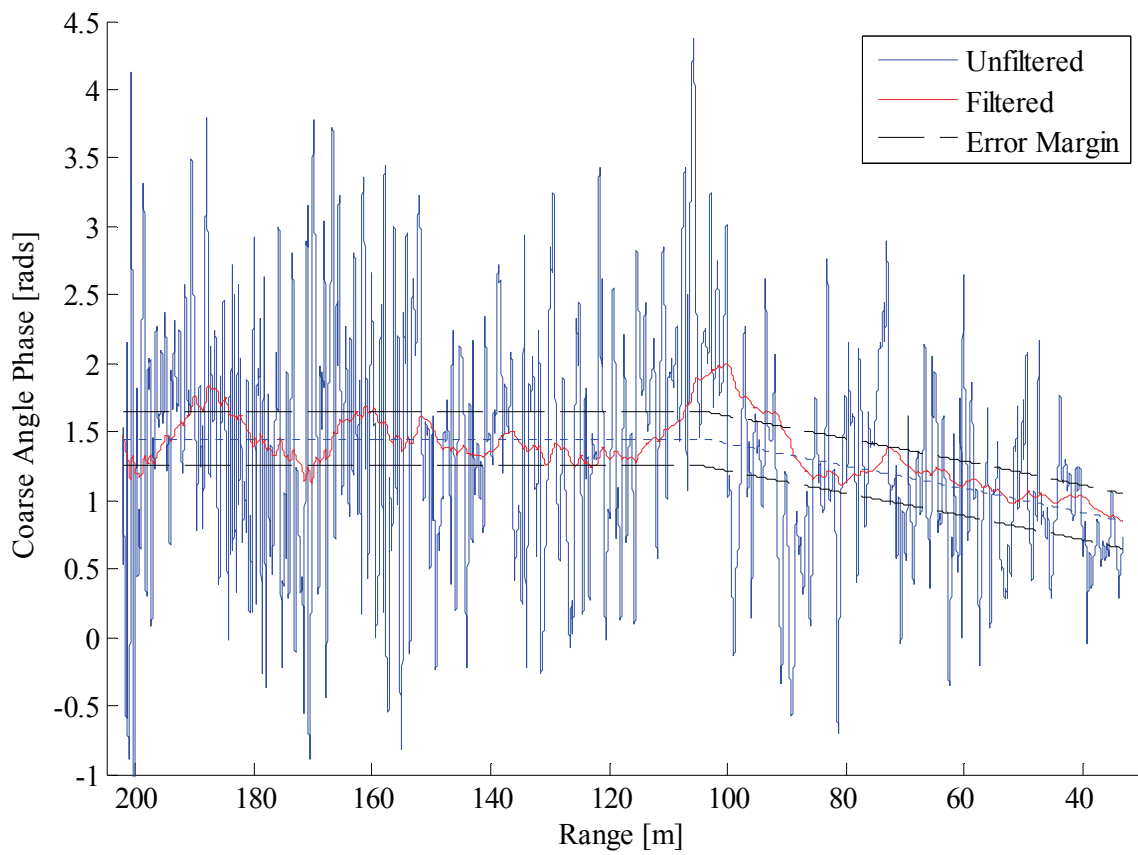
6.3.3 Measured Data Example

The same measurement data from 6.1.3 and 6.2.3 was filtered using an α -filter. Two sets of results are presented: for the first, the initial state of the filter was set to ideal conditions, while the other set of results is for a worst-case scenario. Figure 6.27 (a), (b) and (c) show the unfiltered coarse angle phases (Φ_{ca1} , Φ_{ca2} and Φ_{ca3}) in blue, with the filtered versions superimposed in red. Reductions in mean error of 71.4%, 79.1% and 79.5% were obtained.

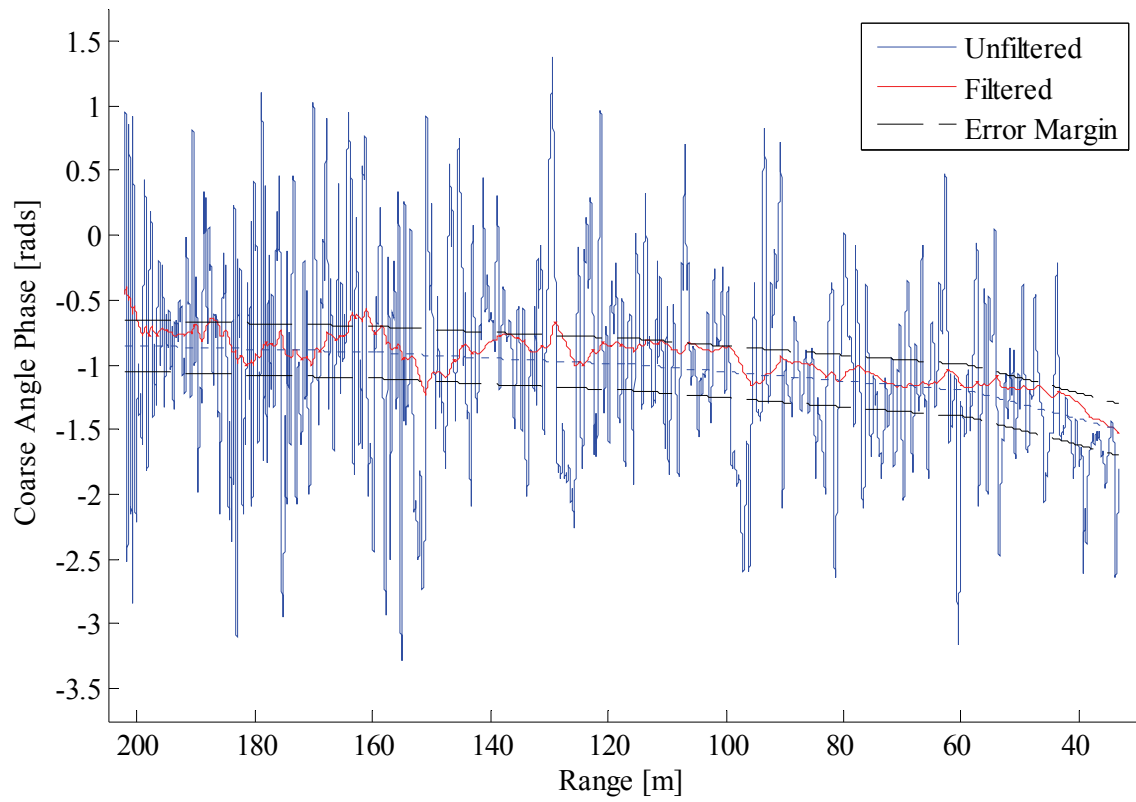
Figure 6.28 (a), (b) and (c) show the same unfiltered coarse angle phases; however, the initial state of the α -filter was set to worst-case values. This was done to see how long it would take for the filter to settle on the correct band. Reductions in mean error of 52.7%, 58.1% and 54.6% were achieved in this non-ideal case.



(a)

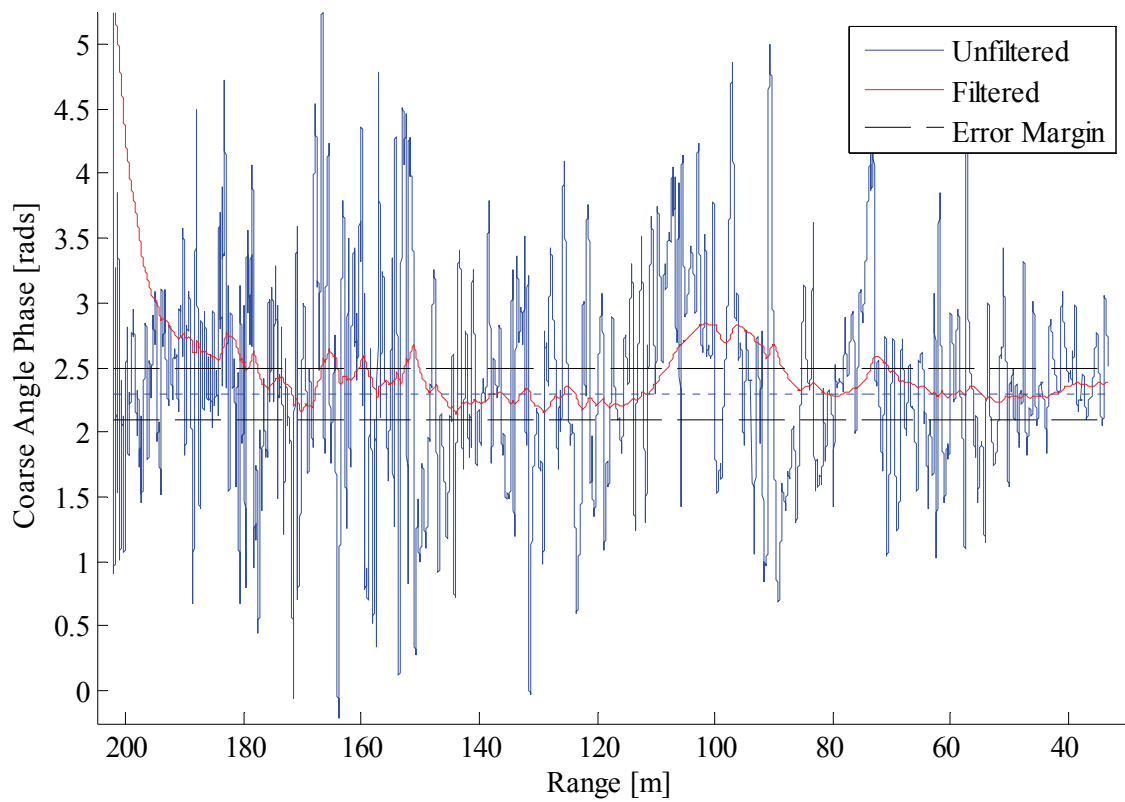


(b)

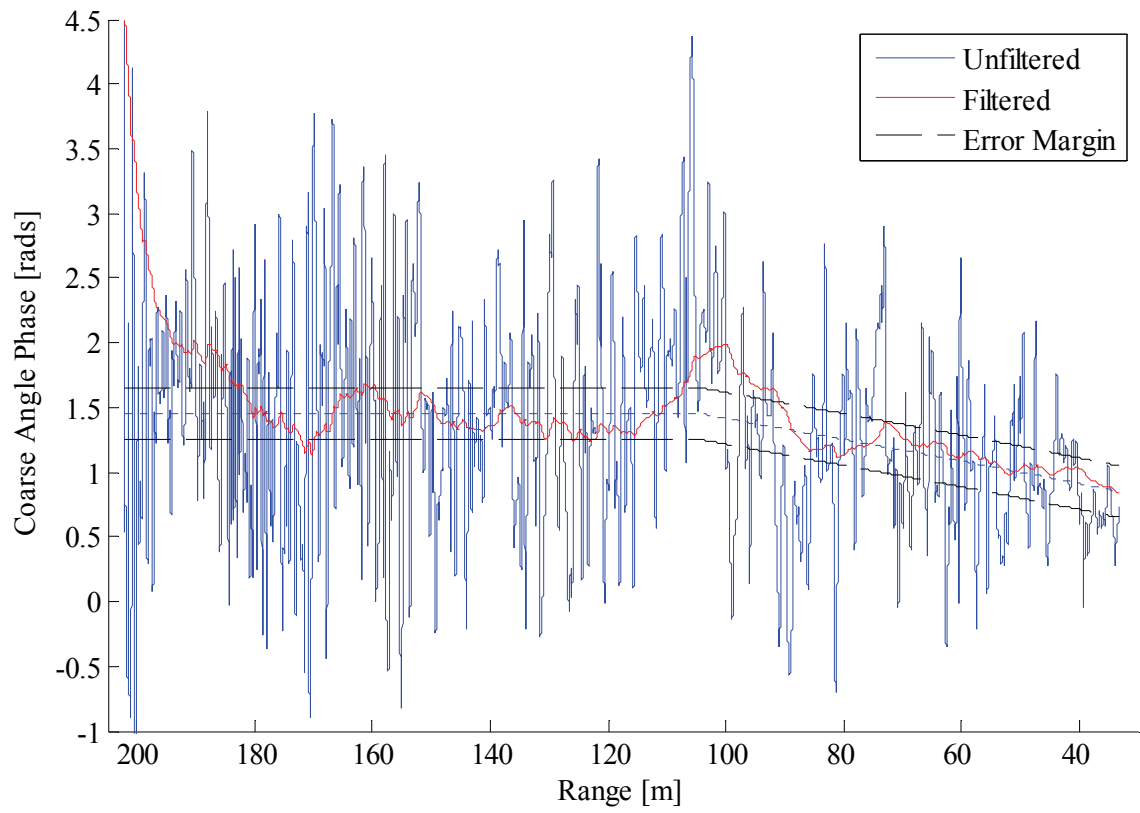


(c)

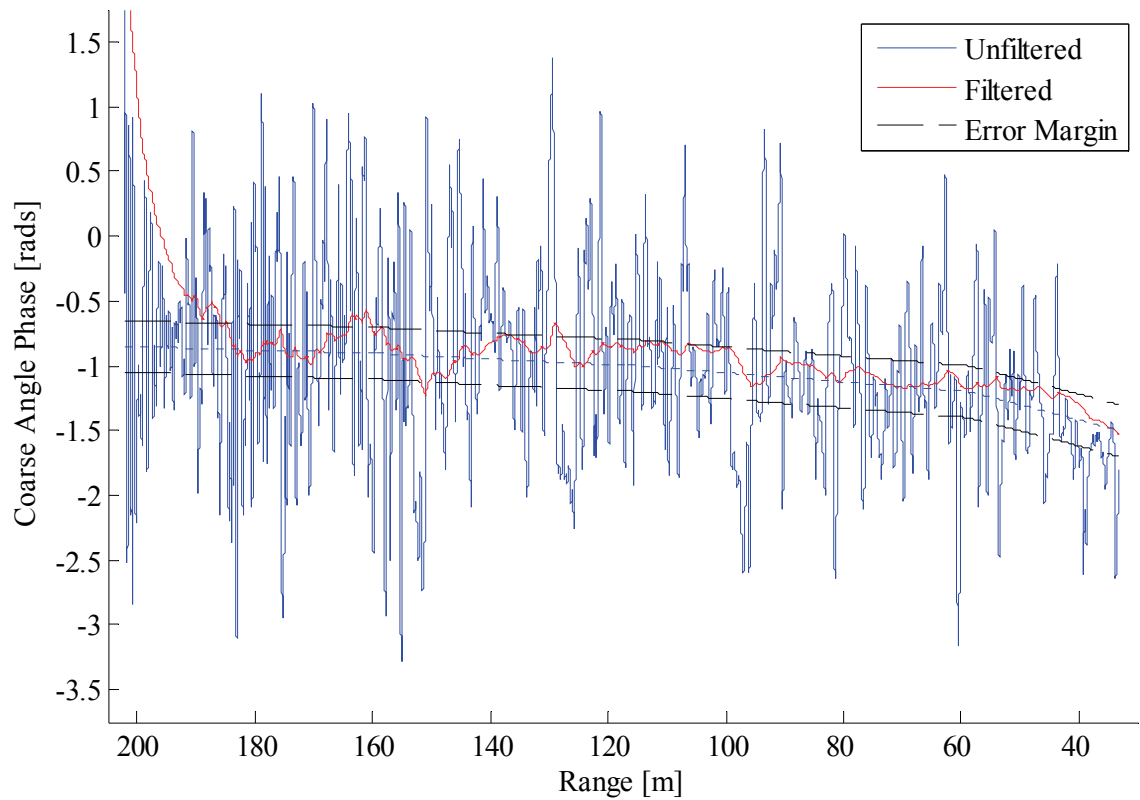
Figure 6.27 Comparison of filtered and unfiltered coarse angle phases for (a) Φ_{ca1} , (b) Φ_{ca2} and (c) Φ_{ca3} . In this example the filter was initialised with favourable values.



(a)



(b)



(c)

Figure 6.28 Comparison of filtered and unfiltered coarse angle phases for (a) Φ_{ca1} , (b) Φ_{ca2} and (c) Φ_{ca3} . In this example the filter was initialised with extreme values.

6.4 Comparison

Table 6.4 provides a quick comparison of the most important aspects of all three mitigation methods. The clear winner is filtering, which provides by far the largest reduction in error and is also the simplest in terms of computational complexity. Whilst the other two methods did show a lot of potential during simulation experiments, they were unable to cope properly with the more erratic nature of a real-world measurement.

Table 6.4 Comparison of mitigation methods.

	Mean Error Reduction	Computational Complexity
Phase Unwrapping	11.4%	Very Complex
Sum-Difference Processing	25.8%	Very Complex
Filtering	76.6%	Simple

There is one way in which phase unwrapping and sum-difference processing can provide more insight into the nature of multipath interference, namely their ability to estimate the multipath phase error for a single channel. In applications where the target is more “well-behaved”, i.e. constant or near constant velocity, the first two mitigation methods should perform much better and should also provide some measure of the multipath error signal itself.

Chapter 7: Conclusions

Radar systems operating in any environment where reflective or partially reflective surfaces are present will suffer from multipath interference. Understanding the effects of the physical environment on transmitted and received signals is crucial when designing mitigation algorithms. Advancements in digital signal processing have extended the capabilities of FMCW radar and have thereby allowed the application thereof in new fields. This study was presented with a unique opportunity – new operating environments and signal processing schemes require novel multipath models.

Several physical environment models were investigated, with a flat, reflective ground surface being selected. A number of multipath mitigation techniques for typical FMCW applications were also studied. Many of these assume an industrial indoor environment with multiple reflective surfaces, which require the application of statistical methodologies. Despite the ingenious approaches of these mitigation methods, they were not suitable for the typical operating parameters of the Active Protection System (or other similar systems).

A rigorous mathematical derivation of the two-dimensional FFT, or range-Doppler, processing method was combined with expressions for phase and amplitude disturbance due to specular multipath for FMCW radar signals. Additional phase terms that are typically ignored were scrutinised to determine the effect they have on the measured burst phase. Some were found to have a significant impact under certain range and velocity conditions. Two multipath phase terms were also discovered, one of which is a result of the particular signal processing method employed.

Three mitigation methods were proposed and critically evaluated. Simulation results showed the potential viability of all three methods. Although the first two methods, Phase Unwrapping and Sum-Difference Processing, are computationally expensive, they have the potential to estimate the multipath error signal for a single channel. The third method, which uses a simple α -filter approach, is much easier to implement and also has a far lower computational overhead. All three methods were applied to real-world measurement data, with the α -filter method showing the best results by far.

All the objectives that were set at the beginning of this study have been completed:

- A novel multipath interference model was derived that accounts for both the environment and the range-Doppler processing method.
- Three mitigation methods were proposed and critically evaluated.

In addition to these objectives, a thorough mathematical derivation of the two-dimensional FFT signal processing method for FMCW systems was also completed, giving insight into the non-ideal aspects of this method.

Bibliography

- [1] Merrill I. Skolnik, *Introduction to Radar Systems*. New York, New York, USA: McGraw-Hill Book Company, Inc., 1962.
- [2] F. T. Ulaby, "Radar Measurement of Soil Moisture Content," *IEEE Transactions on Antennas and Propagation*, vol. AP-22, pp. 257-265, March 1974.
- [3] F. T. Ulaby, "Radar Response to Vegetation," *IEEE Transactions on Antennas and Propagation*, vol. AP-23, pp. 36-45, January 1975.
- [4] Maurice W. Long, *Radar Reflectivity of Land and Sea*, 2nd ed. Dedham, Ma, USA: Artech House, Inc., 1983.
- [5] Dr. Paul J. van der Merwe, Oral source.
- [6] A. K. Fung, J. Boisvert, and B. Brisco, "Interpretation of Radar Measurements from Rough Soil Surface with a Permittivity Profile," in *Proceedings of the 1997 IEEE International Geoscience and Remote Sensing Symposium*, vol. 3, Singapore, 1997, pp. 1376-1378.
- [7] W. H. Peake, "Theory of Radar Return from Terrain," in *IRE Convention Record*, vol. 7, 1959, pp. 27-41.
- [8] Cheng Donn and W. H. Peake, "The Generalized Lommel-Seeliger Cross Section of Foliage Environment," in *Meeting of International Union of Radio Science, Georgia Institute of Technology*, 1974.
- [9] J. W. Wright, "Backscattering from Capillary Waves with Application to Sea Clutter," *IEEE Transactions on Antennas and Propagation*, vol. AP-14, pp. 749-754, November 1966.
- [10] J. W. Wright, "A New Model for Sea Clutter," *IEEE Transactions on Antennas and Propagation*, vol. AP-16, pp. 217-223, March 1968.
- [11] M. L. Burrows, "On the Composite Model for Rough-Surface Scattering," *IEEE Transactions on Antennas and Propagation*, vol. AP-21, pp. 241-243, March 1973.
- [12] A. K. Fung and H. L. Chan, "Backscattering of Waves by Composite Rough Surfaces," *IEEE Transactions on Antennas and Propagation*, vol. AP-17, pp. 590-597, September 1969.
- [13] S. Horikoshi, M. Fujii, M. Itami, and K. Itoh, "A Study on Multipath Propagation Modeling in Millimeter Wave IVC," in *Proceedings of the 2002 5th International Symposium on Wireless*

Personal Multimedia Communications, 2002, pp. 286-290.

- [14] F. Kirsch, R. Miesen, and M. Vossiek, "Precise Local-Positioning for Autonomous Situation Awareness in the Internet of Things," in *Proceedings of the 2014 IEEE MTT-S International Microwave Symposium (IMS2014)*, Tampa, FL, 2014, pp. 1-4.
- [15] F. Ellinger et al., "Local Positioning for Wireless Sensor Networks," in *2007 IEEE Globecom Workshops*, Washington, DC, Nov. 2007, pp. 1-6.
- [16] R. Pfeil, S. Schuster, and A. Stelzer, "Optimized Parameter Estimation for the LPM Local Positioning System," *IEEE Transactions on Instrumentation and Measurement*, vol. 62, no. 1, pp. 153-166, Jan 2013.
- [17] L. Pengzheng, L. Zelong, H. Xiaotao, F. Chongyi, and Z. Jiahua, "A New Ranging Method with Monopulse STLFMCW Radar Signal in Multipath Environments," in *14th International Radar Symposium (IRS)*, Dresden, 2013, pp. 1056-1060.
- [18] S. Roehr, P. Gulden, and M. Vossiek, "Novel Secondary Radar for Precise Distance and Velocity Measurement in Multipath Environments," in *Proceedings of the 2007 European Radar Conference (EuRAD 2007)*, Munich, 2007, pp. 182-185.
- [19] S. Roehr, P. Gulden, and M. Vossiek, "Precise Distance and Velocity Measurement for Real Time Locating in Multipath Environments Using a Frequency-Modulated Continuous-Wave Secondary Radar Approach," *IEEE Transactions on Microwave Theory and Techniques*, vol. 56, no. 10, pp. 2329-2339, Oct 2008.
- [20] J. Wagner, A. Strobel, N. Joram, R. Eickhoff, and F. Ellinger, "FMCW System Aspects for Multipath Environments," in *8th Workshop on Positioning Navigation and Communication*, Dresden, 2011, pp. 89-93.
- [21] G. Li et al., "Bandwidth Dependence of CW Ranging to UHF RFID Tags in Severe Multipath Environments," in *IEEE International Conference on RFID*, Orlando, FL, 2011, pp. 19-25.
- [22] S. Roehr, P. Gulden, and M. Vossiek, "Method for High Precision Clock Synchronization in Wireless Systems with Application to Radio Navigation," in *Proceedings of the 2007 IEEE Radio and Wireless Symposium*, Long Beach, CA, 2007, pp. 551-554.
- [23] S. Roehr, M. Vossiek, and P. Gulden, "Method for High Precision Radar Distance Measurement and Synchronization of Wireless Units," in *Proceedings of the 2007 IEEE/MTT-S International Microwave Symposium*, Honolulu, HI, 2007, pp. 1315-1318.

- [24] C. Reustle, D. Shmakov, S. Röhr, and M. Vossiek, "Precise and Robust Crane Boom Tip Localization Using a 24 GHz Radar Tachymeter," in *Proceedings of the 2015 German Microwave Conference*, Nuremburg, 2015, pp. 190-193.
- [25] S. Gezici et al., "Localization via Ultra-Wideband Radios: a look at positioning aspects of future sensor networks," *IEEE Signal Processing Magazine*, vol. 22, no. 4, pp. 70-84, Jul 2005.
- [26] C. Zhang, M. Kuhn, B. Merkl, A. E. Fathy, and M. Mahfouz, "Accurate UWB Indoor Localization System Utilizing Time Difference of Arrival Approach," in *Proceedings of the 2006 IEEE Radio and Wireless Symposium*, San Diego, CA, 2006, pp. 515-518.
- [27] Robert J. Fontana and Steven J. Gunderson, "Ultra-Wideband Precision Asset Location System," *IEEE Conference on Ultra-Wideband Systems and Technologies*, May 2002.
- [28] C. Zhang, M. Kuhn, B. Merkl, M. Mahfouz, and A. E. Fathy, "Development of an UWB Indoor 3D Positioning Radar with Milimeter Accuracy," in *2006 IEEE MTT-S International Microwave Symposium Digest*, San Francisco, CA, 2006, pp. 106-109.
- [29] F. Ellinger et al., "European Project RESOLUTION - Local Positioning Systems Based on Novel FMCW Radar," in *Proceedings of the 2007 IEEE MTT-S International Microwave and Optoelectronics Conference (IMOC 2007)*, Brazil, 2007, pp. 499-502.
- [30] B. Waldmann, R. Weigel, and P. Gulden, "Method for High Precision Local Positioning Radar Using an Ultra Wideband Technique," in *2008 IEEE MTT-S International Microwave Symposium Digest*, Atlanta, GA, 2008, pp. 117-120.
- [31] B. Waldmann, R. Weigel, P. Gulden, and M. Vossiek, "Pulsed Frequency Modulation Techniques for High-Precision Ultra Wideband Ranging and Positioning," in *Proceedings of the 2008 IEEE International Conference on Ultra-Wideband*, Hannover, 2008, pp. 133-136.
- [32] B. Waldmann, R. Weigel, R. Ebel, and M. Vossiek, "An Ultra-Wideband Local Positioning System for Highly Complex Indoor Environments," in *Proceedings of the 2012 International Conference on Localization and GNSS*, Starnberg, 2012, pp. 1-5.
- [33] S. Max, C. Bohn, and M. Vossiek, "State Observation Using the Phase and the Beat Frequency of a FMCW Radar for Precise Local Positioning and Line-of-Sight Detection," in *Proceedings of the IEEE 68th Vehicular Technology Conference*, Calgary, BC, 2008, pp. 1-5.
- [34] S. Max, M. Vossiek, and P. Gulden, "Fusion of FMCW Secondary Radar Signal Beat Frequency and Phase Estimations for High Precision Distance Measurement," in *Proceedings of the 2008*

- European Radar Conference (EuRAD 2008)*, Amsterdam, 2008, pp. 124-127.
- [35] M. Vossiek, A. Urban, S. Max, and P. Gulden, "Inverse Synthetic Aperture Secondary Radar Concept for Precise Wireless Positioning," *IEEE Transactions on Microwave Theory and Techniques*, vol. 55, no. 11, pp. 2447-2453, Nov 2007.
- [36] S. Max, P. Gulden, and M. Vossiek, "Localization of Backscatter Transponders Based on a Synthetic Aperture Secondary Radar Imaging Approach," in *Proceedings of the 5th IEEE Sensor Array and Multichannel Signal Processing Workshop*, Darmstadt, 2008, pp. 437-440.
- [37] G. Li and M. Vossiek, "A Multilateral Synthetic Aperture Wireless Positioning Approach to Precise 3D Localization of a Robot Tool Center Point," in *Proceedings of the 2011 IEEE Topical Conference on Wireless Sensors and Sensor Networks (WiSNet)*, Phoenix, AZ, 2011, pp. 27-40.
- [38] J. L. Chu and J. F. Kiang, "Multipath Effects on Beacon Performances," in *Proceedings of the 2004 IEEE International Conference on Networking, Sensing and Control*, Taipei, 2004, pp. 635-638.
- [39] R. H. Lee, Z. D. Tsai, C. T. Lang, C. C. Chang, and S. F. Chang, "A Switched-Beam FMCW Radar for Wireless Indoor Positioning System," in *Proceedings of the 2011 European Radar Conference (EuRAD)*, Manchester, 2011, pp. 65-68.
- [40] R. H. Lee et al., "Radar Design for Wireless Indoor Positioning Applications," in *Proceedings of the 2013 European Microwave Conference (EuMC)*, Nuremberg, 2013, pp. 846-849.
- [41] R. Gierlich, J. Hüttner, A. Ziroff, R. Weigel, and M. Huemer, "A Reconfigurable MIMO System for High-Precision FMCW Local Positioning," *IEEE Transactions on Microwave Theory and Techniques*, vol. 59, no. 12, pp. 3228-3238, Dec 2011.
- [42] H. N. Wang, Y. W. Huang, and S. J. Chung, "Spatial-Diversity 24-GHz FMCW Radar With Ground Effect Compensation for Automotive Applications," *IEEE Transactions on Vehicular Technology*, 2016.
- [43] A. Goetz, B. Waldmann, and R. Weigel, "Short Multipath Mitigation Technique Using Feedforward Neural Networks," in *Proceedings of the 2009 German Microwave Conference*, Munich, 2009, pp. 1-4.
- [44] B. Waldmann, A. Goetz, and R. Weigel, "An Ultra Wideband Positioning System Enhanced by a Short Multipath Mitigation Technique," in *IEEE MTT-S International Microwave Workshop on Wireless Sensing, Local Positioning, and RFID*, Cavtat, 2009, pp. 1-4.

- [45] B. Al-Qudsi, E. Edwan, N. Joram, and F. Ellinger, "INS/FMCW Radar Integrated Local Positioning System," in *2014 DGON Inertial Sensors and Systems (ISS)*, Karlsruhe, 2014, pp. 1-10.
- [46] R. Sorrentino et al., "Accurate FMCW Radar-Based Indoor Localization System," in *Proceedings of the 2012 IEEE International Conference on RFID-Technologies and Applications*, Nice, 2012, pp. 362-368.
- [47] S. Wehrli et al., "Integrated Active Pulsed Reflector for an Indoor Local Positioning System," *IEEE Transactions on Microwave Theory and Techniques*, vol. 58, no. 2, pp. 267-276, Feb 2010.
- [48] R. Kumar, J. C. Cousin, and B. Huyart, "Performance of Indoor Localization System in Presence of Scatter for Strong Multipath Condition," in *Proceedings of the 2014 IEEE International Conference on Ultra-WideBand (ICUWB)*, Paris, 2014, pp. 25-29.
- [49] F. Ali and M. Vossiek, "Detection of Weak Moving Targets Based on 2-D Range-Doppler FMCW Radar Fourier Processing," in *German Microwave Conference Digest of Papers*, Berlin, 2010, pp. 214-217.
- [50] M. Song, J. Lim, and D. J. Shin, "The Velocity and Range Detection Using the 2D-FFT Scheme for Automotive Radars," in *Proceedings of the 2014 4th IEEE International Conference on Network Infrastructure and Digital Content*, Beijing, 2014, pp. 507-510.
- [51] L. Su, H. S. Wu, and C. K. C. Tzuang, "2-D FFT and Time-Frequency Analysis Techniques for Multi-Target Recognition of FMCW Radar Signal," in *Proceedings of the 2011 Asia-Pacific Microwave Conference*, Melbourne, VIC, 2011, pp. 1390-1393.
- [52] A. G. Stove, "Linear FMCW Radar Techniques," *IEE Proceedings F - Radar and Signal Processing*, vol. 139, no. 5, pp. 343-350, Oct 1992.
- [53] A. Wojtkiewicz, J. Misiurewicz, M. Nałęcz, K. Jędrzejewski, and K. Kulpa, "Two-Dimensional Signal Processing in FMCW Radars," in *Proceedings of the 20th National Conference on Circuit Theory and Electronics Networks*, Kołobrzeg, Poland, 1997, pp. 475-480.
- [54] Paul J. van der Merwe, "CXDM baseline characterization with POC antenna report," Stellenbosch, 2011.
- [55] T. Benedict and G. Bordner, "Synthesis of an optimal set of radar track-while-scan smoothing equations," *IRE Transactions on Automatic Control*, vol. 7, no. 4, pp. 27-32, July 1962.
- [56] C. C. Schooler, "Optimal α - β Filters for Systems with Modeling Inaccuracies," *IEEE*

- Transactions on Aerospace and Electronic Systems*, vol. 11, no. 6, pp. 1300-1306, November 1975.
- [57] Paul R. Kalata, "The Tracking Index: A Generalized Parameter for α - β and α - β - γ Target Trackers," *IEEE Transactions on Aerospace and Electronic Systems*, vol. 20, no. 2, pp. 174-182, March 1984.
- [58] Paul J. van der Merwe, "Report on the TATS-150 Simulation Results," Reutech Radar Systems (Pty) Ltd., 2008.
- [59] M. Vossiek, L. Wiebking, P. Gulden, J. Wieghardt, and C. Hoffmann, "Wireless Local Positioning - Concepts, Solutions, Applications," in *Proceedings of the 2003 Radio and Wireless Conference (RAWCON '03)*, 2003, pp. 219-224.
- [60] E. Hyun, Y. S. Jin, Y. Ju, and J. H. Lee, "Development of Short-Range Ground Surveillance Radar for Moving Target Detection," in *Proceedings of the 2015 IEEE 5th Asia-Pacific Conference on Synthetic Aperture Radar (APSAR)*, Singapore, 2015, pp. 692-695.
- [61] John G. Proakis and Dimitris G. Manolakis, *Digital Signal Processing: Principles, Algorithms, and Applications*. Prentice-Hall, Inc., 1996.